

Faculty of Engineering of the University of Porto



**Tumor-Targeting Functional Nanoparticles for Cancer
Therapy**

Inês David Amorim do Rego Torres
Up201908312

Porto, June 2022

Faculty of Engineering of the University of Porto



Tumor-Targeting Functional Nanoparticles for Cancer Therapy

Inês David Amorim do Rego Torres
Up201908312

Master Dissertation
Master's in Biomedical Engineering

Supervisor: Prof. Dr. Maria do Carmo Pereira
Co-Supervisor: Dr. Maria João Ramalho

Porto, June 2022

Financial Support

This work was financially supported by LA/P/0045/2020 (ALiCE), UIDB/00511/2020 and UIDP/00511/2020 (LEPABE), funded by national funds through FCT/MCTES (PIDDAC); Project 2SMART - engineered Smart materials for Smart citizens, with reference NORTE-01-0145-FEDER-000054, supported by Norte Portugal Regional Operational Program (NORTE 2020), under the PORTUGAL 2020 Partnership Agreement, through the European Regional Development Fund (ERDF); and Prize “Maratona da Saúde” for Cancer Research.

“We do not need magic to change the world, we carry all the power we need inside ourselves already: we have the power to imagine better.”

JK Rowling

Acknowledgments

The end of a great journey is approaching and I could not fail to thank those who unconditionally gave me their support and patience, making this journey one of the most important in my academic life.

First of all, I want to deeply thank my supervisors Prof. Dr. Maria do Carmo Pereira and Dr. Maria João Ramalho, for all the scientific guidance, assistance and knowledge passing. I am heartily grateful to them. To my lab colleagues at LEPABE and DEQ, thank you for all. I would like to thank Dr. Paula Soares and Dr. Jorge Lima from the Cancer Signaling & Metabolism Group at the Institute for Research and Innovation in Health Sciences (i3S) for making available the facilities to perform the cellular studies.

To all my friends and family, who have been supporting me throughout this year.

To Tiago, thank you for all the love, patience, for all the encouraging words and for always believing in me.

To my mother and father, thank you for all the wise advices and for all the unconditional support, love and trust.

I am so grateful to have you all in my life! Thank you.

Resumo

O glioblastoma multiforme (GBM) é um tumor cerebral altamente invasivo, classificado como um dos tumores cerebrais mais letais do sistema nervoso central. A terapia convencional do GBM consiste em neurocirurgia, seguida de ciclos de radioterapia combinados com quimioterapia com o fármaco temozolomida (TMZ). Contudo, esta terapia multimodal não é eficaz, aumentando apenas modestamente o tempo de sobrevivência do paciente. A ineficácia do TMZ deve-se, em grande parte, aos mecanismos de reparação do DNA mediados pela proteína O⁶-metilguanina DNA metiltransferase (MGMT). Adicionalmente, a existência de barreiras biológicas, como a barreira hematoencefálica (BHE), diminuem a biodisponibilidade dos fármacos no tecido tumoral. Assim, têm sido estudadas estratégias inovadoras para ultrapassar estes obstáculos.

O objetivo deste trabalho foi desenvolver nanopartículas (NPs) de poli (ácido lático-co-ácido glicólico) (PLGA) como veículos de administração de fármacos para a terapia do GBM. Neste trabalho, as NPs de PLGA foram propostas para a co-encapsulação dos fármacos TMZ e bortezomib (BTZ). Em ensaios clínicos, a co-terapia com o BTZ mostrou aumentar a eficácia terapêutica do TMZ, ao inibir a proteína MGMT. No entanto, a elevada toxicidade verificada nos ensaios clínicos cria a necessidade do uso de veículos de administração para dirigir os fármacos ao tecido-alvo, maximizando assim o efeito terapêutico e minimizando os efeitos secundários.

As NPs foram produzidas pelo método de emulsão simples com evaporação do solvente e a sua preparação foi otimizada através da implementação de um desenho experimental. Para que as NPs sejam específicas para as células tumorais, foram ainda funcionalizadas com moléculas de transferrina (Tf). As NPs preparadas apresentaram propriedades físico-químicas adequadas. Ambos os fármacos exibiram elevadas eficiências de encapsulação (EE), bem como, uma libertação controlada ao longo de 15 dias. Para avaliar o efeito antiproliferativo das NPs produzidas, foram realizados ensaios *in vitro* utilizando duas linhas de células humanas T98G e U251. Estes ensaios celulares das NPs desenvolvidas, provaram aumentar a eficiência da TMZ, resultando em valores de IC₅₀ muito mais baixos para as NPs TMZ+BTZ e Tf-TMZ+BTZ PLGA NPs.

Palavras-chave: Glioblastoma Multiforme; Co-administração Controlada de Fármacos; Bortezomib; Temozolomida; Poli (ácido lático-co-ácido glicólico); Transferrina.

Abstract

Glioblastoma multiforme (GBM) is a highly invasive brain tumor, ranked as one of the most lethal tumors of the central nervous system. Conventional GBM therapy consists primarily of neurosurgery to remove as much tumor tissue as possible, followed by radiotherapy cycles combined chemotherapy with temozolomide (TMZ). However, this multimodal therapy is ineffective, only modestly increasing the patient's survival. The ineffectiveness of TMZ is largely due to DNA repair mechanisms mediated by the O⁶-methylguanine DNA methyltransferase (MGMT) protein. Additionally, the existence of biological barriers, such as the blood-brain barrier (BBB), decreases the bioavailability of drugs in the tumor tissue. Thus, innovative strategies have been studied to overcome these obstacles that prevent an effective and local administration of drugs.

This study aimed to develop poly (lactic-co-glycolic acid) (PLGA) nanoparticles (NPs) as drug delivery systems for GBM therapy. In this work, PLGA NPs were proposed for the co-encapsulation of the drugs TMZ and bortezomib (BTZ). In clinical trials, co-therapy with BTZ was proved to enhance the therapeutic efficiency of TMZ by inhibiting DNA repair mechanisms mediated by the MGMT protein. However, the high toxicity observed in clinical trials leads to the need of using nanocarriers to actively deliver the therapeutic drugs into the target tissue, maximizing the therapeutic effect and minimizing the side effects.

The TMZ+BTZ loaded PLGA NPs were produced by the single emulsion-solvent evaporation method and optimized by experimental design to obtain NPs with the most suitable physicochemical properties for brain delivery. To enhance the NPs specificity, these were conjugated with transferrin (Tf). The prepared NPs showed adequate physicochemical properties. Both drugs exhibited high encapsulation efficiencies (EE), as well as a controlled release through the PLGA matrix over 15 days. To assess the antiproliferative effect of Tf-TMZ+BTZ PLGA NPs, *in vitro* cell assays were performed using two human cell lines T98G and U251. The antiproliferative effect of the developed NPs proved to increase the efficiency of TMZ, resulting in a much lower IC₅₀ values for free TMZ+BTZ and Tf-TMZ+BTZ PLGA NPs.

Keywords: Glioblastoma Multiforme; Co-delivery System; Bortezomib; Temozolomide; Poly (lactic acid-co-glycolic acid); Transferrin.

Contents

1	Introduction	1
1.1	Main Objectives	2
1.2	Dissertation Output	2
2	State of Art	5
2.1	Glioblastoma Multiforme	5
2.2	Conventional Diagnosis and Treatment of GBM	6
2.3	TMZ as a Therapeutic Agent	7
2.3.1	Limitations of TMZ	8
2.3.2	Biological Brain Barriers	9
2.3.3	DNA Repair Systems and Resistance to TMZ Therapy	10
2.4	Strategies to Overcome MGMT Resistance	11
2.4.1	MGMT Inhibitors of Gene and Protein Expression	12
2.5	MGMT Protein and BTZ Pharmacological Activity	13
2.6	Nanomedicine	14
2.6.1	Drug Delivery Systems for GBM Treatment	15
2.6.2	Drug Delivery Systems to Overcome MGMT Resistance in GBM Treatment	18
3	Materials and Methods	28
3.1	Materials	28
3.2	Preparation of of TMZ+BTZ Loaded PLGA NPs	29
3.3	Experimental Design and Protocol Optimization	29
3.4	Preparation of the Transferrin Functionalized NPs	32
3.5	NPs Physicochemical Characterization	33
3.5.1	Dynamic Light Scaterring	33
3.5.2	Laser Doopler Velocimetry	34
3.6	Determination of the Encapsulation Efficiency and Loading Capacity	35
3.7	Determination of Tf Conjugation Efficiency	36
3.8	Fourier-Transformed Infrared Spectroscopy	36

3.9 Transmission Electron Microscopy	37
3.10 <i>In vitro</i> Release of TMZ and BTZ from PLGA NPs	37
3.11 Determination of NPs Stability	38
3.12 Cell Culture.	38
3.13 <i>In vitro</i> Cytotoxicity Studies	39
3.14 Statistical Analysis	39
4 Results and Discussion	41
4.1 Experimental Design and Protocol Optimization	41
4.1.1 Effect on the NP's Size	44
4.1.2 Effect on the NPs' PDI	45
4.2 Protocol Optimization and Model Validation	46
4.3 Transferrin-TMZ+BTZ Loaded PLGA NPs	48
4.4 PLGA NPs and Transferrin Conjugation	49
4.5 TMZ+BTZ Release Profile	51
4.6 Stability of PLGA NPs in Storage Conditions	53
4.7 Stability of PLGA NPs in Physiological Conditions	54
4.8 NPs' Antiproliferative Activity	55
5 Conclusion and Future Perspectives	60
References	63
Appendix	

List of Figures

Figure 1 – Representation of all the chemical structures involved in TMZ activation and conversion	8
Figure 2 – Schematic representation of the BBB and its constituents	9
Figure 3 – (1) DNA methylation by alkylating agents, specifically TMZ; (2) MGMT repair mechanism; (3) Restored guanine with MeS (methyl group+S) and inactivated MGMT as reaction products	11
Figure 4 – Inhibition of the DNA repair mechanism mediated by MGMT protein inactivation . . .	12
Figure 5 – Proteasome inhibitor BTZ mechanism through blocking the NF- κ B activity	13
Figure 6 – Illustration of the different types of NPs used in nanomedicine: A – liposome; B – micelle; C – dendrimer; D – polymeric NP (nanocapsule; nanosphere); E – Metallic NP.	15
Figure 7 – Contrast with a normal lymphatic system and a dysfunctional lymphatic system resulting in EPR effect	16
Figure 8 – Illustration of the mechanisms of passive and active targeting in nanostructures loaded with drugs; a) the NPs pass diffusely through the BBB by the leaky vasculature and accumulate in tumor tissue; b) 1- targeted NPs binds to the cellular receptors; 2 – NP enters in the intracellular space inside an endosome; 3- endosomal escape and local drug release	17
Figure 9 – (A) Carbodiimide Coupling reaction for Tf conjugation; (B) TMZ+BTZ PLGA NPs conjugated with Tf. The blue dots represent the TMZ and the orange dots represent the BTZ.	32
Figure 10 – Illustration of the different layers involved in zeta potential measurement	34
Figure 11 – Graphical plots between the experimental values obtained vs the predicted values for the significant variables (A) Size (Y_1) and (B) PDI (Y_2). The blue squares represent the lower values, in contrast to red squares that represent higher values	42
Figure 12 – (A) Contour and (B) response surface plots showing the effect of independent variables, PLGA mass and %PVA, on the NPs' size	44

Figure 13 – (A) Contour and (B) response surface plots showing the effect of independent variables, sonication cycles and O/W ratio, on the NPs' size	44
Figure 14 – (A) Contour and (B) response surface plots showing the effect of independent variables, PLGA mass and O/W ratio, on the NPs' PDI	45
Figure 15 – (A) Contour and (B) response surface plots showing the effect of independent variables, the %PVA and sonication cycles, on the NPs' PDI	46
Figure 16 – TEM image of the prepared Tf- BTZ+TMZ PLGA NPs. Scale bar 500 nm.	49
Figure 17 – FTIR absorbance spectrum of (A) PLGA NPs (control) and (B) Tf stock solution for conjugation recorded from 350-4000 cm^{-1}	50
Figure 18 – FTIR absorbance spectrum of Tf-TMZ+BTZ PLGA NPs, TMZ+BTZ PLGA NPs and Tf stock solution recorded from 350-4000 cm^{-1}	51
Figure 19 – <i>In vitro</i> release profile of (A) TMZ and (B) BTZ from Tf-conjugated and non-conjugated PLGA NPs in PBS (pH 7.4, 0.01M) at 37 °C. The results are represented as mean \pm SD (n=2)	52
Figure 20 – Cell survival inhibition curve after 72 h treatment with free TMZ, free on two GBM human cells by SRB assay. (A) U251 cells and (B) T98G cells. Cell survival is presented as percent [(%) = ((T)/(C) x 100)]. Data represented as mean \pm SD (n=3)	56
Figure 21 – Cell survival inhibition curve after 72h co-treatment with TMZ and BTZ, free or entrapped in Tf-modified PLGA NPs, on two GBM human cells by SRB assay. (A) U251 cells and (B) T98G cells. Cell survival is presented as percent [(%) = ((T)/(C) x 100)]. Data represented as mean \pm SD (n=3)	57
Figure 22 – Cell survival inhibition curve after 72 h treatment with free BTZ, free on two GBM human cells by SRB assay. (A) U251 cells and (B) T98G cells. Cell survival is presented as percent [(%) = ((T)/(C) x 100)]. Data represented as mean \pm SD (n=3)	57

Appendix

Figure A1.1 – Fluorescence (RFU) calibration curve of TMZ in PVA 2% to determine the EE of TMZ	a
Figure A1.2 – Absorbance calibration curve of BTZ in PVA 2% to determine the EE of BTZ	a
Figure A1.3 – Absorbance calibration curve of Tf using the BCA kit for Tf quantification	a
Figure A2.1 – Interaction plots regarding to Y_1 the NPs' size. (A) Interaction plot of X_1 and X_2 . The red line represents the O/W ratio (X_4) values (+1), and the black line represents the sonication cycles (X_3) values (-1). (B) Interaction plot of X_1 and X_3 . The red line represents the O/W ratio (X_4) values (+1), and the black line represents the %PVA (X_2) values (-1). (C) Interaction plot of X_1 and X_4 . The red line represents the sonication cycle (X_3) values (-1), and the black line represents the %PVA (X_2) values (-1). (D) Interaction plot of X_2 and X_4 . The red line represents the sonication cycle (X_3) values	

(+1), and the black line represents the PLGA mass (X_1) values (-1). (E) Interaction plot of X_3 and X_4 . The red line represents the %PVA (X_2) values (-1), and the black line represents the PLGA mass (X_1) values (+1) f

Figure A3.1 – FTIR absorbance spectrum of TMZ+BTZ loaded PLGA NPs solution recorded from 350-4000 cm^{-1} g

Figure A3.2 – FTIR absorbance spectrum of Tf-unloaded PLGA NPs solution recorded from 350-4000 cm^{-1} g

List of Tables

Table 1 – Nanosystems for the delivery of MGMT inhibitors to overcome the MGMT DNA repair mechanisms in GBM therapy	19
Table 2 – Nanosystems for gene therapy to suppress the MGMT activity in GBM therapy	23
Table 3 – Process and formulation of the parameters of the Experimental Design used	30
Table 4 – Experimental plan overview and results. The experimental levels (low, center and high) are represented by the coded values of -1, 0, +1, respectively from 1 to 19 and $-\alpha$, 0, $+\alpha$ from 20 to 27	31
Table 5 – Results of the statistical analysis using ANOVA of the significant variables Y_1 and Y_2	42
Table 6 – Regression coefficients (RC) and p-values for the significant variables Y_1 and Y_2	43
Table 7 – Optimal formulation values of TMZ+BTZ loaded PLGA NPs determined by experimental design	47
Table 8 – Validation model; Comparison between the predicted and the experimental values obtained. The experimental results are represented as mean \pm SD (n=3)	47
Table 9 – Experimental data obtained for the Tf-TMZ+BTZ loaded PLGA NPs. The data is represented as mean \pm SD (n=3)	48
Table 10 – Mean size, PDI and zeta potential values for both Tf conjugated (n=2) and non-conjugated (n=3) TMZ+BTZ loaded PLGA NPs in storage conditions. Data is represented as mean \pm SD ...	53
Table 11 – Mean size, PDI and zeta potential values for both Tf conjugated (n=2) and non-conjugated (n=3) TMZ+BTZ loaded PLGA NPs in physiological conditions. Data is represented as mean \pm SD	54

Table 12 – Cytotoxic effects of the different treatments on the survival of U251 and T98G cell. Results are expressed as IC ₅₀ values of 72h of exposure with free TMZ, free BTZ, free TMZ+BTZ or Tf-TMZ+BTZ PLGA NPs	56
--	----

Appendix

Table A2.1 – ANOVA analysis for the response variable Size (Y ₁) applying a quartic model	b
Table A2.2 – ANOVA analysis for the response variable PDI (Y ₂) applying a linear model	b
Table A2.3 – ANOVA analysis for the response variable Zeta Potential (Y ₃) applying a quadratic model	c
Table A2.4 – ANOVA analysis for the response EE TMZ (Y ₄) applying a quadratic model	d
Table A2.5 – ANOVA analysis for the response EE BTZ (Y ₅) applying a quadratic model	d

Abbreviations, Acronyms & Symbols

AIC	5-aminoimidazole-4-carboxamide
BBB	Blood-Brain Barrier
BBTB	Brain-Blood Tumor Barrier
BER	Base Excision Repair
BTZ	Bortezomib
CCD	Central Composite Design
CE	Conjugation Efficiency
CED	Convection-enhanced delivery
CNS	Central Nervous System
CT	Computed Tomography
DCM	Dichloromethane
DDSs	Drug Delivery Systems
DLS	Dynamic Light Scattering
DMEM	Dulbecco's Modified Eaglec Medium
DMSO	Dimethyl Sulfoxide
DoE	Design of Experiment
DOX	Doxorubicin
EA	Ethyl Acetate
EE	Encapsulation Efficiency
EGFR	Epidermal Growth Factor Receptor
EPR	Enhanced Permeability and retention
ER	Endoplasmic Reticulum
FBS	Fetal Bovine Serum
FDA	Food and Drug Administration
FFD	Full Factorial Design
FTIR	Fourier-Transformed Infrared Spectroscopy
GBM	Glioblastoma Multiforme

GSCs	Glioma Stem Cells
IC ₅₀	Half maximal inhibitory concentration
IDH	Isocitrate Dehydrogenase
IR	Infrared
MC	Methyldiazonium cation
MGMT	O ⁶ -Methylguanine-DNA Methyltransferase
MMP	Matrix Metalloproteinases
MMR	Mismatch Repair
MTIC	5-(3-methyltriazen-1-yl) imidazole-4-carboxamide
NF	Nuclear Factor
NPs	Nanoparticles
PBCA	Polybutylcyanoacrylate
PBS	Phosphate-buffered saline
PDGFRA1	Platelet-Derived Growth Factor Receptor A
PET	Positron Emission Tomography
PIHCA	Poly (isohehexyl cyanoacrylate)
PLGA	Poly (lactic-co-glycolic acid)
PVA	Polyvinyl Alcohol
SRB	Sulforhadamine B
TCA	Trichloroacetic Acid
TEM	Transmission Electron Microscopy
Tf	Transferrin
TfR	Transferrin Receptors
TMZ	Temozolomide
TTF	Tumor-Treating Fields
WHO	World Health Organization
WR	Working Reagent
ZP	Zeta Potential

Lists of symbols

α	Alpha
β	Beta
μ_e	Electrophoretic mobility
ϵ	Dielectric constant

η	Viscosity
ζ	Zeta Potential
v	Velocity
E	Electric field
K	Boltzmann constant
T	Absolute temperature
D_t	Translation diffusion coefficient
R_h	Hydrodynamic radius

Chapter 1

Introduction

Glioblastoma multiforme (GBM) is the most common, invasive and aggressive form of malignant gliomas, representing approximately 50% of all primary brain tumors [1]. Overall, GBM is characterized by a poor prognosis due to therapy resistance and frequent recurrence after treatment. The standard treatment procedure is primarily a neurosurgical resection to eliminate as many tumor tissue followed by radio and adjuvant chemotherapy with temozolomide (TMZ). TMZ is a powerful alkylating agent designed to deliver a methyl group to purine bases of DNA, leading to its degradation and, consequently, resulting in cell death [2, 3].

GBM tumors are represented by unique characteristics such as high proliferation and angiogenic effects, high intratumor molecular and cellular heterogeneity, genetic instability, high diffuse infiltration power resulting in recurrence and elevated tumor resistance to current therapies. In addition, biological barriers such as the blood-brain barrier (BBB) and blood tumor brain barrier (BBTB), lead to low drugs' bioavailability and poor pharmacokinetics, increasing the ineffectiveness and limitation of the delivery of chemotherapeutic agents [4]. Moreover, the multidrug resistance mechanism (MDR) also represents a crucial limitation factor in GBM therapy due to the TMZ transport out of cells mediated by cell membrane efflux pump p-glycoprotein [5].

Furthermore, resistance to therapy is also mediated by the O⁶-methylguanine-DNA methyltransferase (MGMT) protein [6]. MGMT is a protein responsible for repairing the alkylating agent induced DNA lesions [7]. Thus, the use of molecules capable of inactivating the MGMT repair mechanism have been proposed as a new therapeutic approach to enhance the sensitivity of the current chemotherapeutic agents [8, 9].

Bortezomib (BTZ) is a proteasome inhibitor that inhibits the transcription factor involved in the regulation of MGMT gene expression, therefore enhancing the TMZ sensitivity in cancer cells

by decreasing the expression of the MGMT protein [9]. Thus, the concomitant therapy with BTZ and TMZ has been proposed to improve the outcomes in GBM treatment [10].

However, the accumulation of BTZ in healthy tissues is undesirable to avoid the inactivation of MGMT protein in these tissues and consequent exacerbated toxicity of the alkylating agents. Therefore, nanotechnology for drug delivery appears as a suitable solution.

Drug delivery using nanoparticles (NPs) also allows to overcome other limitations due to the enhanced permeability and retention (EPR) effect and circumvention of MDR [11]. Drug encapsulation in nano-sized nanocarriers can be a favorable strategy for GBM treatment capable of enhancing the transport across the biological barriers, increasing drug bioavailability in the target tissues, therefore decreasing side effects in surrounding healthy tissues.

The FDA approved poly (lactic-co-glycolic acid) PLGA nanoparticles (NPs) are one of the most popular nanocarriers due to their high biocompatibility, biodegradability, stability and ease of handling and functionalization, being able to custom made a specific and target therapy [12]. Therefore, these were proposed for co-delivery of TMZ and BTZ in this work.

1.1 Main Objectives

The main objective of this work was to develop PLGA NPs as an effective drug delivery system (DDS) for the co-delivery of TMZ and BTZ. For that, the PLGA NPs were functionalized with Tf to enhance the NPs' specificity as a dual-targeting approach of BBB and GBM tumor cells. The goal of this formulation is to overcome the limitations of both TMZ and BTZ when administrated alone through a controlled delivery, without systemic toxicity. This will also allow overcoming the major drawbacks associated with resistance to GBM therapy such as DNA repair mechanisms and BBB/BBTB permeability.

1.2 Dissertation Output

The research work was carried out at LEPABE – Laboratory for Process Engineering Environment, Biotechnology and Energy at the Faculty of Engineering of the University of Porto. The *in vitro* studies were performed at i3S – Institute for Research and Innovation in Health. This work resulted in the following outputs:

- Participation in conferences:

Torres, I. D., Loureiro, J. A., Ramalho, M. J. and Pereira, M. C. Tumor-Targeting Functional Nanoparticles for Cancer Therapy in 15th Encontro de Investigação Jovem (IJUP), 4-6 May 2022, Porto, Portugal (oral presentation)

Torres, I. D., Loureiro, J. A., Ramalho, M. J. and Pereira, M. C. Resistance-targeting nanoparticles for glioblastoma therapy in 11th International Colloids Conference, 12-15 June 2022, Lisboa, Portugal (poster presentation)

- Papers submitted to international peer-review journals:

Torres, I. D., Loureiro, J. A., Coelho, M.A.N., Pereira, M. and Ramalho, M. J. Drug delivery in glioblastoma therapy: a review on nanoparticles targeting MGMT-mediated resistance. Under review in Expert Opinion on Drug Delivery.

Chapter 2

State of Art

In this chapter, was performed a literature review on the malignant brain tumor, glioblastoma multiforme, its current treatment limitations, and their challenges. Followed by outstanding nano-approaches to overcome these limitations to improve the overall therapeutic efficiency.

2.1 Glioblastoma Multiforme

Glioblastoma multiforme is the most prevalent type of malignant brain tumor, with an incidence rate of about 3.19 per 100.000 people per year [1, 13, 14]. Despite all the efforts, GBM remains a very challenging disease because of its resistance to treatment and unique characteristics [15, 16]. GBM is a type of glioma, which affects the neoplastic glial cells, such as astrocytes, that are responsible for the normal and healthy function of the brain [15]. The finger-shaped tentacles of glial cells, make GBM a highly invasive tumor that rapidly infiltrates into deeper regions of the brain [17]. The term *multiforme* refers to the ability of this tumor to display different shapes, sizes and locations, yet this disease is distinguished by small brain areas of necrotic tissue surrounded by anaplastic cells.

This type of tumor can be subdivided into primary (or de novo) and secondary tumors. Primary GBM corresponds to 90% of the cases and arise spontaneously from normal glial cells, and these mostly develop in elderly patients without any clinical history of brain lesions [13]. Secondary GBM emerges from pre-existing low-grade anaplastic astrocytomas, grade III gliomas, and are more common in younger patients [13, 18, 19]. Both types have the same main features of genetic mutations, affecting pathways concerning cellular proliferation, survival, invasion and angiogenesis. However, they display some distinguished characteristics, such as genetic profiles with distinctly transcriptional patterns and the number of DNA aberrations. For this reason, the need for tailored made therapy at a molecular level is the goal to improve survival rates [4, 20].

The etiology of GBM remains unknown, however, some reports address the topic of a possible genetic predisposition to develop GBMs. In fact, GBM features a complex genetic expression, resulting in the overexpression of several molecular markers, being the epidermal growth factor receptor (EGFR), isocitrate dehydrogenase (IDH-1/2) and O⁶-methylguanine-DNA methyltransferase (MGMT) the most evident molecular characteristics in GBM [17, 21]. In addition, histopathological studies of GBM characteristics show that tumor invasion, development, and permanency mechanisms are such complex as its genetic expression. As a grade IV brain tumor, the GBM is characterized by a range of heterogeneous cells, very resistant and genetically unstable [17]. Some key features of GBM include increase vascular and endothelial cells proliferation, necrosis and increased angiogenic events. GBM is the most angiogenic brain tumor, increasing its ability to therapy resistance [17, 22].

Moreover, the most common symptoms associated with GBM are headaches, gait imbalance, incontinence, sensory loss, visual disturbances, seizures, confusion, delirium, cognitive impairments, and personality disorders [17, 23]. These types of tumors have a very high cellular activity, leading to rapid tumor growth and worsening of symptoms [18]. Despite all the technological and scientific development, after diagnosis, the median survival of GBM patients is between 12.5 to 18 months and only 4-7% a five-year survival rate [22, 24]. This reduced survival rate is due to treatment limitations, the diffuse nature of GBM, and an uncertain understanding of tumor pathophysiology [21].

2.2 Conventional Diagnosis and Treatment of GBM

The initial diagnosis approach for GBM is to perform a magnetic resonance imaging (MRI) scan. To improve the overall diagnosis, simultaneous imaging techniques should be employed, such as computed tomography (CT) and positron emission tomography (PET) [3, 25, 26].

The standard treatment for newly diagnosed GBM patients consists primarily of neurosurgical resection to eliminate as many as tumor tissues as possible and to extract tissue histopathological information. The procedure is followed by radiotherapy cycles combined with co-adjuvant chemoradiotherapy with TMZ. This procedure is known as the Stupp protocol and is the gold-standard care for GBM treatment [26]. However, its clinical success is limited resulting in approximately 80% of the tumors already resected, showing a tendency to recur at the primary sites [27]. This occurs because the complete removal of the GBM tumors is practically unattainable, due to their location and/or depth, and leading to irreparable surrounding brain tissue damage.

As any other treatment, radio and chemotherapy have several limitations. Firstly, radiotherapy depends on the tumor's size, larger tumors respond poorly to radiation treatments because of radiobiological features [28]. In addition, glioma stem cells (GSCs) also contribute significantly to tumor resistance and recurrence [29]. These cells are specific small subpopulations of GBM tumor cells with unlimited self-renew capacities and inductive stress. The exposure of GSCs to the current therapeutic solutions, as radiation, emphasize later differentiation into high proliferative malignant cells consequently more resistant cells [30, 31]. Both radio and chemotherapy also give origin to acute side effects, as epithelial surfaces damage, mouth and throat ulcers and infertility. Hair loss, heart diseases, fibrosis and lymphedema, are some of the long term side effects [32].

Over the past years, FDA has been approving different approaches for GBM treatment. The antibody Bevacizumab is used for anti-angiogenic therapy combined with an inhibitor of vascular endothelial growth factor (VEGF), however, this approach is inefficient since the antibody cannot penetrate the BBB [33, 34]. In addition, delivery of monoclonal antibodies, immune modulators, adoptive T-cell transfer and immune checkpoint blockade have also been studied [35]. However, clinical results display limited efficacy in GBM treatment and low immunogenic response [36]. Plus, therapies combined with a controllable external physical stimulus e.g., magnetic fields, light waves and ultrasound, such as photodynamic therapy, magnetic hyperthermia, electrotherapy and sonodynamic therapy have been explored. These types of therapies are known as tumor-treating fields (TTF) therapy and exhibit very advantages due to their minimal invasive manipulation [36, 37]. Additionally, bevacizumab can be used together with drugs such as TMZ, irinotecan, carmustine/lomustine and carboplatin. Other drugs conjugation includes procarbazine, lomustine and vincristine cyclophosphamide and platinum-based regimens [38].

2.3 TMZ as a Therapeutic Agent

TMZ, a small lipophilic molecule, is a monofunctional DNA alkylating agent dacarbazine derivative from the imidazotetrazines class. The chemical name of TMZ is 3-methyl-4-oxoimidazo tetrazine-8-carboxamide [39]. TMZ can be administrated orally or intravenously, and acts as a stable prodrug at acidic pH <5 [40]. At physiological pH the prodrug rapidly undergoes spontaneous hydrolysis, being completely converted to its active metabolite 5-(3-methyltriazene-1-yl)imidazole-4-carboxamide (MTIC) [41]. MTIC is then converted to 5-aminoimidazole-4-carboxamide (AIC) and a highly reactive methyldiazonium cation (MC), the active species responsible to methylate DNA specific positions [42]. The chemical structures of these metabolites and the conversion sequence are represented schematically in figure 1.

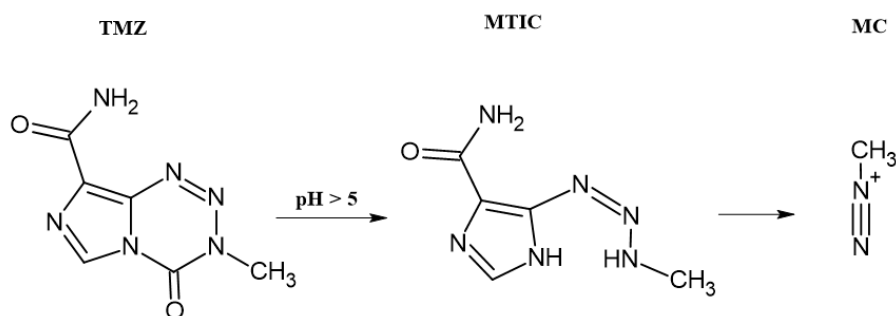


Figure 1- Representation of all the chemical structures involved in TMZ activation and conversion.

The combination of radio and TMZ adjuvant chemotherapy leads to an increase of the survival rate in 2.5 months, compared with patients only receiving radiotherapy [43]. This improvement of the patient survival rate enabled the establishment of TMZ as a standard antitumoral pharmaceutical for GBM treatment in 2005 by the Food and Drug Administration (FDA) [44]. Alkylating agents, such as TMZ, add alkyl groups to the guanine base of the DNA molecule leading to the formation of different small or bulky adducts, leading to irreparable damage affecting its ability to cell replication and, subsequently, leading to apoptosis [45].

2.3.1 Limitations of TMZ

As other chemotherapeutic agents, TMZ exhibits high toxicity to the healthy tissues [46], leading to some adverse reactions such as thrombocytopenia, lymphopenia, neutropenia and myelodysplastic syndrome, a disturbance of the bone marrow that may result in leukemia [46, 47]. Plus, it was reported that 7% of the GBM patients had to stop the treatment due to toxic side-effects [32, 33].

The efficiency of TMZ is also limited by its bioavailability that is significantly reduced as the interactions with blood and plasma components occur [48]. Additionally, resistance mechanisms lead to low therapeutic outcomes [6]. High-grade gliomas are often characterized by chemotherapy resistance. This resistance can either be primary/intrinsic resistance or secondary/acquired resistance. Intrinsic resistance is when failure to respond to upfront therapy. Alternatively, acquired resistance failure in the follow-up of an initial response to the same therapy [48].

Furthermore, the efficacy of TMZ is dependent on interactions with the biological barriers, such as the BBB and BBTB. The lipophilic characteristics of TMZ molecules enable them to pass through these biological barriers. However, the TMZ active metabolite, MTIC, does not have an affinity to the biological barriers [49].

2.3.2 Biological Brain Barriers

The BBB is a highly selective and active interface composed of endothelial cells, spinal cord capillaries and perivascular cells, such as astrocytes, pericytes, microglial cells and smooth muscle cells [50]. The biochemical components of the BBB are fundamental for regulating the movements of molecules between the systemic circulation and the brain interstitial fluid, preserving CNS homeostasis, as well as, protecting the brain from undesired exposure to exogenous molecules [51].

The support structures of the BBB are linked together by tight junctions forming a continuous and nearly impermeable barrier to the extracellular fluid. This constitutes an obstacle to the most therapeutic compounds to reach the brain [52, 53]. It has been reported that the BBB is impermeable to 100% of the larger molecules and to approximately 98% of the smaller molecules (<500 Da). With the lack of paracellular or transcellular channels, the molecules only can pass through the BBB by mechanisms as simple/facilitated diffusion, carrier or receptor-mediated and adsorptive-mediated transcytosis [54].

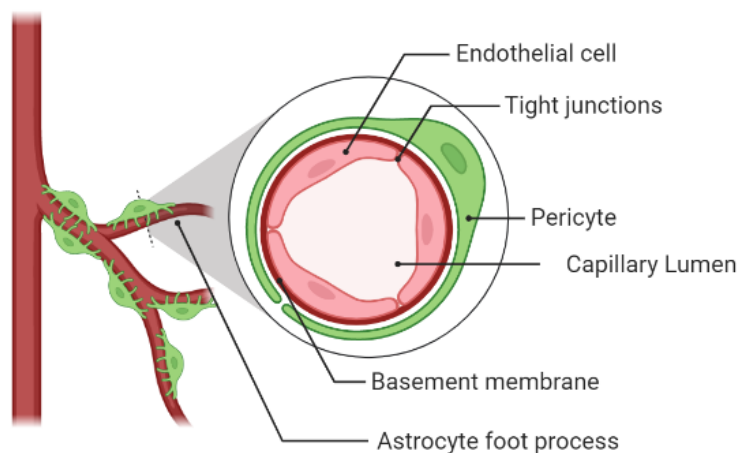


Figure 2– Schematic representation of the BBB and its constituents.

Over the last years, much effort has been engaged in understanding the structure and physiological mechanisms of BBB and its role in GBM tumors. It has been reported that GBM patients exhibit a disrupted vascular network and a high permeable BBB. This disrupted vascular network may allow the extensive presence of carcinogenic cells outside the disrupted area, however, it remains intact nearby the growing tumor [9, 54].

This disrupted vascular network formed between the cerebral tumor tissues and the capillary vessels are referred to as the blood-brain tumor barrier (BBTB) and is characterized by three microvessel populations [50]. The morphology and permeability of this barrier can be subdivided into three phases, and these are dependent on the adjacent tumor progress. In the initial phase of tumor development, the BBTB integrity is not compromised since all the nutrients required for

the tumor to grow are provided by the regular brain capillaries [9]. In the second phase, by mechanisms of angiogenesis, a neovasculature is formed permitting the cancer cells to spread out to neighbouring healthy cerebral tissues [55, 56]. In the third and final phase, the BBTB is compromised since inter-endothelial gaps are formed between the cancer endothelial cells [56].

Overall, brain tumors are characterized by an overexpression of pro-angiogenic factors, which results in increased cerebral microvascular perfusion leading to leakage through the BBB. This increases the interstitial fluid pressure, interfering with the transition of small drug molecules towards the therapeutic target as TMZ [54].

2.3.3 DNA Repair Systems and Resistance to TMZ Therapy

The most common TMZ-induced methylation lesions produced on DNA are at the N⁷ position of guanine, at the N³ position of adenine and O⁶ position of guanine. While about 65-80% of the adducts are formed at N⁷ guanine, only 8% are formed at O⁶-methylguanine (O⁶-MeG). However, despite being the least frequent, O⁶-MeG is the most mutagenic and carcinogenic alkylated base in DNA, contributing the most to the cytotoxicity of TMZ [57].

DNA repair systems are crucial for the multicellular organisms to maintain their genome integrity, once they are capable of neutralizing profound DNA damages induced by a diversity of physical and chemical factors [58]. The most important systems involved in DNA repair of alkylating agents are DNA mismatch repair (MMR), base excision repair (BER) and O⁶-methylguanine-DNA-methyl-transferase (MGMT) protein, being the later the most predominant mechanism for GBM resistance [45].

In figure 3, is represented the DNA methylation process by TMZ and the repairing nature of MGMT. First TMZ induces DNA methylation by a reactive reaction with MC in specific DNA sites. Then, the repair mechanisms of MGMT are triggered to remove the methyl group at the O⁶ position of guanine by transferring it into the cysteine-145 residue in the active internal center of the MGMT molecule, leading to DNA repair. After the DNA being properly repaired, the MGMT protein is irreversibly inactivated since it is not going to convert back to cysteine. Therefore, the MGMT protein is known as “suicide” enzyme, since the alkylated MGMT molecule only can act once. After DNA repair, MGMT is processed by an ubiquitin-proteasome, targeting the protein for degradation [59]. The ubiquitin-proteasome system is an ATP-dependent process representing the main intracellular protein degradation pathway in eukaryotes [60].

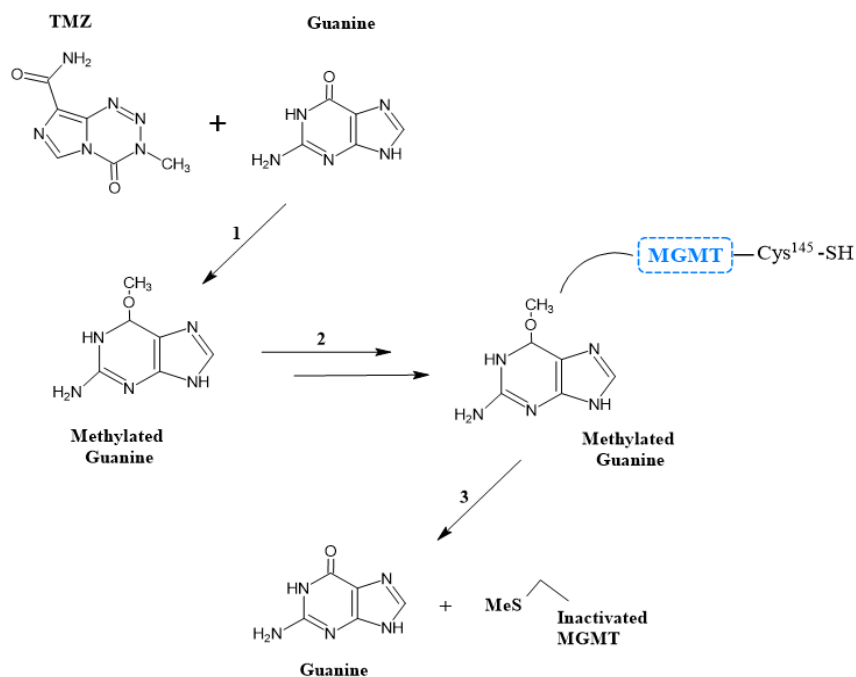


Figure 3 - (1) DNA methylation by alkylating agents, specifically TMZ; and (2) MGMT repair mechanism; (3) Restored guanine with MeS (methyl group+S) and inactivated MGMT as reaction products.

There is a demonstrated evidence of a relationship between the low expression of the MGMT protein with an increase in the sensitivity to TMZ and therapeutic efficacy in recurrent gliomas, suggesting the expression of MGMT as an indicator for chemotherapeutic susceptibility [61, 62]. Patients with deficient MGMT expression, dependent on the MGMT promoter methylation status, have shown improved survival outcomes. The methylation of the gene promoter is an epigenetic silencing mechanism that controls gene expression, and when a gene promoter is hypermethylated, the gene expression is inhibited, decreasing protein expression [63].

Taylor et al. reported that 40-60% of GBM patients show unmethylated MGMT (not-silenced gene), having elevated basal MGMT protein [62]. Thus, the methylation status of the MGMT gene promoter has been pointed as a prognostic indicator for therapeutic outcomes.

2.4 Strategies to Overcome MGMT Resistance

The lack of strategies and drugs that can improve the overall survival rate and quality of life of GBM patients, led to the major focus of the ongoing research to find ways to overcome the MGMT-mediated TMZ resistance. For this, it is crucial to understand the triggering mechanism of MGMT and how these mechanisms act. Thus, allowing their targeting with pseudosubstrates to cause MGMT deterioration [64, 65]. Below, are presented the most explored strategies/approaches and therapeutic agents to enhance the TMZ therapeutic performance through the inhibition of the MGMT enzyme.

2.4.1 MGMT Inhibitors of Gene and Protein Expression

MGMT inhibitors have been explored as a major strategy to modulate the chemotherapeutic response and decrease resistance to therapy [66]. In figure 4, it is schematized the inactivation action of adding a competitive MGMT inhibitor which transfers its O⁶-alkyl group to its cys-145 residue [67].

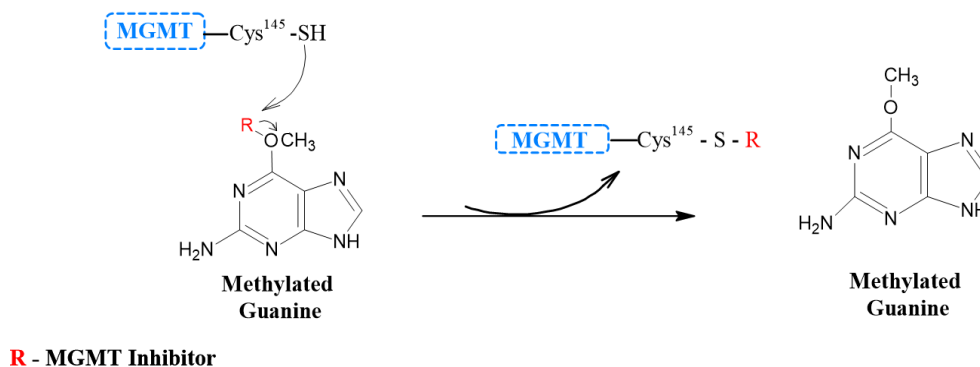


Figure 4 – Inhibition of the DNA repair mechanism by MGMT protein inactivation.

The most used MGMT inhibitors are the O⁶-benzylguanine – O⁶-BG and O⁶-(4-bromothienyl) guanine – O⁶-BTG, which are synthetic derivatives of guanine. In clinical trials, O⁶-BG was mainly used in combination with the alkylating agent TMZ, to act as a suicide inhibitor of MGMT protein by binding to the protein forcing a ubiquitin-mediated degradation, resulting in an enhanced TMZ therapeutic activity [65]. O⁶-BTG, also known as Lomeguatrib, is a pseudo-substrate and powerful MGMT inhibitor that functions similarly to O⁶-BG [68].

Both O⁶-BG and O⁶-BTG unexpectedly have fell short of the expectations over several clinical trials because they promote the MGMT inhibition in both healthy and malignant tissues. This results in a broad sensitization to the alkylating agent TMZ, and consequently, leading to an increased systemic toxicity [66]. Overall, these MGMT inhibitors are effective and can rapidly inactivate the MGMT repair mechanism, however, they are highly dose-limited due to the toxic effects and non-specific target to tumor cells causing the necessity to develop improved strategies [69].

Lately, gene therapy to modulate MGMT gene expression has been reported to have a potential therapeutic effect in GBM patients. Particularly, therapies targeting the p53 or TP53, a tumor suppressor protein, that has been proved to have a significant correlation with MGMT gene promoter methylation [70]. The tumor suppressor protein p53 is a transcription factor that regulates the expression of MGMT gene by inhibiting the MGMT promoter activity [71]. Similarly to other types of tumors, the p53 signaling pathway is impaired in GBM tumors [72]. Alterations of p53 are predominant in 25-30% of the primary GBM and in 60-70% of the secondary GBM [73].

Roos et al. recently showed that the WT p53 stimulation gene enhanced cytotoxicity of the glioma cells to alkylating drugs [74]. Thus, different strategies have been explored such as the use of DNA plasmids to transfect the p53 gene to MGMT-positive cells [71], or the administration of p53 activity enhancers such as levetiracetam [75], decitabine [76], and inhibitors of p53 negative regulators such as MDM2/MDMX [77].

2.5 MGMT Protein and BTZ Pharmacological Activity

Bortezomib (BTZ) is a FDA-approved drug acting as a selective, reversible and highly potent proteasome inhibitor. BTZ mainly acts on the nuclear factor activated by B cells - NF- κ B pathway - which, in turn, plays a critical role in tumoral cell pathogenesis [59, 60]. Recent studies have relieved that BTZ can be used as an MGMT inhibitor in brain tumors, more specifically by blocking the hyperactive NF- κ B activity in GBM cancer cells [78, 79].

NF- κ B is a protein complex that is responsible for controlling the transcription of DNA, being involved in the transcriptional regulation of MGMT gene. NF- κ B transcriptional regulation of MGMT acts by specific binding sites within of MGMT gene promoter region. To control this overactivity of NF- κ B in tumor cells, BTZ acts as a stabilizer of crucial endogenous inhibitors [78]. Consequently, with the decrease of the MGMT gene transcription, the expression of the MGMT protein is decreased, inhibiting the DNA repair. Figure 5 represents schematically the inhibition activity of antineoplastic BTZ throughout NF- κ B associated genes and pathways.

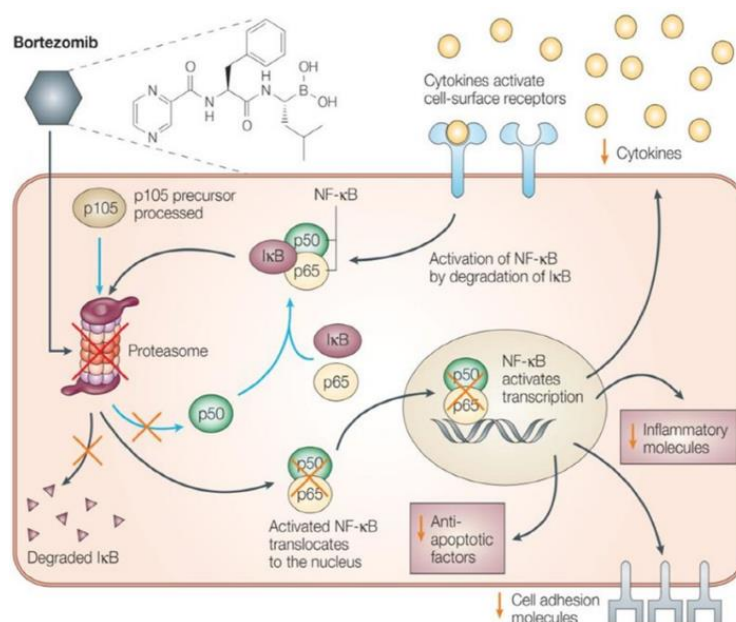


Figure 5 – Proteasome inhibitor BTZ mechanism through blocking the NF- κ B activity [80].

Thus, co-therapy of TMZ with molecular agents such as BTZ capable of inactivating the MGMT protein can increase the sensitivity to TMZ and therefore increase the efficacy of the therapy. The systemic administration of multiple pharmaceutical drugs, known as cocktail chemotherapy, has been arousing some interest, more particularly for cancer therapy. However, it presents some limitations. When two or more drugs are administered, different pharmacokinetics can cause discrepancies in drug concentration within the tumor site. Specifically, for BTZ, its systemic administration can potentiate its toxicity for healthy tissues, as well as, induce the inhibition of MGMT DNA repair activity in healthy tissues.

Using DDS for the simultaneous administration of TMZ and BTZ can improve the quality of treatment. Co-delivery of two or more bioactive components, with therapeutic potential, offers multiple health benefits by enhancing the treatment, as well as, to minimize side effects. The resort to this type of co-delivery system allows the manipulation of drugs properties, pharmacodynamics and kinetics, biodistribution, cellular uptake and therapeutic index of the bioagent [69] as will be further discussed in the following sections.

2.6 Nanomedicine

For the past few decades, nanotechnology has been a major area of research to develop innovative techniques and products that can help to improve our quality of life. In particular, nanomedicine resorts to nanomaterials with unique physicochemical, properties with dimensions within the nanoscale (10^{-9} m) [79]. The challenge of the current chemotherapeutic strategies is their nonspecific targeting and the possibility of affecting healthy cells, triggering multiple drug resistance mechanisms [81]. Thereby, the application of nanotechnology for the delivery of anti-cancer therapeutic agents through drug delivery systems (DDS) is an urgent need.

DDS can overcome some obstacles, when compared to the conventional chemotherapy, due to DDS characteristics, such as, improved drug bioavailability, facilitated bioelimination/biodegradation and overall improved therapeutic efficiency. In addition, each type of cancer cell is characterized by its diversity and heterogeneity, which leads to the need for tailor-made therapeutic approaches. Over the last decades, is notorious the emerging search for the most suitable nanomaterials to be employed as nanocarriers in co-delivery systems.

Several types of nanocarriers have been studied based on their physicochemical properties. Nowadays, liposomes, micelles, dendrimers, polymeric NPs, and solid lipid NPs are the typical and most used nano-based delivery carriers normally within a size range of 10-200 nm. Tailor-made nanostructures enable the development of hybrid NPs with distinct coating and surface functionalization can be designed to a variety of specific target tumoral niches leading to local

uptake of the drug by malignant tissues [79]. Below in figure 6 is represented some of the main used nanocarriers used in DDS.

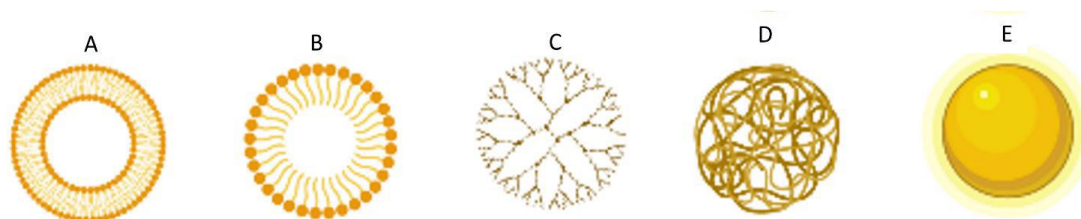


Figure 6 – Illustration of the different types of NPs used in nanomedicine: A – liposome; B – micelle; C – dendrimer; D – polymeric NP (nanocapsule; nanosphere); E – metallic NP.

Organic NPs are frequently used for surface functionalization because in their chemical structure they have terminal surface groups. Polymeric and polyester NPs have been used for the co-delivery of drugs and siRNA due to their tenability and high transfection rate of DNA and siRNA. Some examples of polymers used are poly (ethylene amine) (PEI), polycaprolactone (PCL), poly (D, L-lactic-co-glycolic) (PLGA), polyesters, poly-lactic acid (PLA). PLGA NPs are widely popular due to their unique properties. PLGA is degraded naturally generating lactic acid and/or glycolic acid as degradation products that are subsequently metabolized in the body producing non-toxic products as carbon dioxide, water and nitrogen, via citric acid and pyruvate cycle [82]. It is believed that these polymers do not affect normal cellular function due to their biocompatibility and biodegradability [83]. In addition, inorganic NPs, such as, gold NPs, iron oxide NP, carbon nanotubs and quantum dots, are also immerging due to their optical absorption, magnetic characteristics and fluorescence [84].

2.6.1 Drug Delivery Systems for GBM Treatment

The two biological barriers, BBB and BBTB, represent the major obstacle to drug brain delivery. Therefore, strategies to circumvent the BBB/BBTB have been pursued [9]. For this purpose, two major approaches can be employed, the first approach leans on passive targeting, taking advantage of the enhanced permeability and retention (EPR) effect. The second approach relies on an active targeting strategy by the attachment of specific surface ligands [85]. Tumor tissues exhibit an abnormal vascularization permeabilization and dysfunctional lymphatic system and this effect is known as EPR effect. Near the tumor site this effect is more susceptible to occur due to dysfunctional lymphatic system. In figure 7 is represented both normal and dysfunctional lymphatic drainage system that ultimately leads to EPR effect [86].

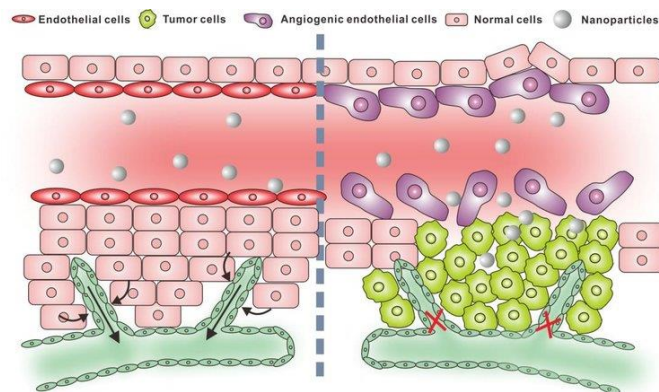


Figure 7 – Contrast with a normal lymphatic system and a dysfunctional lymphatic system resulting in EPR effect [86].

The passive targeting strategy approach offers limited advantages when applied to treat CNS disorders, including GBM. The vascular gap ranges in the brain are between 7-200 nm, representing a very impermeable BBB, hindering the transport of NPs above 200 nm across this barrier [87]. For this fact, few research groups have used passive targeting nanosystems for the drug delivery to GBM damaged tissues [88].

Sebastian et al. (2004) reported polysorbate-80 coated polybutylcyanoacrylate NP or polysorbate-80 coated poly (isohexyl cyanoacrylate) NPs loaded with doxorubicin (DOX). According to the authors, the results obtained in *in vivo* experiments reveal that the animals treated with the DOX NPs exhibited a decrease on the tumor size, proliferation index, tumor vessels density and necrotic zones [88, 89]. Using TMZ as a therapeutic agent, polysorbate-80 coated polybutylcyanoacrylate NPs, were also reported. As expected, the results revealed an increased TMZ accumulation on the brain tumor tissue. As a novel strategy for the treatment of gliomas, curcumin-loaded lipid core nanocapsules were developed. It was observed that the tumor size decreased and the survival rate increased [88].

Active targeting is a gold standard approach targeting specific receptors on the BBB capillaries that play a major role in transferring the designed nanocarriers from blood circulation into the brain. Many GBM treatment nanostructures focus on a dual targeting approach, they are designed with the purpose to improve both infiltration across the BBB and the drug uptake by the brain tumor cells [90].

In the active targeting strategies, the surface of the NPs are functionalized with specific ligands such as antibodies, proteins, peptides and nucleic acids. This allows the selective binding between the nanostructures and specific receptors and biomolecules that are overexpressed in the tumor site [88]. The most prevalent targets in GBM are transferrin (Tf), folate, chlorotoxin (CTX), angiopep-2, EGFR, VEGF, $\alpha v \beta 3$ integrins, matrix metalloproteinases (MMP) and vascular cell adhesion molecule [91]. Figure 8 illustrates the main structural and actuation differences between the nanostructures for passive and active targeting.

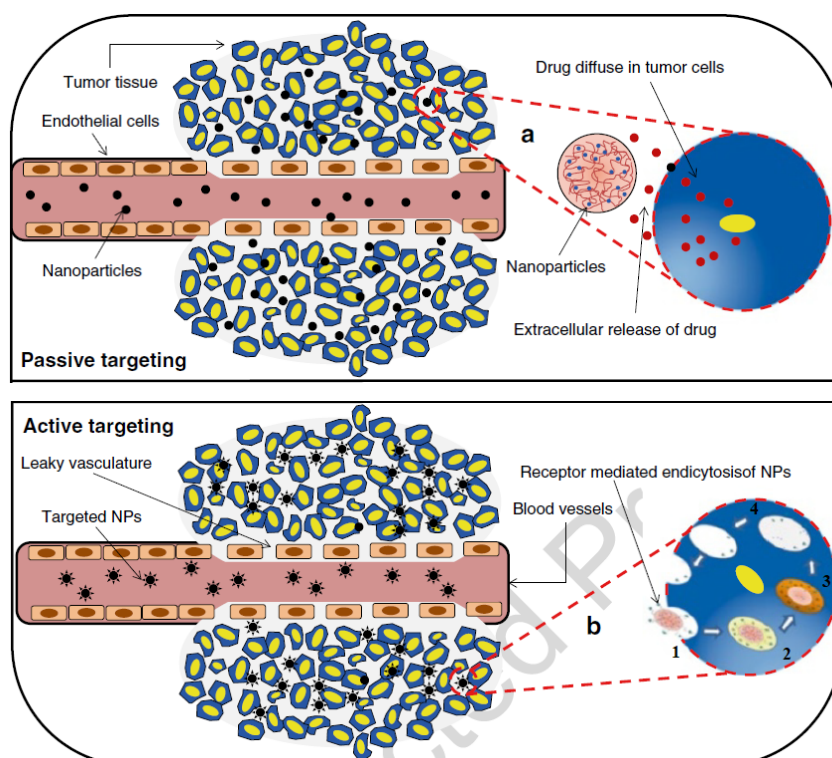


Figure 8 – Illustration of the mechanisms of passive and active targeting in nanostructures loaded with drugs; a) the NPs pass diffusively through the BBB by the leaky vasculature and accumulate in tumor tissue; b) 1- targeted NPs binds to the cellular receptors; 2 – NP enters in the intracellular space inside an endosome; 3- endosomal escape and local drug release. Adapted from [92].

CTX peptide is one of the most used target ligands for GBM since it has a high affinity for chloride channels and MMP-2 isoforms which are upregulated in GBM brain tissues. Fang et al. [93] synthesized CTX-modified chitosan NPs loaded with TMZ for GBM therapy. The authors concluded that these nanostructures could easily penetrate the BBB, being widely distributed in the brain tissue. Angiopep-2 as a targeting ligand was reported by Xin et al. [94]. This is known for its ability to interact with the lipoprotein receptor-related protein and by its dual targeting capacity, enhancing endocytosis through the BBB and glioma cells. PEG-poly- ϵ -caprolactone NPs conjugated with angiopep-2 and loaded with paclitaxel revealed increased uptake in glioma tumors during *in vivo* studies.

Another widely used ligand is Tf due to the overexpression of Tf receptors (TfR) on the BBB and GBM cells. Similar to angiopep-2, Tf also works as a dual target agent, and its incorporation on the external surface of the nanocarrier is proved to improve the cell uptake increasing the drug accumulation in the tumor cell cytoplasm [50, 95]. Luo et al. (2019) used Tf to modify the surface of porous silicon NPs for the targeted delivery of DOX to treat GBM tumors [96].

2.6.2 Drug Delivery Systems to Overcome MGMT Resistance in GBM Treatment

Due to the advantages of nanotechnology in the delivery of therapeutic drugs to GBM tumors, different nanosystems have been proposed to target the MGMT-mediated resistance mechanism aiming to improve therapeutic outcomes. Two main strategies have been explored, the first focused on the delivery of drugs that inhibit directly the MGMT protein (table 1) and gene therapy to inhibit the MGMT gene transcription (table 2).

Table 1 - Nanosystems for the delivery of MGMT inhibitors to overcome the MGMT DNA repair mechanisms in GBM therapy.

Nanocarrier	Coating	Targeting moiety	Loaded cargo		Combination with free alkylating agent	Main conclusions	Ref.
			MGMT inhibitor	Anti-GBM drug			
PLGA NPs	Chitosan	n.a.	O ⁶ BG	Carmustine	n.a.	Co-therapy improved cell sensitivity to carmustine in MGMT-positive cells. Encapsulation in NPs improved drug biodistribution and therapeutic effect in intracranial tumor-bearing rats.	[97]
PLGA NPs	n.a.	n.a.	O ⁶ BG	TMZ	n.a.	NPs with optimal physicochemical properties for brain delivery and suitable release kinetics.	[98]
PLGA nano-fibers	n.a.	n.a.	O ⁶ BG	TMZ and Carmustine	n.a.	Improved tumor growth inhibition by MGMT inhibition and with higher treatment efficacy than clinically available regimens.	[99]
Liposomes	PEG	n.a.	O ⁶ BG derivative	n.a.	n.a.	Liposomes with high drug loading and suitable release kinetics. Suitable dimensions for brain delivery. Reduction of MGMT protein levels in TMZ-resistant glioma tumors, leading to improved therapeutic outcomes.	[64, 100]
Iron oxide NPs	PEG-chitosan	CTX	O ⁶ BG	n.a.	TMZ	NPs induced the suppression of the MGMT activity in GBM cells. Improved TMZ effect in intracranial tumor-bearing mice with reduced O ⁶ BG systemic toxicity.	[101]
Iron oxide NPs	PEG	n.a.	O ⁶ BG analogue	n.a.	TMZ	NPs revealed a pH-dependent <i>in vitro</i> release profile. The NPs are efficiently taken up by GBM cells and can potentiate the MGMT inhibitory activity of the drug, enhancing TMZ therapeutic effect.	[102]

Iron oxide NPs	HA	CTX	n.a.	GEM	n.a.	Effectively cancer cell targeting with high therapeutic potential; High ability to cross the BBB with prolonged blood half-life; GEM activity proved to independent of MGMT expression;	[103]
-----------------------	----	-----	------	-----	------	---	-------

Abbreviations: carmustine (BCNU); dialdehyde modified O⁶-benzylguanosine (DABGS); chlorotoxin (CTX); Gemcitabine (GEM); hyaluronic acid (HA).

PLGA NPs have been the most explored nanocarriers for drug delivery for GBM therapy. Lili et al. (2013) developed chitosan surface-modified PLGA NPs loaded with BCNU and O⁶-BG. The group conclude that the uptake of the NPs in rat glioma cells increased with the surface modification and decreased with particle size. *In vivo* experiments using rats with intracranial tumors with high MGMT levels further revealed that the co-encapsulation of O⁶-BG and BCNU enhanced the MGMT inactivation, proving that the co-administration of BCNU and O⁶-BG exhibits higher anti-GBM efficacy than BCNU alone [97]. Ramalho et al. (2019) developed PLGA NPs for the co-delivery of O⁶-BG and TMZ. The NPs were modified with a monoclonal antibody targeting the TfR to increase specificity. *In vitro* experiments with human GBM cells showed that surface functionalization increased the cell uptake by the target cells, and that the concomitant therapy with the MGMT inhibitor increased TMZ sensitivity in TMZ-resistance cells by 10-fold [98]. Another group, Liu et al. (2018) developed PLGA nanofibers for controlled and sustained release of O⁶-BG and two alkylating agents, TMZ and carmustine (BCNU). *In vivo* experiments using rats with intracranial tumor xenografts showed improved treatment efficacy, with O⁶-BG enabling the inhibition of MGMT, therefore increasing the sensitivity to TMZ and BCNU [99].

Lipidic-based NPs, such as, liposomes have also been proposed to overcome MGMT-mediated resistance in GBM therapy. Signorell et al. (2018) developed PEGylated liposomes loaded with O⁶-BTG to revert chemoresistance using a series of O⁶-BTG molecules conjugated with distinct alkyl chain lengths [100]. Plus, the prepared NPs were conjugated with PEG to enhance their stability. *In vitro* experiments confirmed that this formulation enabled the sustained release of O⁶-BTG derivatives and therefore, it is a possible candidate to overcome MGMT-induced chemoresistance in GBM therapy. Later, the same group evaluated the *in vivo* performance of this nanoformulation in a intracranial tumor bearing mice to assess if these nanocarriers would be suitable for BBB permeability through the transient opening by focused ultrasound [64]. The results revealed that the liposomes were able to improve drug accumulation in the tumor tissue, and when combined with chemotherapy with TMZ the survival of the tumor-bearing mice was prolonged significantly.

Metallic NPs are also suitable candidates for GBM therapy. Stephen et al. (2014) developed superparamagnetic iron oxide NPs for O⁶BG local delivery [101]. To develop an active drug delivery targeting strategy, the NPs' surface was conjugated with CTX peptide. To provide a redox-responsive performance, the NPs were coated with a PEG-chitosan co-polymer. *In vitro* studies using MGMT-positive human GBM cells demonstrated the suppression of the MGMT activity and the enhanced sensitivity to TMZ therapy. The authors were able to conclude that the NPs showed no systemic toxicity in mice bearing intracranial tumors, and overall improved the therapeutic efficacy by suppressing MGMT activity. Later, the same group reported the use of these iron oxide NPs to deliver a pH-sensitive O⁶BG analog, the dialdehyde modified O⁶BG (DABGS)

[102]. The obtained NPs displayed a controlled drug release mediated by a pH-dependent mechanism with maximum release at acidic pH mimicking the tumor intracellular environment and displayed minimal release at simulated blood-circulation pH. *In vitro* studies using MGMT-positive human GBM cells demonstrated the suppression of the MGMT activity and the enhanced sensitivity to TMZ therapy.

Mu et al. (2016) developed iron NPs conjugated with a chemically altered gemcitabine (GEM) that acts as a deoxycytidine-triphosphate-competitive agent that inhibits DNA chain elongation leading to cell death [103]. GEM activity in brain tumors is independent of the MGMT expression, and therefore can be used for patients with unmethylated MGMT gene promoter [104]. For an active targeting drug delivery strategy, the surface of the NPs was modified with the CTX peptide. This formulation showed ability to cross the BBB and to accumulate in the brain tissue of healthy mice after *i.v.* injection. For cytotoxicity *in vitro* studies, two human GBM cell lines were used to represent different MGMT expressions, and it was verified that loaded drug had similar toxicity in both MGMT-positive and negative cell lines as expected. For *in vivo* studies using intracranial tumor-bearing mice, the NPs were tagged with a fluorescent marker, and the authors verified a higher accumulation of the NPs in the tumor sites.

Table 2 –Nanosystems for gene therapy to suppress the MGMT activity in GBM therapy.

Nanocarrier	Coating	Targeting moiety	Molecular target	Loaded cargo	Combination with free alkylating agent	Main conclusions	Ref.
Liposome	n.a.	n.a.	MGMT gene	siRNA	TMZ	MGMT-siRNA lipoplexes enhanced TMZ cytotoxicity in TMZ-resistant cells and showed no effect in TMZ-sensitive cells. The liposomes improved TMZ's therapeutic effect in both subcutaneous and intracranial tumors. Although no toxicity was observed in rats and pigs, the distribution in the brain tissue proved to be insufficient.	[105, 106]
Liposome	n.a.	anti -TfR ScFV	p53 suppressor gene	p53 plasmid	TMZ	The liposomes showed ability to permeate the BBB and target resistance stem cells <i>in vivo</i> . Improved tumor sensitization to TMZ leading to increased tumor growth inhibition and animal survival	[107, 108]
Lecithin-DSPE-PLGA NPs	PEG	RGD	MGMT gene	CRISPR/Cas9 plasmids	TMZ	NPs efficiently transfected the plasmids to cells, leading to a low MGMT expression and improved therapeutic effect in intracranial tumors-bearing mice.	[109]
PLGA micelles	PEG	RGD	Suppressor protein p53	sPMI	TMZ	NPs were able to cross the BBB and accumulate in intracranial tumors in mice model, and sPMI encapsulation led to an enhanced TMZ sensitivity.	[110]

PLGA micelles	PEG	n.a.	p53 sup-pressor gene	Decitabine	TMZ	Decitabine-loaded micelles allowed for the controlled release in the intracellular environment and promote the TMZ cytotoxicity due to the suppression of the MGMT activity.	[111]
Iron oxide NPs	Dextran	CTX	MGMT gene	siRNA	TMZ	The developed NPs accumulate in the brain tumor tissue and effectively reduced tumor growth. The inhibitory effect was more prominent for CTX peptide than for MGMT siRNA.	[112]
Iron oxide NPs	n.a.	n.a.	P52 gene	pEGFP/p53	TMZ	Supermagnetic NPs induce total apoptosis by exposing to magnetic force; pEGFP/p53 is a coding for the EGFP a green fluorescent protein, which contain the p53 gene; magnetic treated NPs showed decrease in p53 protein levels of expression.	[113]

Abbreviations: small interference RNA (siRNA); tripeptide Arginine, Glycine, and Aspartate (RGD); Lipid-polymer hybrid NPs (LPHNs); Transferrin (Tfr); plasmid enhanced green fluorescence protein (pEGFP);

Several groups proposed NPs for gene therapy to overcome MGMT-mediated resistance in GBM. Cationic liposomes are commonly used non-viral gene delivery systems for small-interfering RNA (siRNA), and Kato et al. (2010) proposed the use of commercial liposomes (LipoTrust) for the delivery of anti-MGMT siRNA. *In vitro* experiments using human GBM cells revealed that the liposomes loaded with MGMT-siRNA can downregulate the MGMT expression, resulting in an enhanced TMZ therapeutic sensitivity. *In vivo* experiments using subcutaneous xenograft tumor- and intracranial tumor-bearing mice showed enhanced TMZ cytotoxicity for the siRNA- liposomes when compared with TMZ alone [105]. Later, the same group, aimed to evaluate the safety of this formulation for convection-enhanced delivery (CED) [106], to verify if these lipoplexes were suitable for clinical use for GBM therapy. *In vivo* studies with rats and pigs revealed no toxic side effects, such as, neurological dysfunction or histological abnormalities, but poor biodistribution was verified, leading to the conclusion that this CED approach was not suitable for the delivery of the developed lipoplex.

Kim et al. (2014) developed cationic liposomes to modulate MGMT-mediated resistance. For specific GBM targeting, the nanocarriers were modified with a single-chain variable fragment (scFv) against the Tfr [107]. The scFv has been used instead antibodies due to their improved capacity to pass through the BBB owing to their smaller size [114]. The authors aimed for the co-delivery of TMZ and the exogenous wild-type tumor suppressor p53 gene to downregulate MGMT expression, potentiating TMZ's effects. *In vitro* studies in p53-mutant human GBM cells confirmed that the addition of p53 gene increased the antitumor efficacy of TMZ resulting in an enhanced antiproliferative activity of the drug. In addition, the developed liposomes were able to target the glioma stem cells linked to GBM recurrence and treatment resistance. Later, the same research group evaluated the ability of the developed nanoforumulation to sensitize highly TMZ-resistant GBM tumors to TMZ in mice bearing intracranial tumors. The obtained results allowed concluding that due to the specific tumor-targeting ability and BBB permeability, the developed liposomes improved tumor growth inhibition and prolonged animal survival [108].

Yang et al. (2021) developed a lipid-polymer hybrid NPs coupled with RGD peptide, as nanocarrier to the delivery of CRISPR/Cas9 plasmids targeting the MGMT gene to overcome TMZ resistance [109]. *In vitro* release assays in physiological conditions revealed a sustained release of plasmids. The authors also confirmed that the produced NPs were able of downregulating the MGMT expression. Then, they used ultrasound microbubbles to facilitate the gene delivery passing through the BBB. *In vivo* experiments using mice bearing intracranial tumors demonstrate the NPs ability to downregulate the expression of MGMT with a highly specific targeting ability due to the use of cRGD sequence.

Chen et al. (2015) developed PLGA micelles conjugated with RGD for the delivery of a peptide antagonist of both MDM2 and MDMX (sPMI). MDM2 and MDMX are negative regulators

of the p53 signaling pathway and are usually overexpressed in MGMT tumors being responsible for blocking the p53 activity and targeting p53 for degradation leading to overregulation of the MGMT gene transcription. The nanoformulation was evaluated in *in vivo* using mice bearing subcutaneous and intracranial tumors, and the results demonstrated that combined therapy of TMZ with sPMI-loaded micelles revealed better therapeutic outcomes than co-therapy of TMZ with free sPMI. These results also validate the possible combination of therapy using p53 activators and alkylating agents [110].

Cui et al. (2015) synthesized pegylated PLGA NPs to deliver decitabine for GBM therapy. Decitabine is involved in blocking the DNA methylation, therefore inhibiting p53 gene-silencing, promoting the p53 gene transcription. Since the p53 inhibits the MGMT transcription, decitabine downregulates MGMT expression. This formulation takes advantage of the tumors' acid environment, enabling the PLGA-PEG degradation and decitabine release. *In vitro* cytotoxicity studies using MGMT-positive GBM cells revealed an efficient cellular uptake, and that pre-treatment with decitabine-micelles sensitized the cells to TMZ's activity, due to the suppression of the MGMT activity being more efficient than the combination therapy with free decitabine and TMZ [111].

Yoo et al. (2014) also reported the use of anti-MGMT siRNA for GBM therapy. The authors developed iron oxide NPs functionalized with CTX for its delivery. Experiments with mice bearing intracranial tumors proved that this formulation enhanced sensitivity to TMZ by silencing the MGMT mechanisms and decreasing endogenous MGMT levels, but also enabled the unexpected observation of the cytotoxic properties of CTX [112].

Eslaminejad et al. (2017) also proposed iron oxide NPs for GBM gene therapy. The NPs were loaded with a p53 recombinant plasmid modified with a green fluorescent protein to monitor the anchor peptide binding. *In vitro* experiments using human GBM cells showed that the developed NPs were able to efficiently transfect the gene to the target cells, leading to an increase in apoptosis that was enhanced by the induction of magnetic forces when compared to non-exposed cells. By fluorescence microscopy they were able to conclude that the exposure to magnetic fields directly reflects in decreased p53 protein expression levels [113].

Chapter 3

Materials and Methods

In this chapter, are exposed all the materials and methods used for the NPs preparations, as well as, for their physicochemical characterization, stability and cytotoxicity studies.

3.1 Materials

Polyvinyl alcohol 4-88 (Mowiol ® 4-88, MW 31,000) (PVA), Dichloromethane (MW 84.93; purity = 99%) (DCM), PLGA Resomer® RG 503 H (50:50; MW 24,000 – 38,000), carbodiimide (EDC) (MW 191.70), holo-Transferrin human (MW 80.00, purity \geq 98%), phosphate-buffered saline (PBS) and acetic acid (\geq 98%, MW 60.05), were purchased from Sigma Aldrich. Ethyl acetate (99.6%, ACS reagent, MW 88.11) (EA) was acquired from BioVision, TMZ (MW 194.15, purity \geq 99%) and BTZ (MW 384.24, purity >99%) were obtained from Selleck Chemicals (Munich, Germany). Trypsin (Gibco™ TrypLE™) and fetal bovine serum (Gibco™ FBS), were purchased from Fisher Scientific (Hampton, NH, USA). High-glucose Dulbecco's Modified Eagle medium (DMEM) was purchased from Capricorn Scientific (Ebsdorfergrund, Germany). Penicillin-Streptomycin solution (x100) was purchased from Biowest LCC (Riverside, MO, USA). Amphotericin B was purchased from Corning Inc. (New York, NY, USA). Trypan blue (\geq 70%, MW 960.80) was purchased from Biochem Chemopharma (Cosne-Cours-sur-Loire, France). Dimethyl sulfoxide (DMSO) (\geq 99.9%, MW 78.13) was purchased from VWR international (Radnor, PA, USA). Pierce™ BCA Protein Assay Kit, Trichloroacetic acid (TCA) (99%, MW 163.38). Tris(hydroxymethyl)aminomethane (\geq 99.8%, MW 141.14), Sulforhodamine B (SRB) (MW 580.66) were purchased from Sigma-Aldrich (St. Louis, MO, USA). Dimethyl sulfoxide (DMSO) (\geq 99.9%, MW 78.13) was purchased from VWR international (Radnor, PA, USA).

3.2 Preparation of TMZ+BTZ Loaded PLGA NPs

The TMZ+BTZ loaded PLGA NPs were prepared using the single emulsion-solvent evaporation technique [115]. An organic solution of EA containing a known amount of PLGA, 0.5 mg of TMZ and 0.5 mg of BTZ was prepared. 2 mL of an aqueous solution of a known amount of PVA, was added drop-by-drop to the previously prepared organic solution. The emulsion was vortexed (Genius 3, ika®vortex, Germany) and sonicated (UP400S ultrasonic processor, Hielscher, Berlin, Germany) with 3 cycles of 10 seconds on/off each at a 40% of amplification and an ultrasonic frequency of 24 kHz. The ultrasound waves allow the formation of nanosized droplets during the sonication cycles.

The samples were maintained in continuous agitation at 7,000 rpm (Colosquid, ika®, magnetic stirrer) until complete evaporation of the organic solvent. Then, the NPs suspension was stored at 4 °C to avoid the aggregation and to promote stability. To recover the NPs, a sequence of centrifugation steps was performed with increasing speeds from 5,000 to 14,500 rpm and increasing duration from 2 to 15 minutes. The formed NPs pellet was resuspended in 1.0 mL of ultrapure water for subsequent analysis. The supernatant was saved for non-encapsulated drugs quantification.

3.3 Experimental Design and Protocol Optimization

In conventional process optimization, independent studies are performed to visualize the effect of one experimental parameter, while the other variables must remain constant. However, this conventional approach is expensive and time-consuming. In this way, design of experiment (DoE) is a suitable alternative to optimize the NPs preparation protocol in a faster and accurate manner. The experimental design enables the full knowledge of the relationship between the experimental parameters (independent variables) and the studied responses (dependent variables). With this method, the effect of several experimental factors can be evaluated simultaneously using a reduced number of experiments, leading to an improved quality of the data obtained from the experiment.

Several types of experimental design can be applied, depending on the intended purpose and the variables under study. However, one of the most commonly implemented DoE to optimize nanoformulations is the two-level factorial design (2^n). In these designs, each experimental variable is varied in a high and low level, coded by -1 and +1, respectively. Then, the relationship between the experimental variables and each studied response is obtained by the following polynomial regression [116].

$$Y = \beta_0 + \sum_{i=1}^k \beta_i X_i + \sum \beta_{ij} X_i X_j, \quad (1)$$

Where, Y is the predicted response; β_0 is the intercept term and the remaining term; $X_{i,j}$ are the independent variables levels; and $\beta_{i,j}$ are the fitted coefficients for $X_{i,j}$.

When the information obtained is insufficient to extract a conclusion, an augmented version to the previously implemented model can be applied. The most used approach is the Central Composite Design (CCD), where two levels are added and coded by $-\alpha$ and $+\alpha$.

In this work, a 2^4 full factorial design (FFD) was initially implemented using the Design Expert software (11.1.2.0 version, Stat-Ease Inc., Minneapolis, USA). In preliminary studies, the most relevant experimental parameters for NPs preparation were selected (table 3) as the dependent variables and varied in two levels [low (-1) and high (+1)]. The chosen independent variables were the quantity of PLGA, the percentage of PVA, the number of sonication cycles and the organic solvent/water ratio. For the design augmentation a CCD was implemented by adding star points to the model, where the experimental factors were varied in 2 extra levels, ($-\alpha$ and $+\alpha$) with an $\alpha = 1.54671$. The α value was automatically determined by the design expert software after choosing a factorial orthogonal quadratic design augmentation.

Table 3 - Process and formulation of the parameters of the Experimental Design used.

Parameters	Component	Units	Applied Level				
			$-\alpha$	-1	0	+1	$+\alpha$
X_1	m_{PLGA}	mg	4.5	10	20	30	35.5
X_2	PVA	%	0.09	0.5	1.25	2	2.4
X_3	sonication cycles	unit	1	2	4	6	7
X_4	O/W ratio	mL	0.43	0.5	0.625	0.75	0.82

Note: m_{PLGA} - PLGA mass; PVA – percentage of PVA; sonication cycles – number of sonication cycles of 10 seconds each; O/W ratio – ratio between the volume of organic solution and the inorganic solvent.

The studied dependent variables were the NPs size, the polydispersity index (PDI), the zeta potential values and the encapsulation efficiency (EE) of both drugs. For the initial FFD experimental design, 19 formulations were prepared including 3 replicas for the central point. Then, the DoE was augmented, and 8 additional formulations were prepared (run 20-27). To avoid bias, the order of the formulations was randomly set. The experimental plan, as well as the results are presented in table 4.

Table 4 - Experimental plan overview and results. The experimental levels (low, center and high) are represented by the coded values of -1, 0, +1, respectively from 1 to 19 and $-\alpha$, 0, $+\alpha$ from 20 to 27.

Run order	Coded independent variables				Measured dependent variables				
	X ₁	X ₂	X ₃	X ₄	Mean diameter (nm)	PDI	Zeta Potential (mV)	TMZ	BTZ
1	0	0	0	0	147.9	0.080	-17.4	60.3	67.8
2	-1	-1	+1	+1	192.8	0.024	-19.9	73.1	81.6
3	+1	+1	-1	-1	196.2	0.182	-19.1	81.0	56.0
4	+1	+1	+1	-1	148.1	0.041	-18.8	96.1	43.6
5	+1	+1	-1	+1	202.7	0.199	-21.7	71.4	51.8
6	-1	-1	+1	-1	194.1	0.040	-21.7	39.9	90.1
7	-1	+1	+1	-1	136.3	0.078	-22.5	43.9	84.7
8	-1	+1	+1	+1	126.7	0.064	-20.7	52.3	77.7
9	+1	-1	+1	-1	203.9	0.042	-23.0	92.0	76.5
10	-1	-1	-1	-1	174.4	0.055	-22.7	61.2	89.4
11	+1	+1	+1	+1	280.9	0.219	-23.1	32.8	82.0
12	+1	-1	+1	+1	284.7	0.178	-21.7	78.5	86.7
13	0	0	0	0	149.7	0.036	-19.8	66.8	95.7
14	-1	+1	-1	+1	142.4	0.072	-19.0	42.4	94.2
15	+1	-1	-1	-1	241.9	0.170	-21.4	87.6	87.7
16	+1	-1	-1	+1	256.8	0.186	-23.4	79.5	98.7
17	-1	+1	-1	-1	151.6	0.037	-17.2	53.9	73.7
18	0	0	0	0	155.6	0.046	-21.5	97.3	66.6
19	-1	-1	-1	+1	284.4	0.239	-19.4	56.5	85.1
20	$-\alpha$	0	0	0	150.8	0.036	-24.2	36.9	52.7
21	$+\alpha$	0	0	0	165.6	0.083	-21.7	18.8	84.7
22	0	$-\alpha$	0	0	903.1	0.236	-22.8	52.9	80.0
23	0	$+\alpha$	0	0	148.0	0.032	-19.7	57.9	22.2
24	0	0	$-\alpha$	0	172.3	0.011	-15.5	95.0	41.9
25	0	0	$+\alpha$	0	153.2	0.060	-21.2	16.0	89.4
26	0	0	0	$-\alpha$	145.0	0.054	-24.4	46.5	70.3
27	0	0	0	$+\alpha$	162.0	0.050	-22.7	55.7	98.3

The mathematical regression model was fitted independently to each response variable, and then ANOVA (Analysis of Variance) was used for the statistical analysis of each response regression model. p-values lower than 0.05 were considered significant, at a 95% confidence interval.

3.4 Preparation of the Transferrin Functionalized NPs

The TMZ+BTZ-loaded PLGA NPs were conjugated with transferrin (Tf) by a carbodiimide coupling reaction, as represented in figure 9A. In this reaction, the PLGA carboxylic groups are activated. Later, the activated carboxylic groups bind to the primary amine of Tf, leading to the formation of an amide bond, in a reaction known as a chemical click reaction [117, 118].

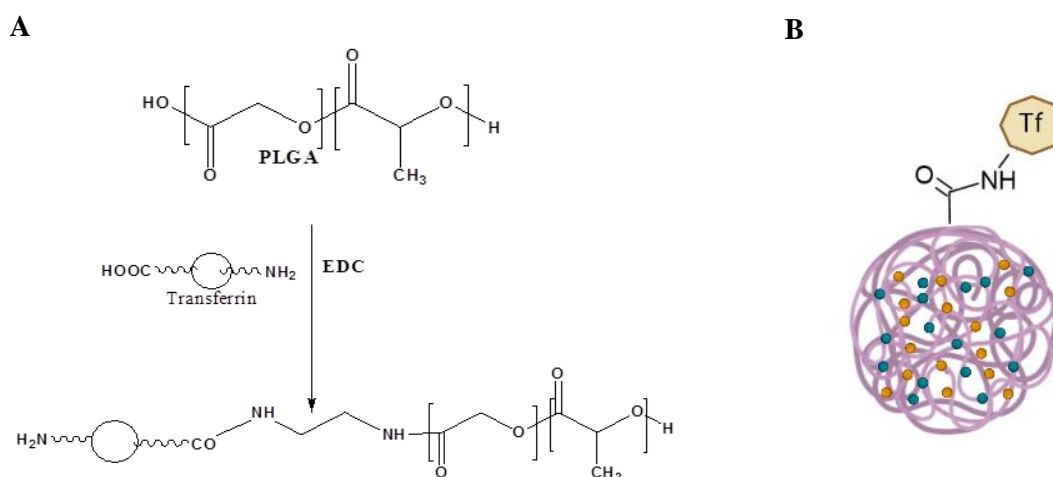


Figure 9 – (A) Carbodiimide Coupling reaction for Tf conjugation [118]; (B) TMZ+BTZ PLGA NPs conjugated with Tf. The blue dots represent the TMZ and the orange dots represent the BTZ.

An N-(3-Dimethylaminopropyl)-N'-ethylcarbodiimide hydrochloride (EDC) aqueous solution was added to the NPs suspension at a 20x molar excess [119]. The NPs and the EDC reagent were continuously agitated for 30 minutes at room temperature. Then, an aqueous solution of Tf was added to the NPs (2x molar excess). The final goal was to obtain around 100 molecules of Tf per NP. The prepared solution was kept in continuous agitation for 1 hour at room temperature. After 1 hour, to remove the excess of EDC and the unbounded Tf, the Tf-conjugated PLGA NPs were collected by subsequent centrifugation steps. Then, the Tf-modified TMZ+BTZ-loaded PLGA NPs were resuspended in ultra-pure water and stored at 4 °C. The unbounded Tf in the supernatant was quantified by a bicinchoninic acid (BCA) protein assay to determine the conjugation efficiency as described in section 3.7.

3.5 NPs Physicochemical Characterization

The parameters evaluated for the physicochemical characterization of the prepared NPs were the size in nanometers (nm), polydispersity index (PDI) and zeta potential in millivolts (mV). The obtained data were analyzed by the ZetaSizer Software (version 8, Malvern Instruments, UK).

3.5.1 Dynamic Light Scattering

Dynamic light scattering (DLS) is a non-invasive technique that relies on the ability of the NPs in suspension to move by Brownian motion, directly related to their size and molecular weight. The velocity of the Brownian motion leads to the laser light to be scattered at different intensities and ultimately producing a scattered light intensity as a function of time. The rate of fluctuations of the scattered light is directly related to the diffusion coefficient (D) of the NPs in suspension. Considering a constant temperature and a known dispersant viscosity, it is possible to determine the NPs size by the hydrodynamic radius (R_h), applying the Stokes-Einstein equation, as follows [120].

$$R_h = \frac{kT}{6\pi\eta D_\tau} , \quad (2)$$

Where, T is the absolute temperature; η is the solvent viscosity of the medium, k is the Boltzmann Constant; D_τ is the diffusion coefficient.

The assumption considered for the NP format was a hypothetical sphere. Therefore, the NP hydrodynamic radius was measured by the equipment considering this assumption, plus the NP solvation shell. Therefore, the output value displayed is slightly higher than the actual NP radius [121]. Another parameter measured by DLS is the polydispersity index (PDI). PDI is an indicator of the heterogeneity of the NPs. For a monodisperse sample is expectable that the PDI stays lower than 0.1 [121].

DLS was used to determine the average diameter and size distribution of the prepared NPs. The analysis was performed using the dielectric constant of water as dispersant, a standard cuvette (Sarstedt®) made of polystyrene and a sample dilution of (1:10) in ultra-pure water, to a final NPs concentration of 1 mg/mL. Three independent measurements were performed with a ZetaSizer Nano ZS, Malvern Instruments, UK.

3.5.2 Laser Doppler Velocimetry

DLS coupled with laser Doppler velocimetry was used to determine the zeta potential (ZP) of the prepared NPs. Zeta potential is a crucial physicochemical parameter and it is an indicator of the colloidal stability of NPs, since it controls the electrostatic interactions between the NPs. In a colloidal suspension, ions form a layer around the NPs known, as the Stern layer as shown in figure 10. An outsider layer, where ions diffuse more freely, is named the diffuse layer, which covers the Stern layer. This second layer is interpreted as the hypothetical boundary of the particle. Zeta potential is the electric potential that exists in this boundary. In figure 10 is represented the layers involved in a zeta potential measurement.

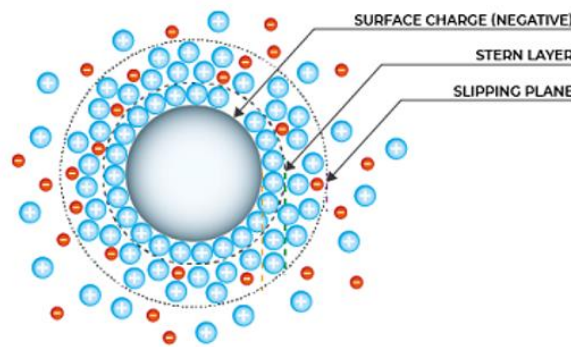


Figure 10 – Illustration of the different layers involved in zeta potential measurement.

NPs with higher zeta potential absolute values repel each other avoiding aggregation [120].

In the process of determining the zeta potential, an electric field must be applied to the NPs, inducing an electrophoretic effect. Radiation hits the particles, and the scattered light is detected by a photodetector enabling the determination of the electrophoretic mobility, μ_e . This parameter can be obtained by knowing the particle velocity (v , $\mu\text{m/s}$) and the induced electrical field (E , volts/cm), as can be seen from the following equation 3:

$$\mu_e = \frac{v}{E}, \quad (3)$$

Once calculated the electrophoresis mobility, the zeta potential can be determined by the *Helmholtz-Smoluchowski* equation 4:

$$\mu_e = \frac{\varepsilon\zeta}{4\pi\eta}, \quad (4)$$

Where ζ is the zeta potential; ε is the dielectric constant of vacuum; and η is the viscosity coefficient of the dispersant. The zeta potential values were obtained by the Smoluchowski model using the dielectric constant of water as dispersant, a DTS1070 cell and a sample dilution of (1:10) in ultra-pure water, to a final NPs concentration of 1 mg/mL. Three independent measurements were performed with a ZetaSizer Nano ZS, Malvern Instruments, UK.

3.6 Determination of the Encapsulation Efficiency and Loading Capacity

The encapsulation efficiency (EE) and loading capacity (LC) of the prepared NPs was determined indirectly, by quantifying the non-encapsulated drug in the supernatant. After the production of the TMZ+BTZ-loaded PLGA NPs, the supernatant containing free drug was separated from the PLGA NPs by sequential centrifugation steps as described in section 3.2.

While BTZ was quantified by UV-Vis absorbance measurements, TMZ was quantified by fluorescence spectroscopy. The measure of fluorescence of a sample is based on its excitation and emission of light (fluorescence) at different wavelengths. A beam of light hits the sample and promotes an excitation of the molecules, to an electronically excited state. As electrons return to their ground states, they emit lower energy radiation, with a higher wavelength. This emitted radiation is detected, and a value for the sample fluorescence is displayed. Fluorescent objects can only be excited and emit light in specific wavelengths, therefore they exhibit their own “fluorescent signature”. Free TMZ was quantified by fluorescence quantification using a microplate reader (Synergy 2 Microplate Reader, BioTek, UK) at excitation/emission wavelengths of 420/540 nm, respectively. The obtained fluorescence values were correlated to a TMZ calibration curve in PVA (figure A1 in appendix A).

UV-Vis spectrophotometry is a non-invasive quantitative measurement of the absorbed light as a function of the wavelength. A beam of light is directed through a path until reaching the sample. As the radiation is passing throughout the sample, part of the radiation is absorbed, and part is transmitted. The transmitted radiation reaches a detector. To determine the absorbance, a mathematical equation must be applied, as follows [122]:

$$A = -\log \left(\frac{I}{I_0} \right) , \quad (5)$$

Where, A is the absorbance; I is the light that reached the detector; I_0 is the incident light beam.

The free BTZ was quantified by UV-Vis absorbance measurements (Synergy 2 Microplate Reader, BioTek, UK) at λ_{\max} 269 nm and correlated to BTZ calibration curve in PVA (figure A2 in appendix A).

The EE and LC values for BTZ and TMZ were then determined using the following equations:

$$EE (\%) = \frac{\text{total amount of drug} - \text{amount of free drug}}{\text{total amount of drug}} \times 100 , \quad (6)$$

$$LC (\%) = \frac{\text{total amount of drug} - \text{amount of free drug}}{\text{total amount of PLGA}} \times 100 , \quad (7)$$

3.7 Determination of Tf Conjugation Efficiency

The Tf conjugation efficiency (CE) was determined by the BCA Protein Assay Kit (Pierce, Bonn, Germany). In this method, a well-known reduction reaction is used to quantify proteins in samples [123]. The reduction of Cu^{2+} to Cu^+ , by protein interaction in an alkaline medium, represents a highly sensitive and colorimetric detection of the Cu^+ using a specific reagent of bicinchoinic acid. The purple-colored product reaction is formed by the chelation of 2 molecules of BCA with one Cu^+ ion. The formed BCA/copper complex exhibits a powerful absorbance at 562 nm enabling protein quantification [124]. The UV-Vis spectrophotometry quantification technique is based on the mathematical law represented in equation 5 (subchapter 3.6).

Then, to determine the Tf CE, the non-conjugated Tf on the supernatant was quantified. To recover the NPs and separate the non-conjugated Tf several centrifugation steps were performed, as already described in section 3.4. Then, 25 μL of the supernatant (sample) was added to 200 μL of working reagent (WR) at a ratio of 1:20 (v/v) and incubated for 30 minutes at 37 °C. The WR enables the purple-colored reaction and it is composed of 50 parts of bicinchoinic acid and 1 part of copper(II) sulfate pentahydrate. The free Tf was quantified by UV-Vis absorbance measurements (Synergy 2 Microplate Reader, BioTek, UK) at λ_{max} 562 nm and correlated to a calibration curve (figure A1.3 in appendix A1).

The percentage of CE was determined through the following equation:

$$CE (\%) = \frac{\text{Total amount of Tf-Free amount of Tf}}{\text{Total amount of Tf}} \times 100, \quad (8)$$

3.8 Fourier-Transformed Infrared Spectroscopy

Fourier-Transformed Infrared Spectroscopy (FTIR) was used to confirm the Tf conjugation onto the TMZ+BTZ-loaded PLGA NPs. FTIR is one of the most used characterization techniques due to its highly sensitive analysis of surface chemistry to determine functional groups, through their molecular bonds [125]. The fact that this characterization technique presents a non-destructive nature and simple sample preparation and acquisition, made this method one of the most used for NPs surface characterization.

FTIR characterization relies on the ability that several molecules have to absorb light in the infrared (IR) range of the electromagnetic spectrum, and convert it to a molecular vibration, called frequency of vibration or resonance frequency, allowing a quantitative and qualitative analysis [125]. When the IR radiation beam passes through the sample, the covalent bond of the sample

absorbs this energy at specific wavelengths, converting into vibrational energy. As different samples have their specific chemical bonds, producing different vibration intensities, this results in a finger-print spectrum of all the components of the sample. The resulting spectrum is given by absorbance/transmittance vs 1/wavelength, represented also as wavenumber (cm^{-1}) [126].

The FTIR spectra of the prepared NPs was recorded using a Bruker Alpha-P FT-IR Spectrometer (Bruker Optics Inc., Billerica, MA, USA) and Opus Software for data acquisition. In this method, the sample containing the NPs is placed directly into the ATR crystal, promoting a non-destructively and reproducible analysis [127]. The spectra were recorded in absorbance mode, within a wavelength range of $4000\text{-}375\text{ cm}^{-1}$ and 64 scans at 4 cm^{-1} of resolution for all measurements, sample and background. The intensity range of the obtained spectra were normalized. To perform the analysis, a $10\text{ }\mu\text{L}$ drop of each sample was placed on the crystal and dried using a nitrogen flow. The FTIR measurements were performed for Tf stock solution, PLGA NPs, Tf-PLGA NPs, Tf-TMZ+BTZ PLGA NPs and non-conjugated TMZ+BTZ-PLGA NPs.

3.9 Transmission Electron Microscopy

Transmission electron microscopy (TEM) is a widely used high-resolution imaging technique to perform the morphological characterization of samples at the nanoscale [128]. For the TEM analysis, the prepared NPs were placed on copper grids (Formvar/Carbon – 400 mesh Copper, Agar Scientific, UK) and negatively stained with 2% (v/v) uranyl acetate. Uranyl is considered a golden standard heavy metal salt for TEM analysis due to its high contrast, low cost, and intrinsic affinity for biological samples, allowing a facilitated visualization and analysis of the sample structures [129].

For the samples' preparation, $5\text{ }\mu\text{L}$ of the NPs' suspension were soaked in the copper grid for 5 minutes and stained with uranyl acetate for 45 seconds. Then, the samples were air-dried before visualization. The NPs were visualized at an accelerating voltage of 80 kV using a Jeol JEM 1400 electron microscope (Japan).

3.10 *In vitro* Release of TMZ and BTZ from PLGA NPs

In vitro studies to evaluate the release of TMZ and BTZ from the non-modified and Tf-modified NPs were performed in simulated physiological conditions over 15 days. For this, the NPs were suspended in PBS (0.01 M, pH 7.4) at $37\text{ }^{\circ}\text{C}$ and divided in 10 aliquots. PBS allows the simulation of the human body pH, ions concentrations and osmolarity [130].

At each predetermined timepoint, the NPs' aliquot samples were centrifuged to separate the NPs from the supernatant containing the released drugs. The amount of drug released was determined by UV-Vis absorbance ((UV- 1700 PharmaSpec UV-Vis spectrophotometer, Shimadzu, Japan), and correlated with control samples for each drug

The TMZ and BTZ release curves, representing the percentage of compound released in the function of time, were then plotted by the following equation:

$$\% Drug_{release} = \frac{\text{amount of drug released at time } t}{\text{amount of encapsulated drug}} \times 100, \quad (9)$$

3.11 Determination of NPs Stability

The stability of the non-modified and Tf-modified TMZ+BTZ loaded PLGA NPs in different conditions was studied by DLS measurements, in terms of variations of the hydrodynamic size (nm), PDI and zeta potential (mV).

To evaluate the colloidal stability at storage conditions, the prepared NPs were stored at 4°C for weekly DLS measurements. These measurements were performed for 10 weeks.

To simulate the stability in physiological conditions, the prepared NPs were suspended in PBS (0.01 M, pH 7.4) and stored at 37 °C. These measurements were performed for 4 weeks.

3.12 Cell Culture

Two humans GBM cell lines with different MGMT expression were used to analyze the cytotoxicity of the produced NPs. U251 cells were selected due their high sensitivity to TMZ's effect and low MGMT expression [131] and T98G were chosen due to being TMZ-resistant due to high MGMT endogenous levels [132].

Both cell lines were cultured in DMEM supplemented with 10% FBS, 1% penicillin-streptomycin and 1% fungizone to prevent cell culture contaminations. The cells were trypsinized and passaged at a confluence of approximately 80%. During all the experimental work, the cultures were maintained at 37 °C in a 5% CO₂ incubator.

3.13 *In vitro* Cytotoxicity Studies

The antiproliferative effect of free TMZ, free BTZ, free TMZ+BTZ combination and the Tf-TMZ+BTZ NPs was evaluated using the U251, and T98G cell lines by a sulforhodamine B (SRB) colorimetric assay. The SRB assay is used for cell density determination according to the measurement of cellular protein content, directly related with cell survival and cellular proliferation [133].

The cells were cultured at a density of 1,000 cells/well using 96-well plates and incubated for 24 hours at 37 °C in a humidified 5% CO₂ incubator for cell adhesion. Then, free drugs, free drugs combination, and Tf-TMZ+BTZ NPs were diluted in DMEM medium and added to the cells. The following concentrations were used: for free TMZ 0.01-2000 μM; and 1 x 10⁻⁴ – 1 x 10⁴ nM for free BTZ, TMZ+BTZ and Tf-TMZ+BTZ NPs. Untreated cells were used as negative control. After 72 hours of incubation, the SBR protocol was performed. First, the cells were fixed with trichloroacetic acid (TCA) 10% (w/v) at 4 °C for 1 hour, then washed and dried at room temperature. Then, 50 μL of SRB was added to each well and left for 20 minutes to allow cell staining. To remove SRB excess, the samples were washed twice with acetic acid 1% (v/v) and stove-dried. The protein-bound stained was solubilized by adding 100 μL of Tris buffer solution. The quantification of protein was measured using UV-Vis absorbance (BioTek Synergy HT Microplate Reader – BioTek, UK) at 560 and 655 nm.

Cell growth was determined by the following equation:

$$\text{Cell growth (\%)} = \frac{T}{C} \times 100, \quad (10)$$

Where, T is the absorbance values at the end of the incubation period in the treated wells, C the absorbance values in the untreated cells wells (control).

The dose-response curves were made using GraphPad 9.3.1 software (GraphPad Software Inc., USA)

3.14 Statistical Analysis

All the results are presented as mean ± standard deviation (SD) for three independent formulations. T-student test was applied for the statistical analysis, with a 95% confidence interval, with p<0.05 being considered significant for a toxicity screening.

Chapter 4

Results and Discussion

In this chapter, the results obtained by the optimized protocol of NPs preparation, transferrin functionalization and release profile of TMZ and BTZ were studied and discussed. Additionally, the stability and antiproliferative activity of the NPs were also discussed.

4.1 Experimental Design and Protocol Optimization

DoE was used to optimize the protocol for the TMZ-BTZ loaded PLGA NPs preparation. According to preliminary experiments, four experimental variables were identified as representing a direct effect on the NPs physicochemical characteristics. The chosen independent variables were the PLGA mass (X_1), the percentage (%) of PVA (X_2), the number of sonication cycles (X_3) and the ratio between the organic phase/aqueous solution (o/w) ratio (X_4). All the remaining parameters of the preparation protocol, such as sonication amplitude, time of sonication, evaporation process and emulsification process were maintained constant. The response/dependent variables analyzed were the NP size (Y_1), PDI (Y_2), zeta potential (Y_3), TMZ EE (Y_4) and BTZ EE (Y_5) (subchapter 3.3 – table 3).

As mentioned in subchapter 3.3, an FFD (2^4) was initially implemented with a 2-level variation (-1 and +1). For this, 19 formulations were prepared, with 16 experimental runs and 3 replicas of the centre points set halfway between the low and high levels to check for curvature in the model. However, ANOVA statistical analysis revealed that the model was not significant for all the studied response variables ($p > 0.05$) and was therefore augmented to a CCD design. 8 additional runs varying in two extra levels ($-\alpha$ and $+\alpha$) (table 4) were added, completing a total of 27 formulations. The statistical analysis was performed by ANOVA, and the results are presented in table 5 and tables A1-A5 in appendix 2. This CCD proved to only be significant for variables size (Y_1) and PDI (Y_2) ($p < 0.05$), with size (Y_1) being adjusted by a quartic regression model and PDI (Y_2) by linear regression.

Table 5 – Results of the statistical analysis using ANOVA for the significant response variables Y_1 e Y_2 .

Parameter	Size - Y_1				
	SS	dF	MS	F-Value	p-value
Model	5.569×10^5	24	23205.54	1430.38	0.0007
Residual					
Lack of Fit					
Pure Error	32.45	2	16.22		
Cor Total	5.570×10^5	26			
R²			0.9999		
Parameter	PDI – Y_2				
	SS	dF	MS	F-Value	p-value
Model	0.0488	4	0.0122	2.90	0.0454
Residual	0.0926	22	0.0042		
Lack of Fit	0.0915	20	0.0046	8.60	0.1092
Pure Error	0.0011	2	0.0005		
Cor Total	0.1414	26			
R²			0.3454		

Abbreviations: sum of squares (SS); mean square (MS).

Table 5 shows that the regression model has a good fit for response prediction regarding size (Y_1) and the PDI (Y_2), and the remaining response variables zeta potential (Y_3) TMZ EE (Y_4) BTZ EE (Y_5) were not considered for the model.

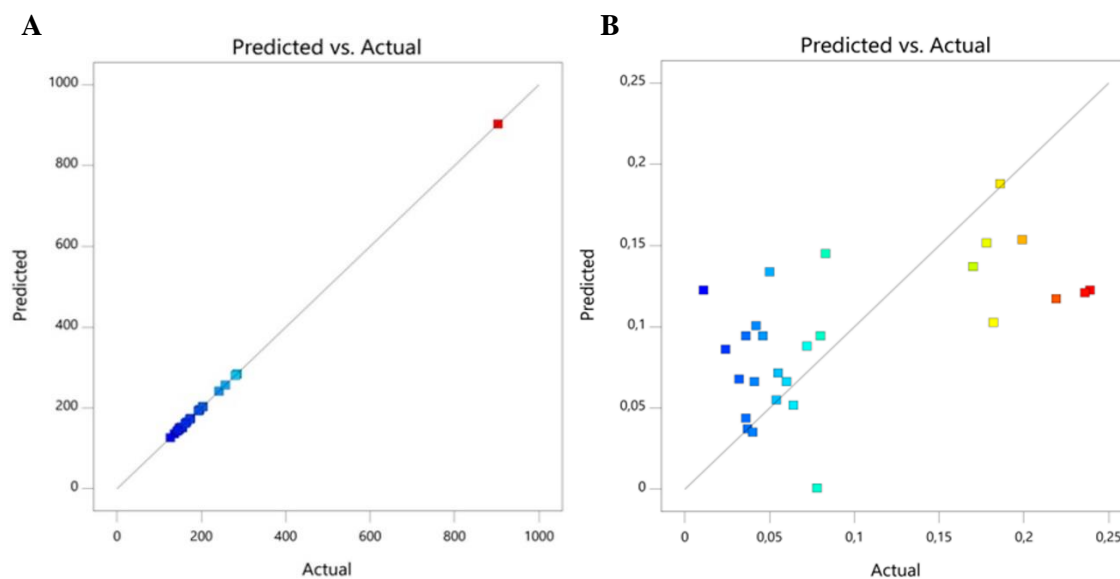


Figure 11 – Graphical plots between the experimental values obtained vs the predicted values for the significant variables, (A) Size (Y_1) and (B) PDI (Y_2). The blue squares represent lower values, in contrast to red squares that represent higher values.

The graphic representation of the experimental observations and predicted values for the NPs' size (figure 11.A) shows a good agreement between the predicted and the experimental values obtained as expected due to the high R^2 values obtained for the model (0.9999), as shown in table 5. In contrast, the experimental values obtained for the PDI appear to be slightly scattered from the expected values. This is in agreement with the low R^2 value (0.3454), however, the linear regression model proved to be significant as mentioned previously ($p < 0.05$).

For both response variables considered for the model (size (Y_1), and PDI (Y_2)), the regression coefficients (RC) were determined, describing and estimating the impact between the experimental variables and the responses. The values of RC and p-values for each experimental variable are described in table 6. The positive sign before the coefficient indicates a positive effect with increased response, while a negative sign indicates a decreased response. The RC were used to obtain the regression equation for each response, where only the significant variables ($p < 0.05$) were considered, excluding the non-significant experimental variables ($p > 0.05$). The obtained equations (A2.1 and A2.2 are presented in Appendix 2). Table 6 summarizes the determined RC values for Y_1 and Y_2 , as well as the p-values for each experimental variable.

Table 6 – Regression coefficients (RC) and p-values for the significant variables Y_1 and Y_2 .

	Size – Y_1		PDI – Y_2	
	RC	p-Value	RC	p-Value
X_1-PLGA Mass	4.78	0.1217	0.0327	0.0312
X_2-%PVA	-244.10	< 0.0001	-0.0172	0.2395
X_3-Sonication Cycles	-6.17	0.0786	-0.0182	0.2142
X_4-Ratio O/W	5.50	0.0963	0.0255	0.0870
X_1X_2	8.08	0.0152		
X_1X_3	7.68	0.0168		
X_1X_4	9.07	0.0121		
$X_2 X_3$	5.07	0.0373		
$X_2 X_4$	-5.24	0.0350		
$X_3 X_4$	5.03	0.0378		

The contour plots and response surface analysis were obtained according to the determined polynomial function in 2- and 3-dimensional graphics, respectively. These allow studying the impact and interaction between each independent variable and the dependent variables. Furthermore, the impact of the significant independent variables on each dependent variable were studied and discussed below.

4.1.1 Effect on the NPs' Size

The NPs size is an essential physicochemical property since it directly influences the NP half-life, pharmacokinetics, biodistribution, and cellular uptake, which is related to their ability to cross the biological barriers [134]. For the NPs to be able to cross the BBB, their size must not exceed 200 nm, as already mentioned. In addition, NPs below 200 nm represent enhanced ability to accumulate in the brain tumor tissue, due to the vascular fenestration of this microenvironment (40-200 nm) [135]. The NPs prepared in the CCD exhibited sizes ranging from 126.7 nm (formulation 8) to 903.1 (formulation 22) as shown in table 4. In figure 12 and 13 are represented the 2D-contour and 3D- response surface plots that provided a visual representation of the effect of the different independent variables on the NP size.

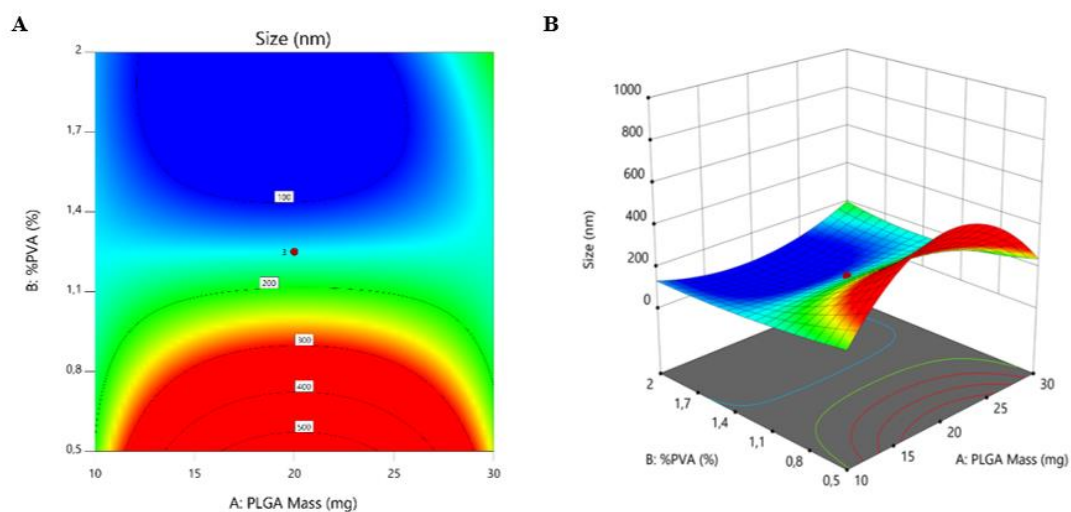


Figure 12 – (A) Contour and (B) response surface plots showing the effect of independent variables, PLGA mass and the %PVA, on the NP size.

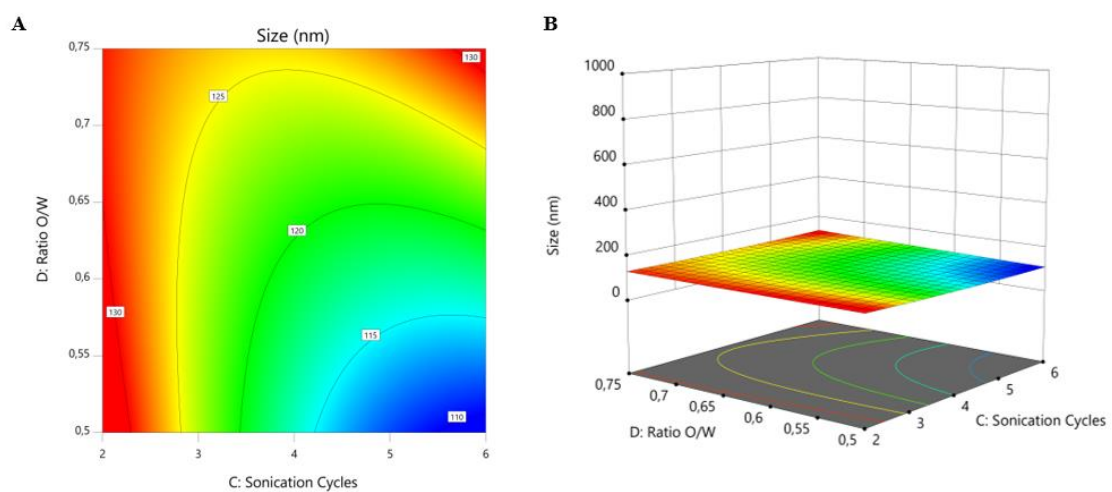


Figure 13 – (A) Contour and (B) response surface plots showing the effect of the independent variables, sonication cycles and the O/W ratio, on the NPs' size.

Analyzing the RC values (table 2.1 in appendix A2) and the obtained regression equation (eq. 1, appendix A2), it is concluded that the PLGA mass (X_1) and the O/W ratio (X_4) have a positive effect on the NP size. The amount of PLGA leads to the formation of larger NPs, since an increased polymer concentration leads to an increased viscosity of the organic phase. This hampers the diffusion of the organic solvent into the aqueous phase, leading to the formation of larger oil droplets during the emulsification process [98]. The O/W ratio also positively affected the NP size due to the increase in the organic phase viscosity. On the other hand, %PVA (X_2) and the number of sonication cycles (X_3) negatively affected the NP size, therefore increasing these variables, resulted in formation of smaller NPs. PVA promotes the steric stabilization of the emulsion, decreasing the interfacial tension between the oiled droplets containing the PLGA and the continuous aqueous phase [136]. In addition, the sonication cycles are crucial to promoting the disruption of the emulsion formed droplets into smaller ones [137].

4.1.2 Effect on the NPs' PDI

PDI is also an important physicochemical property of the NPs, since it is an indicator of the size heterogeneity of a NPs suspension. According to the literature, for a monodisperse NPs' sample, the PDI is expected to be below 0.1 [138]. The PDI of the NPs prepared in the CCD ranged from 0.011 (formulation 24) to 0.239 (formulation 19) as shown in table 4. In figure 14 is presented the 2D contour plot (14.A) and the 3D response surface plot showing the effect of the PVA and sonication cycles on the NPs' PDI values.

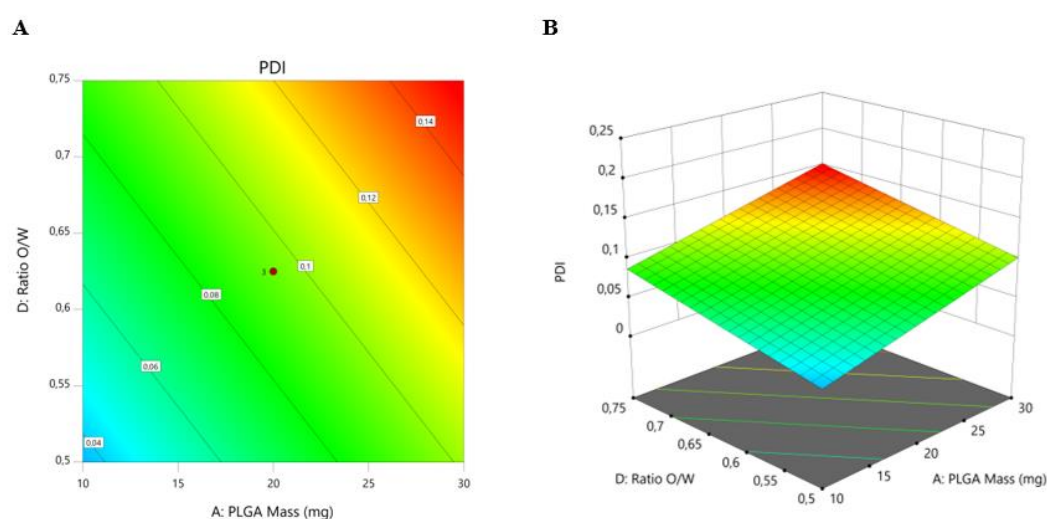


Figure 14 – (A) Contour and (B) response surface plots showing the effect of independent variables, PLGA mass and the O/W ratio, on the NPs' PDI.

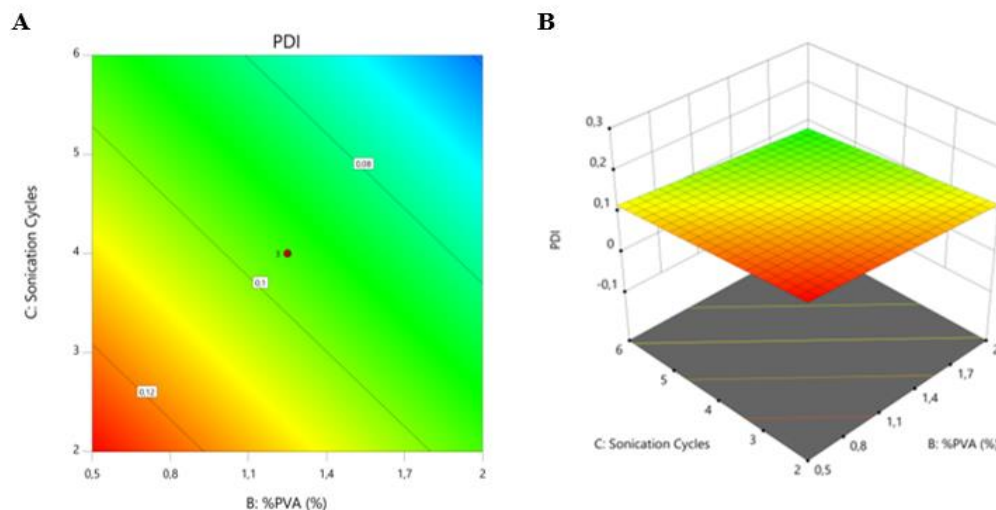


Figure 15 – (A) Contour and (B) response surface plots showing the effect of independent variables, the %PVA and sonication cycles, on the NPs' PDI.

According to the RC values (table A2.2 in appendix A2) and the regression equation (Appendix A2, equation 2), the PVA amount and number of sonication cycles negatively affect the response variable. On the other hand, the PLGA mass and the O/W ratio exhibited a positive impact on the NPs' PDI. In other words, as the %PVA and/or the number of sonication cycles increase, the PDI decreases. The PDI gives an indication of the different NP sizes in a sample, thus the smaller the variations between the NPs sizes, the lower the PDI value and, therefore, a monodisperse sample can be considered. These PDI related conclusions are similar to the previous ones drawn for the NPs' size. The higher the %PVA and the number of sonication cycles, the more stable the formation of the NPs emulsion droplets and the higher disruption of these droplets into smaller droplets, resulting in a monodisperse emulsion with a reduced PDI value. An increasing in the amount of PLGA and O/W ratio translates into an increased viscosity in the organic phase, leading to a more unstable emulsion and higher dispersion of the NP size. The graphs presented in figure 14 and 15 allow to corroborate the conclusions drawn and graphically visualize.

4.2 Protocol Optimization and Model Validation

The optimization process was performed after determining the regression equations (Appendix A2, equations 1-2), that allowed the choice of the optimal experimental values by establishing the range limits for each response. For the NPs size the range was set between 150-180 nm (Y_1); and for the PDI, the range was set at 0.011-0.1 (Y_2). In table 7 is represented the optimal levels of the independent variables.

Table 7 – Optimal formulation values for TMZ+BTZ loaded PLGA NPs determined by experimental design.

Parameter	Independent variable	Units	Optimal Value
X₁	PLGA mass	mg	19
X₂	PVA	%	1.26
X₃	Sonication Cycles	#	4
X₄	O/W Ratio	mL	0.667

To validate the protocol, a formulation checkpoint was prepared in triplicate applying the chosen optimal experimental values. In table 8 are presented the predicted responses and the obtained experimental results.

Table 8 – Validation model; Comparison between the predicted and the experimental values. The experimental results are represented as mean \pm SD (n=3).

	Predicted Values	Experimental Values
Size (nm)	149 (135-163)	159 \pm 6 (152-164)
PDI	0.099 (0.017-0.182)	0.055 \pm 0.007 (0.048-0.062)
Zeta Potential (mV)	-19.6 (-26.8-[-12.4])	-20.5 \pm 1.5 (-19.1-[-22.0])
TMZ EE (%)	75.3 (6.1-144.4)	65.4 \pm 15.8 (50.2-86.5)
BTZ EE (%)	72.3 (41.2-103.4)	71.1 \pm 12.2 (58.0-87.2)

Analyzing table 8, it is verified that all the responses of the checkpoint formulations were within the predicted range. As expected, the predicted range of the variables ($Y_{3,4,5}$) is wider than the variables ($Y_{1,2}$), since the model was not significant for the $Y_{3,4,5}$ variables. In addition, the physicochemical properties of the NPs (size, PDI and zeta potential values) proved to be suitable for brain delivery, with sizes below 200 nm and PDI values below 0.1, suggesting the presence of a monodisperse colloidal suspension. Furthermore, the high absolute zeta potential values, due to the negatively charged carboxyl groups of PLGA, suggest that the NPs are stable, avoid aggregation [135]. The values obtained for the encapsulation efficiencies were high suggesting good drugs entrapment within the NPs.

4.3 Transferrin-TMZ+BTZ Loaded PLGA NPs

The TMZ+BTZ loaded PLGA NPs were conjugated with Tf for an active targeting drug delivery approach. The conjugation efficiency (CE) was evaluated using the BCA kit to quantify the unbound Tf. Unloaded PLGA NPs were used as a negative control to assess if the drug molecules adsorbed to the NPs' surface could affect the functionalization protocol. The CE of Tf of the PLGA NPs varied from $92 \pm 4\%$ for the unloaded PLGA NPs (control) to $70 \pm 9\%$ for the TMZ+BTZ loaded PLGA NPs. This significant CE decrease ($p < 0.05$) suggests that the amount of drug adsorbed into the NPs surface affects the conjugation of the Tf amine groups to the terminal carboxylic groups of PLGA. However, the final CE for the TMZ+BTZ loaded NPs ($70 \pm 9\%$) still yielded NPs with the appropriate Tf molecules-to-NPs ratio, that was 121 ± 10 molecules of Tf per NP. The number of Tf molecules per NP for this application was determined based in work previously published by the group [139].

The NPs were physicochemically characterized and table 9 presents a comparison between the non-modified and Tf-modified NPs.

Table 9 – Experimental data obtained for the Tf-TMZ+BTZ loaded PLGA NPs. The data is represented as mean \pm SD (n=3).

TMZ +BTZ loaded PLGA NPs		
	Non-modified NPs	Tf-modified NPs
Size (nm)	159 ± 6	156 ± 3
PDI	0.055 ± 0.007	0.042 ± 0.016
Zeta Potential (mV)	-20.5 ± 1.5	-21.5 ± 1.6
EE TMZ (%)	65.4 ± 15.8	69.6 ± 12.0
EE BTZ (%)	71.1 ± 12.2	46.0 ± 12.8
TMZ LC (%)	1.4 ± 0.1	1.8 ± 0.3
BTZ LC (%)	1.9 ± 0.3	1.2 ± 0.3

Analyzing table 9, it is possible to conclude that the physicochemical properties of the NPs (size, PDI and zeta potential) did not undergo significant changes ($p > 0.05$) with Tf conjugation.

However, it is possible to verify that, statistically, BTZ EE and LC significantly decreased with the Tf conjugation protocol. The BTZ EE decreased from $71.1 \pm 12.1\%$ to $46.0 \pm 12.8\%$ ($p < 0.05$), suggesting that approximately 25% of drug molecules are lost during Tf conjugation. This can be explained due the drug adsorbed on the NP surface that was eliminated to take place the Tf-PLGA chemical bonds. Plus, the additional centrifugation steps were added with the Tf protocol functionalization. However, the obtained BTZ EE results still remain within favorable

values. The EE and LC values for TMZ did not suffer significant changes with the surface modification ($p>0.05$). The obtained results also revealed that for Tf-modified NPs, both EE and LC values for BTZ are statistically significantly lower than the ones for TMZ ($p<0.05$). Since the difference between the solubility of TMZ and BTZ in water is not considerable, the differences in LC may be due to the centrifugation steps involved throughout the NP preparation process.

TEM analysis was used to confirm the shape and dimensions of the produced NPs. Below, in figure 16 is possible to observe the prepared Tf-BTZ+TMZ NPs and confirm that these results are in concordance with the results obtained by the NP's size using DLS. It also allowed to conclude that the preparation method yielded well-stabilized monodisperse PLGA NPs. In addition, it is possible to observe the spherical shape of the NPs and the homogeneous size distribution in agreement with the low PDI.

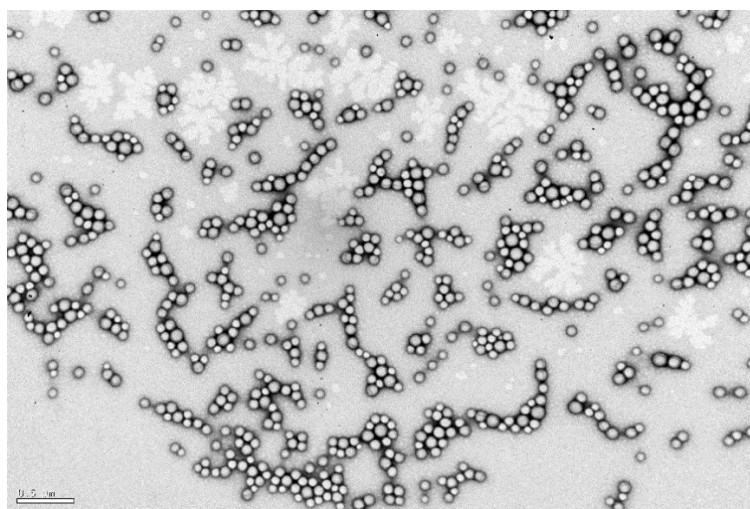


Figure 16 – TEM image of the prepared Tf- BTZ+TMZ PLGA NPs. Scale bar 500 nm.

4.4 PLGA NPs and Transferrin Conjugation

FTIR analysis was used to confirm the success of the preparation of the PLGA NPs (as control), TMZ+BTZ loaded PLGA NPs and the effectiveness of Tf conjugation. The spectra were recorded in absorbance mode vs wavelength in a range of 350 to 4000 cm^{-1} . These FTIR spectra are called as fingerprint spectra since they represent unique chemical bound for each molecule. According to literature, in between the 1500-2500 cm^{-1} region is possible to detect the double-bonds, such as, C=C, C=H and C=O. Detection region of 2500 to 2000 cm^{-1} for the triple-bonds (C≡C and C≡N). Lastly, single-bonds are possible to detected in higher wavelength regions 2500 to 4000 cm^{-1} for O-H, C-H and N-H detection [140]. Below, in figure 17, is represented the FTIR spectrum of the PLGA NPs without any process of functionalization or conjugation and the Tf stock solution for the NPs conjugation.

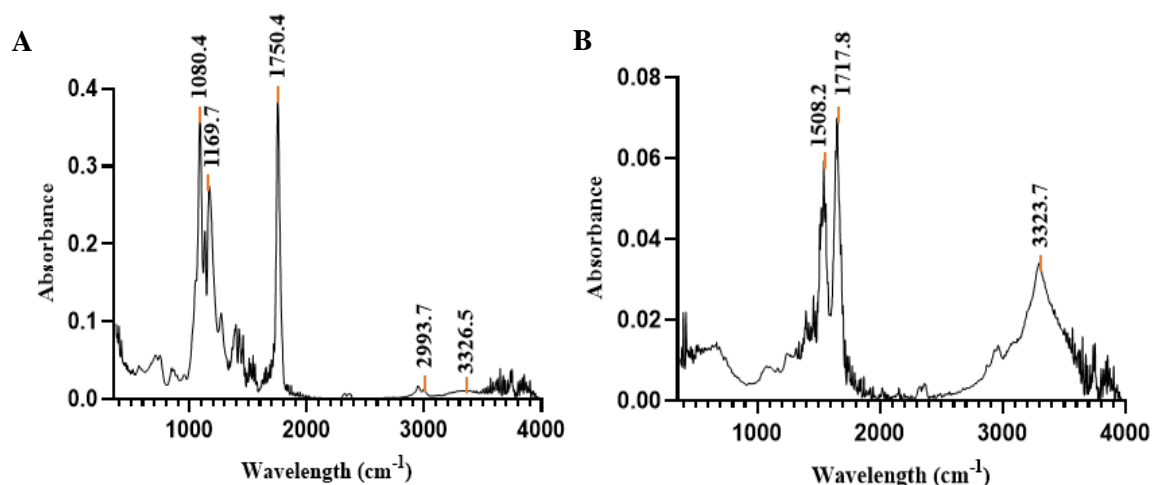


Figure 17 – FTIR absorbance spectrum of (A) PLGA NPs (control) (B) Tf stock solution for conjugation recorded from 350-4000 cm⁻¹.

The PLGA copolymer can be divided into 4 main regions. At the peak 2885-3010 cm⁻¹ corresponds to C-O stretches; around 1762.6 cm⁻¹ a second peak due the C=O stretch peak; in between 1450-850 cm⁻¹ the peak of C-H bends, and lastly at 1186-1089 cm⁻¹ is represented the peak of C-O stretch. For Tf absorbance spectrum, 3 regions stand out corresponding to the amine groups of Tf molecule. The first amine group is represented at approximately 1540 cm⁻¹; the second amine group is seen on peak 1650 cm⁻¹ and the last amine group of Tf is represented on peak 3300 cm⁻¹ [141]. Analyzing figure 17.B is possible to observe these peaks of the Tf. Thereby, the results are in agreement with the values found in the literature for both, PLGA NPs and Tf stock solutions.

To study if the process of Tf-conjugation was successful, the FTIR spectra of Tf-PLGA NPs was also recorded. To validate the Tf conjugation protocol is necessary to be analyzed in detail the sift of the main PLGA peaks in spectrums figures 17.A and 18. After conjugation, the 1080.4 cm⁻¹ shift to 1089.1 cm⁻¹, and 1750.4 cm⁻¹ to 1753.2 cm⁻¹ [141]. All these peak shifts suggests stronger physical interaction between the molecules. In addition, a shift from 3326.5 cm⁻¹ to 3343.5 cm⁻¹ with an increase in absorbance intensity representing the amine group of Tf molecule. All the obtained spectra were normalized and smoothed.

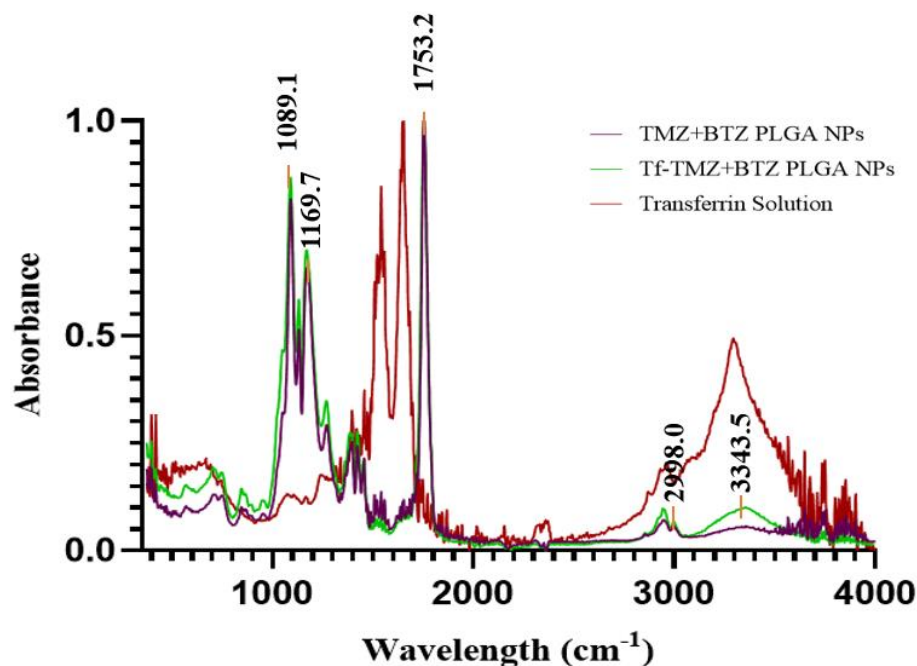
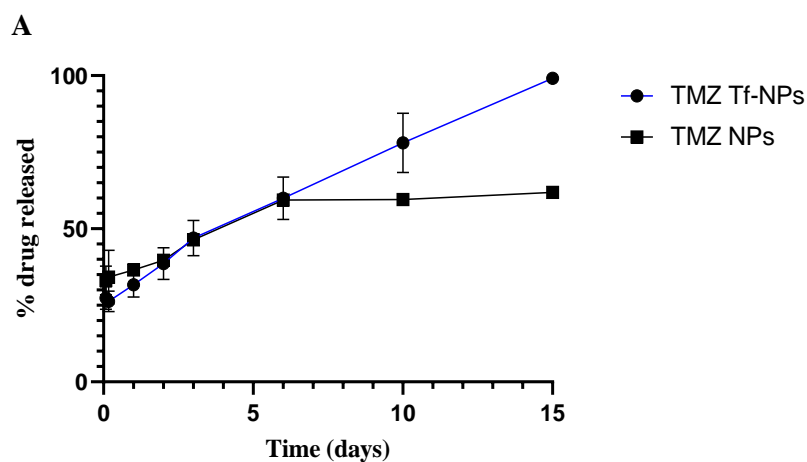


Figure 18 – FTIR absorbance spectrum of Tf-TMZ+BTZ PLGA NPs, TMZ+BTZ PLGA NPs and Tf stock solution recorded from 350-4000 cm⁻¹.

These observed conclusions and the data from literature enable to affirm the success of the conjugation and encapsulation protocols in the PLGA NPs.

4.5 TMZ+BTZ Release Profile

A major characteristic of DDSs is the ability of nanocarriers to sustainable release the encapsulated drugs. Therefore, the prepared Tf conjugated and non-conjugated PLGA NPs were evaluated for their ability to maintain a sustained release of TMZ and BTZ. The *in vitro* release profile of BTZ and TMZ from the PLGA NPs was evaluated mimicking the physiological temperature, pH and salt concentrations (37 °C in PBS, pH 7.4, 0.01M). The obtained release profiles are represented in figure 19.



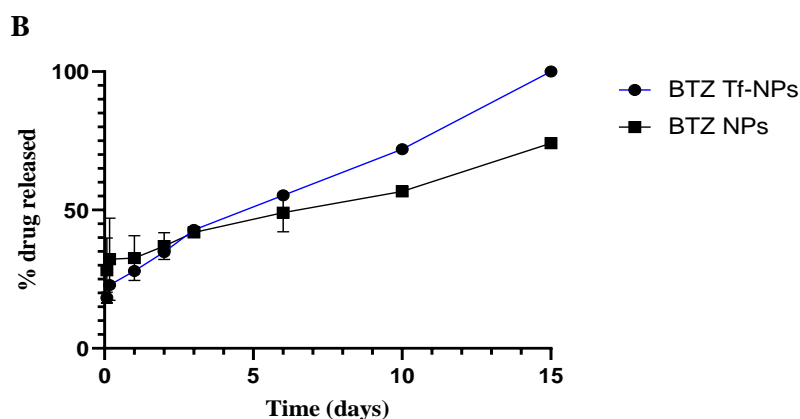


Figure 19 – *In vitro* release profile of (A) TMZ and (B) BTZ from Tf-conjugated and non-conjugated PLGA NPs in PBS (pH 7.4, 0.01M) at 37 °C. The results are represented as mean \pm SD (n=2).

Comparing the release profiles, in non-conjugated NPs the drug molecules were released in a biphasic pattern, with an initial burst release followed by a more controlled and slower drug release. As figure 19 A shows for the TMZ release from non-conjugated NPs, $37 \pm 18\%$ of the total TMZ was released in the initial 24 hours. In figure 19 B, we can observe that in the initial 24 hours, $33 \pm 8\%$ of the total BTZ was released from the NP. This initial burst release is characteristic of PLGA NPs explained by the portion of drugs that is adsorbed into the NPs' surface instead of encapsulated. The controlled and slower second phase occurs over time by a combination of 3 pathways, the drugs diffusion from the PLGA NPs matrix, the NP erosion and hydrolysis [142]. The PLGA suffers hydrolysis of the ester bonds into its monomers PLA and PGA, promoting the accumulation of acidic degradation products within the PLGA NP. This mechanism leads to pores formation and increased NP erosion rate [143].

In contrast, analyzing the release profile of the Tf-conjugated NPs is possible to conclude that the profile is affected by Tf conjugation. As already concluded in section 4.3, after Tf conjugation the EE decreases significantly ($p < 0.05$) due to the elimination of some of surface-adsorbed drug for establishment of the Tf chemical bonds with PLGA, slowing the initial biphasic burst release. In Tf-modified NPs, after 24 hours the release of BTZ and TMZ is only $28 \pm 1\%$ and $32 \pm 4\%$, respectively. After 15 days Tf-conjugated NPs exhibit a total release of $100 \pm 0\%$ for BTZ and $99.2 \pm 1.2\%$ for TMZ, respectively. These results can be supported by some Tf linked to the NPs surface that possible obstruct water permeation, masking the diffusion of drug molecules [144]. These release profiles allow to conclude that the developed PLGA NPs are a suitable approach for the brain delivery while releasing the TMZ and BTZ, due to its biphasic and controlled patterns.

4.6 Stability of PLGA NPs in Storage Conditions

The NPs' properties (mean size, PDI and zeta potential values) were weekly measured to evaluate the NPs colloidal stability over time. The TMZ+BTZ loaded PLGA NPs and Tf-TMZ+BTZ loaded PLGA NPs were analysed over 10 weeks. The results are summarized in table 10.

Table 10 – Mean size, PDI and zeta potential values for both Tf conjugated (n=2) and non-conjugated (n=3) TMZ+BTZ loaded PLGA NPs in storage conditions. Data is represented as mean \pm SD.

	Hydrodynamic Size (nm)	PDI	Zeta Potential (mV)
TMZ+BTZ loaded PLGA NPs			
Day 0	159 \pm 6	0.055 \pm 0.007	-20.5 \pm 1.5
Day 7	153 \pm 7	0.043 \pm 0.015	-19.2 \pm 1.3
Day 14	158 \pm 12	0.037 \pm 0.019	-20.3 \pm 1.9
Day 21	154 \pm 9	0.040 \pm 0.016	-21.1 \pm 2.1
Day 28	153 \pm 5	0.047 \pm 0.009	-21.6 \pm 1.9
Day 36	152 \pm 8	0.041 \pm 0.009	-22.2 \pm 2.4
Day 42	162 \pm 23	0.133 \pm 0.076	-20.3 \pm 1.3
Day 49	161 \pm 3	0.072 \pm 0.005	-18.5 \pm 1.4
Day 56	149 \pm 8	0.055 \pm 0.030	-20.5 \pm 1.9
Day 63	146 \pm 7	0.048 \pm 0.041	-16.8 \pm 1.0
Day 70	145 \pm 13	0.040 \pm 0.030	-18.4 \pm 1.6
Tf-TMZ+BTZ loaded PLGA NPs			
Day 0	153 \pm 2	0.029 \pm 0.001	-21.1 \pm 2.5
Day 7	169 \pm 28	0.119 \pm 0.115	-21.4 \pm 5.2
Day 14	155 \pm 3	0.093 \pm 0.020	-21.4 \pm 0.8
Day 21	171 \pm 26	0.140 \pm 0.113	-22.0 \pm 0.1
Day 28	151 \pm 0	0.059 \pm 0.003	-20.2 \pm 1.6
Day 36	198 \pm 63	0.124 \pm 0.083	-15.7 \pm 1.0

Day 42	150 ± 2	0.288 ± 0.371	-21.0 ± 0.4
Day 49	146 ± 1	0.056 ± 0.002	-17.6 ± 3.5
Day 56	149 ± 2	0.061 ± 0.015	-23.2 ± 1.7
Day 63	161 ± 17	0.100 ± 0.127	-18.3 ± 3.2
Day 70	145 ± 1	0.066 ± 0.011	-19.0 ± 1.6

Both non-modified and Tf-modified TMZ+BTZ loaded PLGA NPs proved to be stable at storage conditions for at least 10 weeks, since no statistically significant changes were observed in the studied physicochemical properties overtime ($p>0.05$).

4.7 Stability of PLGA NPs in Physiological Conditions

The NPs' properties (mean size, PDI and zeta potential values) were weekly measured to evaluate the NPs stability over time in simulated physiological conditions (PBS 0.01 M, pH 7.4). The TMZ+BTZ loaded NPs and the Tf-TMZ+BTZ loaded PLGA NPs were analysed over 4 weeks. The results are summarised in table 11.

Table 11– Mean size, PDI and zeta potential values for both Tf conjugated (n=2) and non-conjugated (n=3) TMZ+BTZ loaded PLGA NPs in storage conditions. Data is represented as mean ± SD.

	Hydrodynamic Size (nm)	PDI	Zeta Potential (mV)
TMZ+BTZ loaded PLGA NPs			
Day 0	159 ± 17	0.096 ± 0.028	-7.8 ± 1.3
Day 4	174 ± 14	0.089 ± 0.051	-8.3 ± 1.8
Day 8	142 ± 8	0.061 ± 0.023	-11.1 ± 2.1
Day 12	145 ± 6	0.080 ± 0.027	-9.7 ± 3.2
Day 16	144 ± 1	0.080 ± 0.050	-9.5 ± 2.1
Day 20	139 ± 2	0.073 ± 0.029	-12.3 ± 3.9
Day 24	141 ± 6	0.071 ± 0.014	-8.9 ± 0.8
Day 28	138 ± 7	0.048 ± 0.025	-11.5 ± 4.0

Day 32	161 ± 26	0.106 ± 0.015	-9.7 ± 3.3
Tf-TMZ+BTZ loaded PLGA NPs			
Day 0	144 ± 5	0.052 ± 0.001	-6.4 ± 0.2
Day 4	161 ± 1	0.133 ± 0.018	-8.7 ± 1.2
Day 8	142 ± 3	0.086 ± 0.031	-12.4 ± 4.0
Day 12	145 ± 6	0.068 ± 0.037	-15.1 ± 4.0
Day 16	144 ± 3	0.086 ± 0.005	-8.7 ± 4.7
Day 20	138 ± 1	0.097 ± 0.027	-9.7 ± 4.0
Day 24	135 ± 3	0.040 ± 0.016	-10.6 ± 2.7
Day 28	127 ± 1	0.039 ± 0.038	-8.3 ± 0.9
Day 32	150 ± 10	0.066 ± 0.041	-10.1 ± 5.1

Both non-modified and Tf-modified TMZ+BTZ loaded PLGA NPs proved to be stable at simulated physiological conditions for the least 4 weeks, since no statistically significant changes were observed in the studied properties overtime ($p > 0.05$), therefore these are suitable to be used for GBM administration. In physiological conditions, the NP zeta potential suffers a decrease, exhibiting less negative values, since the NP were suspended in PBS. This occurs due to the free charges of PBS that interact with the surface chemical groups of the NPs [145]. However, despite these lower zeta potential values, the NPs remain stable. Beyond the electrostatic stabilization provided by the surface charges, the NPs colloidal stability is promoted by a steric stabilization due to the PVA. During NPs' formation, the PVA adsorbs to the NPs' surface preventing them from aggregate, therefore improving the stability of NP [146].

4.8 NPs' Antiproliferative Activity

To evaluate the *in vitro* antiproliferative activity of the developed Tf-TMZ+BTZ loaded PLGA NPs, two human GBM cells with different MGMT-expression were used. First, to assess the TMZ resistance of each cell line, both cells were treated with increasing concentrations of TMZ, and the obtained survival inhibition curves are presented in figure 20.

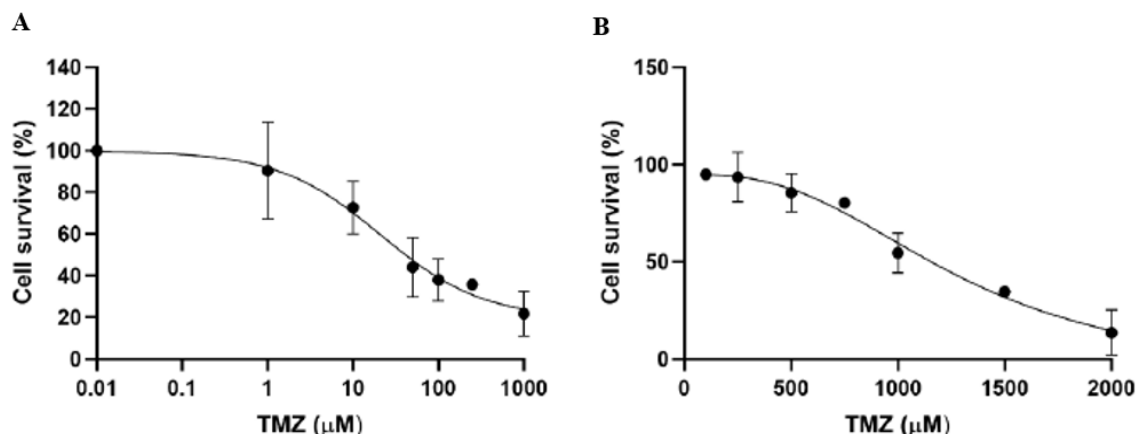


Figure 20 - Cell survival inhibition curve after 72 h treatment with free TMZ, free on two GBM human cells by SRB assay. (A) U251 cells and (B) T98G cells. Cell survival is presented as percent [(%) = ((T)/(C)) x 100]. Data represented as mean \pm SD (n=3).

The obtained survival inhibition curves show that free TMZ induced a concentration-related decrease in the survival of both cells lines and allowed for the determination of the IC₅₀ values (table 12). As depicted by the much higher IC₅₀ values obtained for the T98G cells (1.2 x 10⁶ μM, while for U251 41.2 is μM), these cells proved to be highly resistant to the TMZ effect due to being MGMT-positive cells, as well-reported in the literature [132].

Table 12 - Cytotoxic effects of the different treatments on the survival of U251 and T98G cell. Results are expressed as IC₅₀ values at 72h of exposure with free TMZ, free BTZ, free TMZ+BTZ and Tf-TMZ+BTZ PLGA NPs.

	IC ₅₀ (nM)			
	Free TMZ	Free BTZ	Free TMZ+BTZ	Tf-TMZ+BTZ PLGA NPs
U251	4.1 x 10 ⁴	1.29	1.42	1.14
T98G	1.2 x 10 ⁶	6.88	0.61	2.94

Then, the ability of BTZ in enhancing the *in vitro* effects of TMZ in both resistant and non-resistant GBM cells was evaluated. Two approaches were studied, to compare the therapeutic efficacy of the free combined therapy with the Tf-TMZ+BTZ PLGA NPs. The obtained results are presented in figure 21 and table 12. The studied TMZ:BTZ ratio (1:0.8) was chosen based on the EE (%) of both drugs in the developed NPs. In both treatment regimens (free or entrapped drugs), a concentration-related decrease in cell growth was observed (figure 21). By comparing the obtained IC₅₀ values (table 12), it is possible to conclude that the combination therapy of TMZ+BTZ inhibited the cellular proliferation more efficiently than free TMZ in both studied lines, resulting in much lower IC₅₀ values for free TMZ+BTZ and Tf-TMZ+BTZ PLGA NPs.

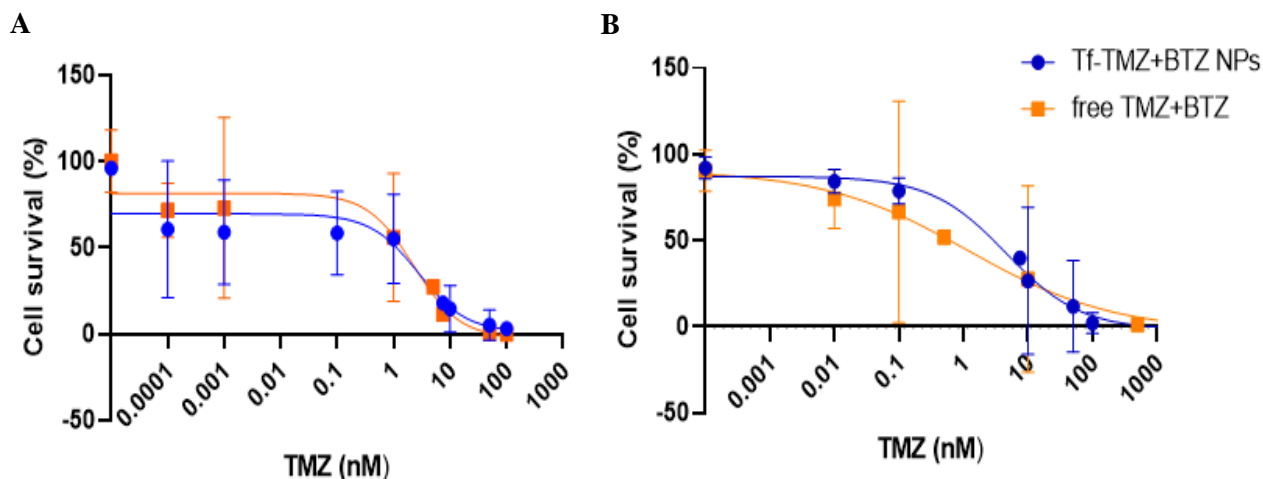


Figure 21 - Cell survival inhibition curve after 72 h co-treatment with TMZ and BTZ, free or entrapped in Tf-modified PLGA NPs, on two GBM human cells by SRB assay. (A) U251 cells and (B) T98G cells. Cell survival is presented as percent [$(\%) = ((T)/(C)) \times 100$]. Data represented as mean \pm SD (n=3).

The effect of the free combined therapy proved to be more pronounced for TMZ-resistant T98G cells, with the addition of BTZ leading to a decrease of the IC_{50} values in about 2 million times, while for U251 cells, a 30,000-fold decrease of the IC_{50} values was observed. This was expected since it is well-described the ability of the BTZ to inhibit the MGMT activity in T98G cells, leading to an increased antiproliferative activity [145, 146]. The improved anticancer activity in the MGMT-negative U251 cells can also be explained due to the fact that BTZ itself has also antiproliferative activity [149]. In fact, BTZ is a potent anticancer agent able to inhibit cell survival. Both cells were treated with free BTZ and a concentration-related decrease in cell growth was observed as depicted in the obtained cell survival inhibition curves presented in figure 22.

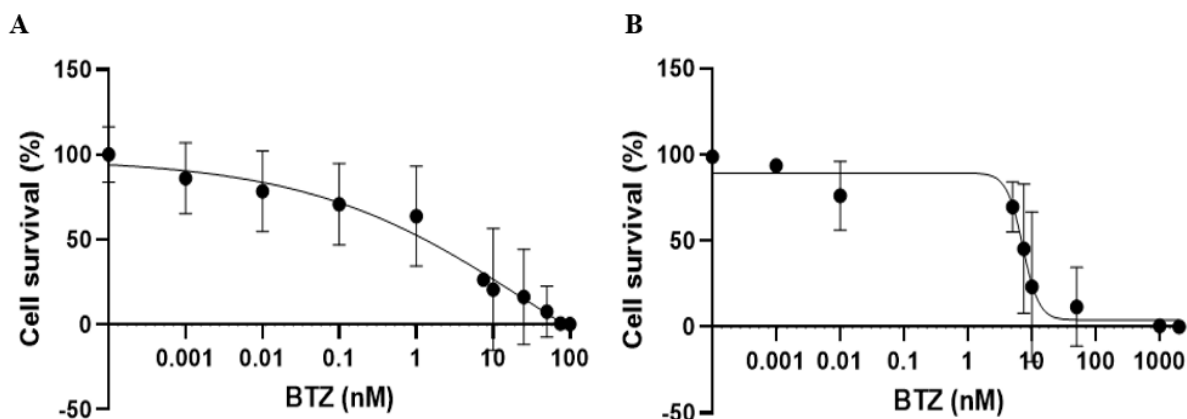


Figure 22 - Cell survival inhibition curve after 72 h treatment with free BTZ on two GBM human cells by SRB assay. (A) U251 cells and (B) T98G cells. Cell survival is presented as percent [$(\%) = ((T)/(C)) \times 100$]. Data represented as mean \pm SD (n=3).

Interestingly, it is also possible to observe, that while the TMZ+BTZ IC_{50} values are almost similar for U251 cells regardless of if the drugs were in the free form or entrapped in the Tf-

PLGA NPs, the IC_{50} values are higher for the NPs in the T98G cells. Apparently, the NPs were less efficient in inhibiting the cell survival than the free drugs. However, the Tf-TMZ+BTZ NPs are still much more efficient than free TMZ, as proved by the 400,000-fold lower IC_{50} values.

Thus, the developed Tf-TMZ+BTZ PLGA NPs proved to increase the efficiency of TMZ in both MGMT-positive and negative cells, being a promising approach for the co-therapy of GBM with both drugs.

Chapter 5

Conclusion and Future Perspectives

Over the last decades, nanomedicine has played a key role in the discovery and development of NPs that can be used in cancer diagnosis and treatment.

The therapeutic properties of TMZ, the most used drug for GBM treatment, are well documented and established in the literature. However, it has limited success mainly due to low bioavailability in the tumor tissue and intrinsic resistance mechanisms mediated by the MGMT protein. More recently, clinical trials revealed that concomitant therapy of TMZ with BTZ can improve the survival outcomes in GBM patients due to overcoming MGMT-mediated resistance. However, the systemic administration of both drugs presents limitations, and therefore their delivery using NPs can enhance their activity and reach the GBM target cells at effective therapeutic concentrations. In addition, the NPs' specificity can be enhanced by conjugating the NPs surface with specific ligands. In this work, an active targeting strategy of a drug delivery system is proposed for the treatment of GBM. Polymeric NPs of PLGA were used as nanocarriers to co-deliver TMZ and BTZ. The NPs' surface was conjugated with Tf to enhance their specificity for GBM and BBB cells.

First, an experimental design was applied to optimize the NPs preparation protocol. For that, a total of 27 formulations were prepared using a FFD augmented design. The effect of experimental independent variables was studied and modelled according to the obtained mathematical regression models. The main experimental variables affecting the physicochemical properties, NP size, PDI, zeta potential and EE of both drugs, were determined using statistical analysis (ANOVA). An optimized formulation was obtained using 19 mg of PLGA, 1.26 %PVA, 4 sonication cycles and 0.667 O/W ratio. These optimized formulations presented suitable values for GBM treatment application, sizes below 200 nm, low PDI values and negative zeta potentials. Furthermore, the optimized NPs exhibited high EE values.

Then, the NPs were conjugated with Tf, since its receptor is overexpressed in the BBB and GBM tumor cells, therefore enabling a dual-targeting approach. The Tf conjugation protocol did not significantly affect the NP properties (size, PDI and zeta potential), however, the Tf-conjugation protocol resulted in a 25% reduction in the EE of BTZ and 5% increase in EE of TMZ. Still, the obtained EE results remain within suitable values and was observed a sustained drugs release over 15 days from the PLGA matrix. The stability in storage and physiological conditions of the produced Tf- conjugated and non-conjugated NPs was evaluated. The results revealed that the NPs are stable in both conditions, crucial for biological applications, as NP need to stay stable until reach the target and along the drugs release.

In vitro studies were performed to evaluate the antiproliferative effect of the NPs. Free TMZ, free TMZ+BTZ and Tf-conjugated TMZ+BTZ PLGA NPs were evaluated using two human GBM cell lines, T98G and U251. Free TMZ induced a concentration-related decrease in the survival of both cell lines, however the combined therapy inhibited the cellular proliferation more efficiently than free TMZ in both studied lines, resulting in much lower IC₅₀ values for free TMZ+BTZ and Tf-TMZ+BTZ PLGA NPs. In conclusion, the developed Tf-TMZ+BTZ PLGA NPs proved to increase the efficiency of TMZ by in both MGMT-positive and negative cells, being a promising approach for the co-therapy of GBM with both drugs.

Further future experimental work is necessary to assess the nanosystem efficacy. Further cytotoxicity assays of free BTZ, TMZ+BTZ loaded PLGA NPs and TMZ+BTZ are fundamental and a third cell line will be studied, an immortalized human astrocyte (NHA). Future *in vivo* assays using animal models could also be tested, as pharmacokinetics and biodistribution studies.

References

- [1] Q. T. Ostrom, H. Gittleman, G. Truitt, A. Boscia, C. Kruchko, and J. S. Barnholtz-Sloan, “CBTRUS statistical report: Primary brain and other central nervous system tumors diagnosed in the United States in 2011-2015,” *Neuro Oncology*, vol. 20, pp. iv1–iv86, 2018, doi: 10.1093/neuonc/ny131.
- [2] R. Stupp, M. Brada, M. J. van den Bent, J. C. Tonn, and G. Pentheroudakis, “High-grade glioma: ESMO clinical practice guidelines for diagnosis, treatment and follow-up,” *Annals Oncology*, vol. 25, pp. 93–101, March 2014, doi: 10.1093/annonc/mdu050.
- [3] S. K. Carlsson, S. P. Brothers, and C. Wahlestedt, “Emerging treatment strategies for glioblastoma multiforme.,” *EMBO Molecular Medicine*, vol. 6, no. 11, pp. 1359–1370, November 2014, doi: 10.15252/emmm.201302627.
- [4] F. B. Furnari, T. Fenton, R. M. Bachoo, A. Mukasa, J. M. Stommel, A. Stegh, W. C. Hahn, K. L. Ligon, D. N. Louis, C. Brennan, L. Chin, R. A. DePinho and W. K. Cavenee, “Malignant astrocytic glioma: genetics, biology, and paths to treatment.,” *Genes & Development*, vol. 21, no. 21, pp. 2683–2710, November 2007, doi: 10.1101/gad.1596707.
- [5] C. P. Haar, P. Hebbar, and G. C. Wallace, “Drug resistance in glioblastoma: a mini review.,” *Neurochemical Research*, vol. 37, no. 6, pp. 1192–1200, June 2012, doi: 10.1007/s11064-011-0701-1.
- [6] A. Yoshino, A. Ogino, K. Yachi, T. Ohta, T. Fukushima, T. Watanabe, Y. Katayama, Y. Okamoto, N. Naruse, E. Sano, and K. Tsumoto, “Gene expression profiling predicts response to temozolomide in malignant gliomas.,” *International Journal of Oncology*, vol. 36, no. 6, pp. 1367–1377, June 2010, doi: 10.3892/ijo_00000621.
- [7] F. Accardi, D. Toscani, M. Bolzoni, B. Dalla Palma, F. Aversa, and N. Giuliani, “Mechanism of Action of Bortezomib and the New Proteasome Inhibitors on Myeloma Cells and the Bone Microenvironment: Impact on Myeloma-Induced Alterations of Bone Remodeling.” *BioMed Research International*, vol. 2015, p. 172458, 2015, doi: 10.1155/2015/172458.
- [8] B. Kaina, G. P. Margison, and M. Christmann, “Targeting O⁶-methylguanine-DNA methyltransferase with specific inhibitors as a strategy in cancer therapy.,” *Cellular and Molecular Life Sciences*, vol. 67, no. 21, pp. 3663–3681, November 2010, doi: 10.1007/s00018-010-0491-7.
- [9] O. van Tellingen, B. Yetkin-Arik, M. C. de Gooijer, P. Wesseling, T. Wurdinger, and H. E. de Vries, “Overcoming the blood-brain tumor barrier for effective glioblastoma treatment.,” *Drug Resistance Updates: Reviews and Commentaries in Antimicrobial and Anticancer Chemotherapy*, vol. 19, pp. 1–12, March 2015, doi: 10.1016/j.drup.2015.02.002.
- [10] M. A. Rahman, J. Brekke, V. Arnesen, M. H. Hannisdal, A. G. Navarro, A. Waha, L. Herfindal, C. B. Rygh, E. Bratland, P. Brandal, J. Haasz, L. Oltedal, H. Miletic, A. Lundervold, S. A. Lie, D. Goplen, and M. Chekenya, “Sequential bortezomib and temozolomide treatment promotes immunological responses in glioblastoma patients with positive clinical outcomes: A phase 1B study.,” *Immunity, Inflammation and Disease*, vol.

- 8, no. 3, pp. 342–359, September 2020, doi: 10.1002/iid3.315.
- [11] Y. Xin, Q. Huang, J. Q. Tang, X. Y. Hou, P. Zhang, L. Z. Zhang, and G. Jiang, “Nanoscale drug delivery for targeted chemotherapy.,” *Cancer Letters*, vol. 379, no. 1, pp. 24–31, August 2016, doi: 10.1016/j.canlet.2016.05.023.
- [12] F. Danhier, E. Ansorena, J. M. Silva, R. Coco, A. Le Breton, and V. Préat, “PLGA-based nanoparticles: an overview of biomedical applications.,” *Journal of Controlled Release*, vol. 161, no. 2, pp. 505–522, July 2012, doi: 10.1016/j.jconrel.2012.01.043.
- [13] H. Ohgaki and P. Kleihues, “The definition of primary and secondary glioblastoma.,” *Clinical Cancer Research*, vol. 19, no. 4, pp. 764–772, 2013, doi: 10.1158/1078-0432.CCR-12-3002.
- [14] A. Gutkin, Z. R. Cohen, and D. Peer, “Harnessing nanomedicine for therapeutic intervention in glioblastoma.,” *Expert Opinion on Drug Delivery*, vol. 13, no. 11, pp. 1573–1582, November 2016, doi: 10.1080/17425247.2016.1200557.
- [15] A. Misra, S. Ganesh, A. Shahiwala, and S. P. Shah, “Drug delivery to the central nervous system: a review.,” *Journal of Pharmacy & Pharmaceutical Sciences*, vol. 6, no. 2, pp. 252–273, 2003.
- [16] J. Martinez-Quintanilla, D. Bhere, P. Heidari, D. He, U. Mahmood, and K. Shah, “Therapeutic efficacy and fate of bimodal engineered stem cells in malignant brain tumors.,” *Stem Cells*, vol. 31, no. 8, pp. 1706–1714, August 2013, doi: 10.1002/stem.1355.
- [17] M. L. Goodenberger and R. B. Jenkins, “Genetics of adult glioma.,” *Cancer Genetics*, vol. 205, no. 12, pp. 613–621, December 2012, doi: 10.1016/j.cancergen.2012.10.009.
- [18] A. Omuro and L. M. DeAngelis, “Glioblastoma and other malignant gliomas: a clinical review.,” *JAMA*, vol. 310, no. 17, pp. 1842–1850, November 2013, doi: 10.1001/jama.2013.280319.
- [19] B. Mujokoro, M. Adabi, E. Sadroddiny, M. Adabi, and M. Khosravani, “Nano-structures mediated co-delivery of therapeutic agents for glioblastoma treatment: A review.,” *Materials Science & Engineering C. Materials for Biological Applications*, vol. 69, pp. 1092–1102, December 2016, doi: 10.1016/j.msec.2016.07.080.
- [20] Y. Wang and T. Jiang, “Understanding high grade glioma: molecular mechanism, therapy and comprehensive management.,” *Cancer Letters*, vol. 331, no. 2, pp. 139–146, May 2013, doi: 10.1016/j.canlet.2012.12.024.
- [21] X. Zhang, W. Zhang, W.-D. Cao, G. Cheng, and Y.-Q. Zhang, “Glioblastoma multiforme: Molecular characterization and current treatment strategy (Review).,” *Experimental and Therapeutic Medicine*, vol. 3, no. 1, pp. 9–14, January 2012, doi: 10.3892/etm.2011.367.
- [22] I. Z. Renault and D. Golgher, “Molecular genetics of glioblastomas: defining subtypes and understanding the biology.,” *Neuroimaging Clinics of North America*, vol. 25, no. 1, pp. 97–103, February 2015, doi: 10.1016/j.nic.2014.09.007.
- [23] S. Karcher, H. H. Steiner, R. Ahmadi, S. Zoubaa, G. Vasvari, H. Bauer, A. Unterberg, and C. Herold-Mende, “Different angiogenic phenotypes in primary and secondary glioblastomas.,” *International Journal of Cancer*, vol. 118, no. 9, pp. 2182–2189, May 2006, doi: 10.1002/ijc.21648.
- [24] R. Batash, N. Asna, P. Schaffer, N. Francis, and M. Schaffer, “Glioblastoma Multiforme, Diagnosis and Treatment; Recent Literature Review,” *Current Medicinal Chemistry*, pp. 3002–3009, 2017, doi: 10.2174/0929867324666170516123206.
- [25] F. Yamasaki, K. Kurisu, K. Satoh, K. Arita, K. Sugiyama, M. Ohtaki, J. Takaba, A. Tom-inaga, R. Hanaya, H. Yoshioka, S. Hama, Y. Ito, Y. Kajiwara, K. Yahara, T. Saito, and M. A. Thohar, “Apparent diffusion coefficient of human brain tumors at MR imaging.,” *Radiology*, vol. 235, no. 3, pp. 985–991, June 2005, doi: 10.1148/radiol.2353031338.
- [26] A. Gupta, R. J. Young, A. D. Shah, A. D. Schweitzer, J. J. Graber, W. Shi, Z. Zhang, J. Huse, and A. M. Omuro, “Pretreatment Dynamic Susceptibility Contrast MRI Perfusion in Glioblastoma: Prediction of EGFR Gene Amplification.,” *Clinical Neuroradiology*, vol. 25, no. 2, pp. 143–150, June 2015, doi: 10.1007/s00062-014-0289-3.
- [27] R. G. W. Verhaak, K. A. Hoadley, E. Purdom, V. Wang, Y. Qi, M. D. Wilkerson, C. R. Miller, L. Ding, T. Golub, J. P. Mesirov, G. Alexe, M. Lawrence, M. O’Kelly, P. Tamayo,

- B. A. Weir, S. Gabriel, W. Winckler, S. Gupta, L. Jakkula, H. Feiler, “Integrated Genomic Analysis Identifies Clinically Relevant Subtypes of Glioblastoma Characterized by Abnormalities in PDGFRA, IDH1, EGFR, and NF1,” *Cancer Cell*, vol. 17, no. 1, pp. 98–110, 2010, doi: 10.1016/j.ccr.2009.12.020.
- [28] G. D. Cha, T. Kang, S. Baik, D. Kim, S. H. Choi, T. Hyeon, D. Kim, “Advances in drug delivery technology for the treatment of glioblastoma multiforme,” *Journal of Controlled Release*, vol. 328, pp. 350–367, September 2020, doi: 10.1016/j.jconrel.2020.09.002.
- [29] S. S. Kim, A. Rait, E. Kim, K. F. Pirollo, M. Nishida, N. Farkas, J. A. Dagata, and E. H. Chang, “A nanoparticle carrying the p53 gene targets tumors including cancer stem cells, sensitizes glioblastoma to chemotherapy and improves survival,” *ACS Nano*, vol. 8, no. 6, pp. 5494–5514, 2014, doi: 10.1021/nn5014484.
- [30] R. Carruthers and A. J. Chalmers, “The potential of PARP inhibitors in neuro-oncology.,” *CNS Oncology*, vol. 1, no. 1, pp. 85–97, Sep. 2012, doi: 10.2217/cns.12.13.
- [31] M. Zhao, D. van Straten, M. L. D. Broekman, V. Pr eat, and R. M. Schiffelers, “Nanocarrier-based drug combination therapy for glioblastoma.,” *Theranostics*, vol. 10, no. 3, pp. 1355–1372, 2020, doi: 10.7150/thno.38147.
- [32] E. R. Laws, I. F. Parney, W. Haug, F. Anderson, A. M. Morris, A. Asher, K. O. Lillehei, M. Bernstein, H. Brem, A. Sloan, M. S. Berger and S. Chang, “Survival following surgery and prognostic factors for recently diagnosed malignant glioma: data from the Glioma Outcomes Project.,” *Journal of Neurosurgery*, vol. 99, no. 3, pp. 467–473, September 2003, doi: 10.3171/jns.2003.99.3.0467.
- [33] M. Ameratunga, M. Khasraw, R. Grant, H. Wheeler, and N. Pavlakis, “Anti-angiogenic therapy for high-grade glioma (Review),” 2018, doi: 10.1002/14651858.CD008218.
- [34] N. Marchi, G. Betto, V. Fazio, Q. Fan, C. Ghosh, A. Machado and D. Janigro “Blood-brain barrier damage and brain penetration of antiepileptic drugs: Role of serum proteins and brain edema,” *Epilepsia*, vol. 50, no. 4, pp. 664–677, 2009, doi: 10.1111/j.1528-1167.2008.01989.x.
- [35] V. A. Boussiotis and A. Charest, “Immunotherapies for malignant glioma.,” *Oncogene*, vol. 37, no. 9, pp. 1121–1141, Mar. 2018, doi: 10.1038/s41388-017-0024-z.
- [36] G. D. Cha, T. Kang, S. Baik, D. Kim, S. H. Choi, T. Hyeon and D.-H. Kim, “Advances in drug delivery technology for the treatment of glioblastoma multiforme,” *Journal of Controlled Release*, vol. 328, pp. 350–367, 2020, doi: <https://doi.org/10.1016/j.jconrel.2020.09.002>.
- [37] R. Stupp, S. Taillibert, A. A. Kanner, S. Kesari, D. M. Steinberg, S. A. Toms, L. P. Taylor, F. Lieberman, A. Silvani, K. L. Fink, G. H. Barnett, J. J. Zhu, J. W. Henson, H. H. Engelhard, T. C. Chen, D. D. Tran, J. Sroubek, N. D. Tran, A. F. Hottinger, J. Landolfi, and Z. Ram, “Maintenance therapy with tumor-Treating fields plus temozolomide vs temozolomide alone for glioblastoma a randomized clinical trial,” *JAMA - Journal of American Medical Association*, vol. 314, no. 23, pp. 2535–2543, 2015, doi: 10.1001/jama.2015.16669.
- [38] “Principles of Neuro-Oncology: Edited by David Schiff and Brian Patrick O’Neill. McGraw-Hill, New York, 2005, 750 pp. \$125.00, ISBN 0-07-142515-2.,” *Neuro-Oncology*, vol. 8, no. 2, pp. 193–194, April 2006, doi: 10.1215/15228517-2005-001.
- [39] C. L. Moody and R. T. Wheelhouse, “The medicinal chemistry of imidazotetrazine prodrugs.,” *Pharmaceuticals (Basel)*, vol. 7, no. 7, pp. 797–838, July 2014, doi: 10.3390/ph7070797.
- [40] E. S. Newlands, G. R. Blackledge, J. A. Slack, G. J. Rustin, D. B. Smith, N. S. Stuart, C. P. Quarterman, R. Hoffman, M. F. Stevens, and M. H. Brampton, “Phase I trial of temozolomide (CCRG 81045: M&B 39831: NSC 362856).,” *British Journal of Cancer*, vol. 65, no. 2, pp. 287–291, February 1992, doi: 10.1038/bjc.1992.57.
- [41] D. T. Nagasawa, F. Chow, A. Yew, W. Kim, N. Cremer, and I. Yang, “Temozolomide and Other Potential Agents for the Treatment of Glioblastoma Multiforme,” *Neurosurgery Clinics of North America*, vol. 23, no. 2, pp. 307–322, 2012, doi: 10.1016/j.nec.2012.01.007.

- [42] M. Andradi, R. Bustos, A. Gaspar, F. A. Gomez, and A. Klekner, "Analysis and stability study of temozolomide using capillary electrophoresis.," *Journal of Chromatography B, Analytical Technologies in the Biomedical and Life Sciences*, vol. 878, no. 21, pp. 1801–1808, July 2010, doi: 10.1016/j.jchromb.2010.05.008.
- [43] J. Zhang, M. F.G. Stevens, and T. D. Bradshaw, "Temozolomide: Mechanisms of Action, Repair and Resistance," *Current Molecular Pharmacology*, vol. 5, no. 1, pp. 102–114, 2011, doi: 10.2174/1874467211205010102.
- [44] R. Stupp, W. P. Mason, M. J. van den Bent, M. Weller, B. Fisher, M. J. Taphoorn, K. Belanger, A. A. Brandes, C. Marosi, U. Bogdahn, J. Curschmann, R. C. Janzer, S. K. Ludwin, T. Gorlia, A. Allgeier, D. Lacombe, J. G. Cairncross, E. Eisenhauer and R. O. Mirimanoff, "Radiotherapy plus Concomitant and Adjuvant Temozolomide for Glioblastoma," *New England Journal of Medicine*, vol. 352, no. 10, pp. 987–996, March 2005, doi: 10.1056/NEJMoa043330.
- [45] F. Marchesi, M. Turriziani, G. Tortorelli, G. Avvisati, F. Torino, and L. De Vecchis, "Triazene compounds: Mechanism of action and related DNA repair systems," *Pharmacology Research*, vol. 56, no. 4, pp. 275–287, 2007, doi: 10.1016/j.phrs.2007.08.003.
- [46] Y. R. Lawrence, M. Wang, A. P. Dicker, D. Andrews, W. J. Curran, J. M. Michalski, L. Souhami, W. K. Yung and M. Mehta, "Early toxicity predicts long-term survival in high-grade glioma.," *British Journal of Cancer*, vol. 104, no. 9, pp. 1365–1371, April 2011, doi: 10.1038/bjc.2011.123.
- [47] G. Lanzetta, C. Campanella, A. Rozzi, M. Nappa, A. Costa, F. Fedele, G. Innocenzi, F. M. Gagliardi, M. Salvati, G. Minniti, A. Frati, L. Frati, and A. Vecchione, "Temozolomide in radio-chemotherapy combined treatment for newly-diagnosed glioblastoma multiforme: phase II clinical trial.," *Anticancer Research*, vol. 23, no. 6D, pp. 5159–5164, 2003.
- [48] M. C. Chamberlain, "Temozolomide: Therapeutic limitations in the treatment of adult high-grade gliomas," *Expert Review of Neurotherapeutics*, vol. 10, no. 10, pp. 1537–1544, 2010, doi: 10.1586/ern.10.32.
- [49] M. J. Ramalho, S. Andrade, M. Á. N. Coelho, J. A. Loureiro, and M. C. Pereira, "Biophysical interaction of temozolomide and its active metabolite with biomembrane models: The relevance of drug-membrane interaction for Glioblastoma Multiforme therapy.," *European Journal of Pharmaceutics and Biopharmaceutics*, vol. 136, pp. 156–163, March 2019, doi: 10.1016/j.ejpb.2019.01.015.
- [50] R. Karim, C. Palazzo, B. Evrard, and G. Piel, "Nanocarriers for the treatment of glioblastoma multiforme: Current state-of-the-art," *Journal of Controlled Release*, vol. 227, pp. 23–37, 2016, doi: 10.1016/j.jconrel.2016.02.026.
- [51] M. Fakhoury, "Drug delivery approaches for the treatment of glioblastoma multiforme," *Artificial Cells, Nanomedicine and Biotechnology*, vol. 44, no. 6, pp. 1365–1373, 2016, doi: 10.3109/21691401.2015.1052467.
- [52] W.-Y. Liu, Z.-B. Wang, L.-C. Zhang, X. Wei, and L. Li, "Tight junction in blood-brain barrier: an overview of structure, regulation, and regulator substances.," *CNS Neuroscience & Therapeutics*, vol. 18, no. 8, pp. 609–615, August 2012, doi: 10.1111/j.1755-5949.2012.00340.x.
- [53] D. S. Hersh, A. S. Wadajkar, N. Roberts, J. G. Perez, N. P. Connolly, V. Frenkel, J. A. Winkles, G. F. Woodworth, and A. J. Kim, "Evolving Drug Delivery Strategies to Overcome the Blood Brain Barrier.," *Current Pharmaceutical Design*, vol. 22, no. 9, pp. 1177–1193, 2016, doi: 10.2174/1381612822666151221150733.
- [54] F. Hervé, N. Ghinea, and J.-M. Scherrmann, "CNS delivery via adsorptive transcytosis.," *AAPS Journal*, vol. 10, no. 3, pp. 455–472, September 2008, doi: 10.1208/s12248-008-9055-2.
- [55] K. E. Schlageter, P. Molnar, G. D. Lapin, and D. R. Groothuis, "Microvessel organization and structure in experimental brain tumors: microvessel populations with distinctive structural and functional properties.," *Microvascular Research*, vol. 58, no. 3, pp. 312–328, November 1999, doi: 10.1006/mvre.1999.2188.

- [56] J. M. Squire, M. Chew, G. Nneji, C. Neal, J. Barry, and C. Michel, “Quasi-periodic substructure in the microvessel endothelial glycocalyx: A possible explanation for molecular filtering?,” *Journal of Structural Biology*, vol. 136, no. 3, pp. 239–255, 2001, doi: 10.1006/jsbi.2002.4441.
- [57] J. K. Horton and S. H. Wilson, “Hypersensitivity phenotypes associated with genetic and synthetic inhibitor-induced base excision repair deficiency,” *DNA Repair (Amst.)*, vol. 6, no. 4, pp. 530–543, 2007, doi: 10.1016/j.dnarep.2006.10.016.
- [58] K. K. Khanna, M. F. Lavin, S. P. Jackson, and T. D. Mulhern, “ATM, a central controller of cellular responses to DNA damage.,” *Cell Death Differentiation*, vol. 8, no. 11, pp. 1052–1065, November 2001, doi: 10.1038/sj.cdd.4400874.
- [59] P. J. Vlachostergios, E. Hatzidaki, N. E. Stathakis, G. K. Koukoulis, and C. N. Papandreou, “Bortezomib downregulates MGMT expression in T98G glioblastoma cells,” *Cellular Molecular Neurobiology*, vol. 33, no. 3, pp. 313–318, 2013, doi: 10.1007/s10571-013-9910-2.
- [60] B. Gong, M. Radulovic, M. E. Figueiredo-Pereira, and C. Cardozo, “The Ubiquitin-Proteasome System: Potential Therapeutic Targets for Alzheimer’s Disease and Spinal Cord Injury,” *Frontiers in Molecular Neuroscience*, vol. 9, 2016, doi: 10.3389/fnmol.2016.00004.
- [61] D. Cousin, M. G. Hummersone, T. D. Bradshaw, J. Zhang, C. J. Moody, M. B. Foreiter, H. S. Summers, W. Lewis, R. T. Wheelhouse and M. F. Stevens, “Synthesis and growth-inhibitory activities of imidazo[5,1-d]-1,2,3,5-tetrazine-8-carboxamides related to the anti-tumour drug temozolomide, with appended silicon, benzyl and heteromethyl groups at the 3-position.,” *MedChemComm*, vol. 9, no. 3, pp. 545–553, March 2018, doi: 10.1039/c7md00554g.
- [62] J. W. Taylor and D. Schiff, “Treatment Considerations for MGMT-Unmethylated Glioblastoma,” *Current Neurology Neuroscience Reports*, vol. 15, no. 1, pp. 1–6, 2015, doi: 10.1007/s11910-014-0507-z.
- [63] M. Esteller, S. R. Hamilton, P. C. Burger, S. B. Baylin, and J. G. Herman, “Inactivation of the DNA repair gene O6-methylguanine-DNA methyltransferase by promoter hypermethylation is a common event in primary human neoplasia.,” *Cancer Research*, vol. 59, no. 4, pp. 793–797, February 1999.
- [64] A. Papachristodoulou, R. D. Signorell, B. Werner, D. Brambilla, P. Luciani, M. Cavusoglu, J. Grandjean, M. Silginer, M. Rudin, E. Martin, M. Weller, P. Roth, and J. C. Leroux, “Chemotherapy sensitization of glioblastoma by focused ultrasound-mediated delivery of therapeutic liposomes,” *Journal of Controlled Release*, vol. 295, no. May 2018, pp. 130–139, 2019, doi: 10.1016/j.jconrel.2018.12.009.
- [65] M. Esteller and J. G. Herman, “Generating mutations but providing chemosensitivity: the role of O6-methylguanine DNA methyltransferase in human cancer,” *Oncogene*, vol. 23, no. 1, pp. 1–8, 2004, doi: 10.1038/sj.onc.1207316.
- [66] K. H. Tomaszowski, R. Schirrmacher, and B. Kaina, “Multidrug Efflux Pumps Attenuate the Effect of MGMT Inhibitors,” *Molecular Pharmaceutics*, vol. 12, no. 11, pp. 3924–3934, 2015, doi: 10.1021/acs.molpharmaceut.5b00341.
- [67] C. Avendaño and J. C. Menéndez, “Chapter 14 - Drugs That Modulate Resistance to Antitumor Agents,” C. Avendaño and E. Menéndez, Eds. Boston: Elsevier, 2015, pp. 655–700.
- [68] B. Verbeek, T. D. Southgate, D. E. Gilham, and G. P. Margison, “O6-Methylguanine-DNA methyltransferase inactivation and chemotherapy,” *British Medical Bulletin*, vol. 85, no. 1, pp. 17–33, 2008, doi: 10.1093/bmb/ldm036.
- [69] A. M. Morás, J. G. Henn, L. Steffens Reinhardt, G. Lenz, and D. J. Moura, “Recent developments in drug delivery strategies for targeting DNA damage response in glioblastoma,” *Life Science*, vol. 287, no. October, 2021, doi: 10.1016/j.lfs.2021.120128.
- [70] National Center for Biotechnology Information (US), “The p53 tumor suppressor protein,” no. Md, pp. 346–355, 1998, [Online]. Available: <https://www.ncbi.nlm.nih.gov/books/NBK22268/>.

- [71] D. Bocangel, S. Sengupta, S. Mitra, and K. K. Bhakat, “p53-Mediated down-regulation of the human DNA repair gene O6-methylguanine-DNA methyltransferase (MGMT) via interaction with Sp1 transcription factor.,” *Anticancer Research*, vol. 29, no. 10, pp. 3741–3750, October 2009.
- [72] Y. Kinashi, T. Ikawa, and S. Takahashi, “The combined effect of neutron irradiation and temozolomide on glioblastoma cell lines with different MGMT and P53 status.,” *Applied Radiation and Isotopes*, vol. 163, p. 109204, September 2020, doi: 10.1016/j.apradiso.2020.109204.
- [73] B. England, T. Huang, and M. Karsy, “Current understanding of the role and targeting of tumor suppressor p53 in glioblastoma multiforme,” *Tumor Biology*, vol. 34, no. 4, pp. 2063–2074, 2013, doi: 10.1007/s13277-013-0871-3.
- [74] W. P. Roos, L. F. Batista, S. C. Naumann, W. Wick, M. Weller, C. F. Menck, and B. Kaina, “Apoptosis in malignant glioma cells triggered by the temozolomide-induced DNA lesion O6-methylguanine.,” *Oncogene*, vol. 26, no. 2, pp. 186–197, January 2007, doi: 10.1038/sj.onc.1209785.
- [75] G. C. Bobustuc, G. C., Bobustuc, C. H., Baker, A. Limaye, W. D. Jenkins, G. Pearl, N. G. Avgeropoulos and S. D. Konduri., “Levetiracetam enhances p53-mediated MGMT inhibition and sensitizes glioblastoma cells to temozolomide.,” *Neuro. Oncology*, vol. 12, no. 9, pp. 917–927, September 2010, doi: 10.1093/neuonc/noq044.
- [76] M. Gallitto, R. Cheng, J. F. Inocencio, H. Wang, Y. Zhang, G. Deikus, I. Wasserman, M. Strahl, M. Smith, R. Sebra, and R. L. Yong, “Epigenetic preconditioning with decitabine sensitizes glioblastoma to temozolomide via induction of MLH1.,” *Journal of Neurooncology*, vol. 147, no. 3, pp. 557–566, May 2020, doi: 10.1007/s11060-020-03461-4.
- [77] X. Miles, C. Vandevoorde, A. Hunter, and J. Bolcaen, “MDM2/X Inhibitors as Radiosensitizers for Glioblastoma Targeted Therapy.,” *Frontiers in Oncology*, vol. 11, p. 703442, 2021, doi: 10.3389/fonc.2021.703442.
- [78] M. H. Sung, L. Bagain, Z. Chen, T. Karpova, X. Yang, C. Silvin, T. C. Voss, J. G. McNally, C. Van Waes, and G. L. Hager, “Dynamic effect of bortezomib on nuclear factor-kappaB activity and gene expression in tumor cells.,” *Molecular Pharmacology*, vol. 74, no. 5, pp. 1215–1222, November 2008, doi: 10.1124/mol.108.049114.
- [79] L. Tang, J. Li, Q. Zhao, T. Pan, H. Zhong, and W. Wang, “Advanced and innovative nano-systems for anticancer targeted drug delivery,” *Pharmaceutics*, vol. 13, no. 8, pp. 1–30, 2021, doi: 10.3390/pharmaceutics13081151.
- [80] G. Unsoy, “The Synthesis and characterization of doxorubicin and bortezomib loaded magnetic nanoparticles for targeting tumor cells (Thesis)”, Dept. of natural and applied sciences, Middle east technical university” 2013.
- [81] E. Pérez-Herrero and A. Fernández-Medarde, “Advanced targeted therapies in cancer: Drug nanocarriers, the future of chemotherapy.,” *European Journal of Pharmaceutical Biopharmacy*, vol. 93, pp. 52–79, June 2015, doi: 10.1016/j.ejpb.2015.03.018.
- [82] M. Creixell and N. A. Peppas, “Co-delivery of siRNA and therapeutic agents using nanocarriers to overcome cancer resistance,” *Nano Today*, vol. 7, no. 4, pp. 367–379, 2012, doi: 10.1016/j.nantod.2012.06.013.
- [83] G. Gasparini, R. G. Holdich, and S. R. Kosvintsev, “PLGA particle production for water-soluble drug encapsulation: Degradation and release behaviour,” *Colloids Surfaces B Biointerfaces*, vol. 75, no. 2, pp. 557–564, 2010, doi: 10.1016/j.colsurfb.2009.09.035.
- [84] D. Pissuwan, T. Niidome, and M. B. Cortie, “The forthcoming applications of gold nanoparticles in drug and gene delivery systems.,” *Journal of Controlled Release*, vol. 149, no. 1, pp. 65–71, January 2011, doi: 10.1016/j.jconrel.2009.12.006.
- [85] Y. Li and H. Zhang, “Nanoparticle-Based Drug Delivery Systems for Enhanced Tumor-Targeting Treatment.,” *Journal of Biomedical Nanotechnology*, vol. 15, no. 1, pp. 1–27, January 2019, doi: 10.1166/jbn.2019.2670.
- [86] X. Xie, Y. Zhang, F. Li, T. Lv, Z. Li, H. Chen, L. Jia, and Y. Gao, “Challenges and Opportunities from Basic Cancer Biology for Nanomedicine for Targeted Drug Delivery,”

- Current Cancer Drug Targets*, vol. 18, June 2018, doi: 10.2174/1568009618666180628160211.
- [87] C. Zhan and W. Lu, “The blood-brain/tumor barriers: challenges and chances for malignant gliomas targeted drug delivery.,” *Current Pharmaceutical Biotechnology*, vol. 13, no. 12, pp. 2380–2387, September 2012, doi: 10.2174/138920112803341798.
- [88] L. Nam, C. Coll, L. Erthal, C. de la Torre, D. Serrano, R. Martínez-Máñez, M. J. Santos-Martínez, and E. Ruiz-Hernández, “Drug delivery nanosystems for the localized treatment of glioblastoma multiforme,” *Materials (Basel)*, vol. 11, no. 5, 2018, doi: 10.3390/ma11050779.
- [89] S. C. J. Steiniger, J. Kreuter, A. S. Khalansky, I. N. Skidan, A. I. Bobruskin, Z. S. Smirnova, S. E. Severin, R. Uhl, M. Kock, K. D. Geiger, and S. E. Gelperina, “Chemotherapy of glioblastoma in rats using doxorubicin-loaded nanoparticles.,” *International Journal of Cancer*, vol. 109, no. 5, pp. 759–767, May 2004, doi: 10.1002/ijc.20048.
- [90] M. P. Pinto, M. Arce, B. Yameen, and C. Vilos, “Targeted brain delivery nanoparticles for malignant gliomas.,” *Nanomedicine (Lond)*, vol. 12, no. 1, pp. 59–72, January 2017, doi: 10.2217/nmm-2016-0307.
- [91] F. Danhier, “To exploit the tumor microenvironment: Since the EPR effect fails in the clinic, what is the future of nanomedicine?,” *Journal of Controlled. Release*, vol. 244, no. Pt A, pp. 108–121, December 2016, doi: 10.1016/j.jconrel.2016.11.015.
- [92] P. V. Pawar, A. J. Domb, and N. Kumar, “Systemic Targeting Systems-EPR Effect, Ligand Targeting Systems,” 2014.
- [93] C. Fang, K. Wang, Z. R. Stephen, Q. Mu, F. M. Kievit, D. T. Chiu, O. W. Press and M. Zhang, “Temozolomide nanoparticles for targeted glioblastoma therapy,” *ACS Applied Materials & Interfaces*, vol. 7, no. 12, pp. 6674–6682, 2015, doi: 10.1021/am5092165.
- [94] H. Xin, X. Jiang, J. Gu, X. Sha, L. Chen, K. Law, Y. Chen, X. Wang, Y. Jiang, and X. Fang, “Angiopep-conjugated poly(ethylene glycol)-co-poly(ϵ -caprolactone) nanoparticles as dual-targeting drug delivery system for brain glioma.,” *Biomaterials*, vol. 32, no. 18, pp. 4293–4305, June 2011, doi: 10.1016/j.biomaterials.2011.02.044.
- [95] P. Zhang, L. Hu, Q. Yin, L. Feng, and Y. Li, “Transferrin-modified c[RGDfK]-paclitaxel loaded hybrid micelle for sequential blood-brain barrier penetration and glioma targeting therapy.,” *Molecular Pharmaceutics*, vol. 9, no. 6, pp. 1590–1598, June 2012, doi: 10.1021/mp200600t.
- [96] M. Luo, G. Lewik, J. C. Ratcliffe, C. H. Choi, E. Makila, W. Y. Tong and N. H. Voelcker, “Systematic Evaluation of Transferrin-Modified Porous Silicon Nanoparticles for Targeted Delivery of Doxorubicin to Glioblastoma,” *ACS Applied Materials & Interfaces*, vol. 11, no. 37, pp. 33637–33649, 2019, doi: 10.1021/acsami.9b10787.
- [97] L. Qian, J. Zheng, K. Wang, Y. Tang, X. Zhang, H. Zhang, F. Huang, Y. Pei, and Y. Jiang, “Cationic core-shell nanoparticles with carmustine contained within O6-benzylguanine shell for glioma therapy,” *Biomaterials*, vol. 34, no. 35, pp. 8968–8978, 2013, doi: 10.1016/j.biomaterials.2013.07.097.
- [98] M. J. Ramalho, J. A. Loureiro, M. A. N. Coelho, and M. C. Pereira, “Factorial Design as a Tool for the Optimization of PLGA Nanoparticles for the Co-Delivery of Temozolomide and O6-Benzylguanine,” *Pharmaceutics*, vol. 11, no. 8, p. 401, August 2019, doi: 10.3390/pharmaceutics11080401.
- [99] S. J. Liu, T. C. Yang, S. T. Yang, Y. C. Chen, and Y. Y. Tseng, “Biodegradable hybrid-structured nanofibrous membrane supported chemoprotective gene therapy enhances chemotherapy tolerance and efficacy in malignant glioma rats,” *Artificial Cells, Nanomedicine and Biotechnology*, vol. 46, no. sup2, pp. 515–526, 2018, doi: 10.1080/21691401.2018.1460374.
- [100] R. D. Signorell, A. Papachristodoulou, J. Xiao, B. Arpagaus, T. Casalini, J. Grandjean, J. Thamm, F. Steiniger, P. Luciani, D. Brambilla, B. Werner, E. Martin, M. Weller, P. Roth, and J. C. Leroux, “Preparation of PEGylated liposomes incorporating lipophilic lomeguatrib derivatives for the sensitization of chemo-resistant gliomas,” *International Journal of Pharmaceutics*, vol. 536, no. 1, pp. 388–396, 2018, doi:

- 10.1016/j.ijpharm.2017.11.070.
- [101] Z. R. Stephen, F. M. Kievit, O. Veiseh, P. A. Chiarelli, C. Fang, K. Wang, S. J. Hatzinger, R. G. Ellenbogen, J. R. Silber, and M. Zhang, “Redox-Responsive Magnetic Nanoparticle for Targeted Convection-Enhanced Delivery of O6-Benzylguanine to Brain Tumors,” *ACS Nano*, vol. 8, no. 10, pp. 10383–10395, October 2014, doi: 10.1021/nn503735w.
- [102] Z. R. Stephen, R. N. Gebhart, M. Jeon, A. A. Blair, R. G. Ellenbogen, J. R. Silber, and M. Zhang, “PH-sensitive O6-benzylguanosine polymer modified magnetic nanoparticles for treatment of glioblastomas,” *Bioconjugate Chemistry*, vol. 28, no. 1, pp. 194–202, 2017, doi: 10.1021/acs.bioconjchem.6b00545.
- [103] Q. Mu, G. Lin, V. K. Patton, K. Wang, O. W. Press, and M. Zhang, “Gemcitabine and chlorotoxin conjugated iron oxide nanoparticles for glioblastoma therapy,” *Journal of Materials and Chemistry. B*, vol. 4, no. 1, pp. 32–36, 2016, doi: 10.1039/c5tb02123e.
- [104] C. Bastiancich, G. Bastiat, and F. Lagarce, “Gemcitabine and glioblastoma: challenges and current perspectives,” *Drug Discovery Today*, vol. 23, no. 2, pp. 416–423, 2018, doi: <https://doi.org/10.1016/j.drudis.2017.10.010>.
- [105] T. Kato, A. Natsume, H. Toda, H. Iwamizu, T. Sugita, R. Hachisu, R. Watanabe, K. Yuki, K. Motomura, K. Bankiewicz, and T. Wakabayashi, “Efficient delivery of liposome-mediated MGMT-siRNA reinforces the cytotoxicity of temozolomide in GBM-initiating cells,” *Gene Therapy*, vol. 17, no. 11, pp. 1363–1371, 2010, doi: 10.1038/gt.2010.88.
- [106] T. Tsujiuchi, A. Natsume, K. Motomura, G. Kondo, M. Ranjit, R. Hachisu, I. Sugimura, S. Tomita, I. Takehara, M. Woolley, N. U. Barua, S. S. Gill, A. S. Bienemann, Y. Yamashita, S. Toyokuni, and T. Wakabayashi, “Preclinical evaluation of an O(6)-methylguanine-DNA methyltransferase-siRNA/liposome complex administered by convection-enhanced delivery to rat and porcine brains,” *American Journal of Translational Research*, vol. 6, no. 2, pp. 169–178, 2014.
- [107] S.-S. Kim, A. Rait, E. Kim, K. F. Pirollo, M. Nishida, N. Farkas, J. A. Dagata, and E. H. Chang, “A nanoparticle carrying the p53 gene targets tumors including cancer stem cells, sensitizes glioblastoma to chemotherapy and improves survival,” *ACS Nano*, vol. 8, no. 6, pp. 5494–5514, June 2014, doi: 10.1021/nn5014484.
- [108] S. S. Kim, A. Rait, E. Kim, K. F. Pirollo, and E. H. Chang, “A tumor-targeting p53 nanodelivery system limits chemoresistance to temozolomide prolonging survival in a mouse model of glioblastoma multiforme,” *Nanomedicine: Nanotechnology, Biology and Medicine*, vol. 11, no. 2, pp. 301–311, 2015, doi: 10.1016/j.nano.2014.09.005.
- [109] Q. Yang, Y. Zhou, J. Chen, N. Huang, Z. Wang, and Y. Cheng, “Gene Therapy for Drug-Resistant Glioblastoma via Lipid-Polymer Hybrid Nanoparticles Combined with Focused Ultrasound,” *International Journal Nanomedicine*, vol. 16, pp. 185–199, 2021, doi: 10.2147/IJN.S286221.
- [110] X. Chen, L. Tai, J. Gao, J. Qian, M. Zhang, B. Li, C. Xie, L. Lu, W. Lu, and W. Lu, “A stapled peptide antagonist of MDM2 carried by polymeric micelles sensitizes glioblastoma to temozolomide treatment through p53 activation,” *Journal of Controlled Release*, vol. 218, pp. 29–35, 2015, doi: 10.1016/j.jconrel.2015.09.061.
- [111] Y. Cui, A. Naz, D. H. Thompson, and J. Irudayaraj, “Decitabine nanoconjugate sensitizes human glioblastoma cells to temozolomide,” *Molecular Pharmaceutics*, vol. 12, no. 4, pp. 1279–1288, 2015, doi: 10.1021/mp500815b.
- [112] B. Yoo, M. A. Ifediba, S. Ghosh, Z. Medarova, and A. Moore, “Combination treatment with theranostic nanoparticles for glioblastoma sensitization to TMZ,” *Molecular imaging and Biology*, vol. 16, no. 5, pp. 680–689, October 2014, doi: 10.1007/s11307-014-0734-3.
- [113] T. Eslaminejad, S. N. Nematollahi-Mahani, and M. Ansari, “Glioblastoma Targeted Gene Therapy Based on pEGFP/p53-Loaded Superparamagnetic Iron Oxide Nanoparticles,” *Current Gene Therapy*, vol. 17, no. 1, pp. 59–69, 2017, doi: 10.2174/1566523217666170605115829.
- [114] M. J. Ramalho, J. A. Loureiro, M. A. N. Coelho, and M. C. Pereira, “Transferrin Receptor-Targeted Nanocarriers: Overcoming Barriers to Treat Glioblastoma,” *Pharmaceutics*, vol.

- 14, no. 2, January 2022, doi: 10.3390/pharmaceutics14020279.
- [115] M. G. Nava-Arzaluz, E. Piñón-Segundo, A. Ganem-Rondero, and D. Lechuga-Ballesteros, “Single emulsion-solvent evaporation technique and modifications for the preparation of pharmaceutical polymeric nanoparticles.,” *Recent Patents on Drug Delivery and Formulation*, vol. 6, no. 3, pp. 209–223, December 2012, doi: 10.2174/187221112802652633.
- [116] D. Cun, D. K. Jensen, M. J. Maltesen, M. Bunker, P. Whiteside, D. Scurr, C. Foged, and H. M. Nielsen, “High loading efficiency and sustained release of siRNA encapsulated in PLGA nanoparticles: Quality by design optimization and characterization,” *European Journal Pharmaceutics and Biopharmaceutics*, vol. 77, no. 1, pp. 26–35, 2011, doi: 10.1016/j.ejpb.2010.11.008.
- [117] D. Bartczak and A. G. Kanaras, “Preparation of peptide-functionalized gold nanoparticles using one pot EDC/Sulfo-NHS coupling,” *Langmuir*, vol. 27, no. 16, pp. 10119–10123, 2011, doi: 10.1021/la2022177.
- [118] S. Jose, R. Sebastian, A. Durazzo, M. Lucarini, A. Santini, and E. B. Souto, “Transferrin-conjugated Docetaxel-PLGA nanoparticles for tumor targeting: Influence on MCF-7 cell cycle,” *Polymers (Basel)*, vol. 11, no. 11, 2019, doi: 10.3390/polym11111905.
- [119] J. L. Li, L. Wang, X. Y. Liu, Z. P. Zhang, H. C. Guo, W. M. Liu, and S. H. Tang, “In vitro cancer cell imaging and therapy using transferrin-conjugated gold nanoparticles,” *Cancer Letters*, vol. 274, no. 2, pp. 319–326, 2009, doi: 10.1016/j.canlet.2008.09.024.
- [120] J. Stetefeld, S. A. McKenna, and T. R. Patel, “Dynamic light scattering: a practical guide and applications in biomedical sciences,” *Biophysic Review*, vol. 8, no. 4, pp. 409–427, 2016, doi: 10.1007/s12551-016-0218-6.
- [121] D. K. Carpenter, “Dynamic Light Scattering with Applications to Chemistry, Biology, and Physics),” *Journal of Chemical Education*, vol. 54, no. 10, p. A430, October 1977, doi: 10.1021/ed054pA430.1.
- [122] M. R. Siddiqui, Z. A. AlOthman, and N. Rahman, “Analytical techniques in pharmaceutical analysis: A review,” *Arabian Journal of Chemistry*, vol. 10, pp. S1409–S1421, 2017, doi: <https://doi.org/10.1016/j.arabjc.2013.04.016>.
- [123] J. Bart, R. Tiggelaar, M. Yang, S. Schlautmann, H. Zuilhof, and H. Gardeniers, “Room-temperature intermediate layer bonding for microfluidic devices.,” *Lab Chip*, vol. 9, no. 24, pp. 3481–3488, December 2009, doi: 10.1039/b914270c.
- [124] U. Guide, “Pierce™ BCA Protein Assay Kit,” no. 2161296, pp. 0–3, 2020.
- [125] B. Ladewig and M. N. Z. Al-Shaeli, “Membrane Characterization Techniques,” pp. 131–150, 2017, doi: 10.1007/978-981-10-2014-8_5.
- [126] Z. Bacsik, J. Mink, and G. Keresztury, “FTIR spectroscopy of the atmosphere. I. Principles and methods,” *Applied Spectroscopy Reviews*, vol. 39, no. 3, pp. 295–363, 2004, doi: 10.1081/ASR-200030192.
- [127] A. O. Odeh, “Qualitative and quantitative ATR-FTIR analysis and its application to coal char of different ranks,” *Ranliao Huaxue Xuebao/Journal Fuel Chemistry Technology*, vol. 43, no. 2, pp. 129–137, 2015, doi: 10.1016/s1872-5813(15)30001-3.
- [128] D. J. Smith, “Chapter 1 Characterization of Nanomaterials Using Transmission Electron Microscopy,” in *Nanocharacterisation (2)*, The Royal Society of Chemistry, 2015, pp. 1–29.
- [129] A. Moscardini, S. Di Pietro and G. Signore, “Uranium-free X solution: a new generation contrast agent for biological samples ultrastructure,” *Science Report*, vol. 10, no. 1, p. 11540, 2020, doi: 10.1038/s41598-020-68405-4.
- [130] J. Schuster, H.-C. Mahler, A. Koulov, S. Joerg, A. Racher, J. Huwyler, P. Detampel and R. Mathaes, “Tracking the physical stability of fluorescent-labeled mAbs under physiologic in vitro conditions in human serum and PBS,” *European Journal of Pharmaceutics and Biopharmaceutics*, vol. 152, pp. 193–201, 2020, doi: <https://doi.org/10.1016/j.ejpb.2020.04.014>.
- [131] J.-H. Tang, L. Yang, J. X. Chen, Q. R. Li, L. R. Zhu, Q. F. Xu, G. H. Huang, Z. X. Zhang, Y. Xiang, L. Du, Z. Zhou, and S. Q. Lv, “Bortezomib inhibits growth and sensitizes glioma

- to temozolomide (TMZ) via down-regulating the FOXM1–Survivin axis,” *Cancer Communications*, vol. 39, no. 1, p. 81, 2019, doi: 10.1186/s40880-019-0424-2.
- [132] P. J. Vlachostergios, E. Hatzidaki, C. D. Befani, P. Liakos, and C. N. Papandreou, “Bortezomib overcomes MGMT-related resistance of glioblastoma cell lines to temozolomide in a schedule-dependent manner,” *Investigational New Drugs*, vol. 31, no. 5, pp. 1169–1181, 2013, doi: 10.1007/s10637-013-9968-1.
- [133] V. Vichai and K. Kirtikara, “Sulforhodamine B colorimetric assay for cytotoxicity screening,” *Nature Protocols*, vol. 1, no. 3, pp. 1112–1116, 2006, doi: 10.1038/nprot.2006.179.
- [134] N. P. Truong, M. R. Whittaker, C. W. Mak, and T. P. Davis, “The importance of nanoparticle shape in cancer drug delivery,” *Expert Opinion on Drug Delivery*, vol. 12, no. 1, pp. 129–142, 2015, doi: 10.1517/17425247.2014.950564.
- [135] J. Fonseca-Gomes, J. A. Loureiro, S. R. Tanqueiro, F. M. Mouro, P. Ruivo, T. Carvalho, A. M. Sebastião, M.J. Diogenes and M. C. Pereira “In vivo bio-distribution and toxicity evaluation of polymeric and lipid-based nanoparticles: A potential approach for chronic diseases treatment,” *International Journal of Nanomedicine*, vol. 15, pp. 8609–8621, 2020, doi: 10.2147/IJN.S267007.
- [136] Y. Liu, J. Pan, and S.-S. Feng, “Nanoparticles of lipid monolayer shell and biodegradable polymer core for controlled release of paclitaxel: effects of surfactants on particles size, characteristics and in vitro performance.,” *International Journal of Pharmaceutics*, vol. 395, no. 1–2, pp. 243–250, August 2010, doi: 10.1016/j.ijpharm.2010.05.008.
- [137] S. Pradhan, J. Hedberg, E. Blomberg, S. Wold, and I. Odnevall Wallinder, “Effect of sonication on particle dispersion, administered dose and metal release of non-functionalized, non-inert metal nanoparticles,” *Journal of Nanoparticle Research*, vol. 18, no. 9, p. 285, 2016, doi: 10.1007/s11051-016-3597-5.
- [138] D. R. P. Loureiro, J. Soares, D. Lopes, T. Macedo, D. Yordanova, S. Jakobtorweihen, C. Nunes, S. Reis, M. Pinto and C. Afonso, “Assessing lipophilicity of drugs with biomimetic models: A comparative study using liposomes and micelles,” *European Journal of Pharmaceutical Science*, vol. 115, pp. 369–380, 2018, doi: <https://doi.org/10.1016/j.ejps.2018.01.029>.
- [139] M. J. Ramalho, M. Bravo, J. A. Loureiro, J. Lima, and M. C. Pereira, “Transferrin-modified nanoparticles for targeted delivery of Asiatic acid to glioblastoma cells,” *Life Science*, vol. 296, p. 120435, 2022, doi: <https://doi.org/10.1016/j.lfs.2022.120435>.
- [140] C. Berthomieu and R. Hienerwadel, “Fourier transform infrared (FTIR) spectroscopy,” *Photosynthesis Research*, vol. 101, no. 2, pp. 157–170, 2009, doi: 10.1007/s11120-009-9439-x.
- [141] Y.-L. Zhao, “Enhancing water-solubility of poorly soluble drug, Asiatic Acid with hydroxypropyl- β -cyclodextrin,” *Digest Journal of Nanomaterials and Biostructures*, vol. 5, 2010.
- [142] S. Boimvaser, R. N. Mariano, L. N. Turino, and J. R. Vega, “In vitro bulk/surface erosion pattern of PLGA implant in physiological conditions: a study based on auxiliary microsphere systems,” *Polymer Bulletin*, vol. 73, no. 1, pp. 209–227, 2016, doi: 10.1007/s00289-015-1481-6.
- [143] P. Rafiei and A. Haddadi, “Docetaxel-loaded PLGA and PLGA-PEG nanoparticles for intravenous application: pharmacokinetics and biodistribution profile.,” *International Journal of Nanomedicine*, vol. 12, pp. 935–947, 2017, doi: 10.2147/IJN.S121881.
- [144] J. A. Loureiro, B. Gomes, G. Fricker, M. A. N. Coelho, S. Rocha, and M. C. Pereira, “Cellular uptake of PLGA nanoparticles targeted with anti-amyloid and anti-transferrin receptor antibodies for Alzheimer’s disease treatment.,” *Colloids and Surface. B. Biointerfaces*, vol. 145, pp. 8–13, September 2016, doi: 10.1016/j.colsurfb.2016.04.041.
- [145] P. Bihari, M. Vippola, S. Schultes, M. Praetner, A. G. Khandoga, C. A. Reichel, C. Coester, T. Tuomi, M. Rehberg, and F. Krombach, “Optimized dispersion of nanoparticles for biological in vitro and in vivo studies,” *Particle and Fibre Toxicology*, vol. 5, p. 14, November 2008, doi: 10.1186/1743-8977-5-14.

- [146] K. W. Powers, S. C. Brown, V. B. Krishna, S. C. Wasdo, B. M. Moudgil, and S. M. Roberts, "Research Strategies for Safety Evaluation of Nanomaterials. Part VI. Characterization of Nanoscale Particles for Toxicological Evaluation," *Toxicology Science*, vol. 90, no. 2, pp. 296–303, April 2006, doi: 10.1093/toxsci/kfj099.
- [147] P. J. Vlachostergios, E. Hatzidaki, N. E. Stathakis, G. K. Koukoulis, and C. N. Papandreou, "Bortezomib downregulates MGMT expression in T98G glioblastoma cells.," *Cell and Molecular Neurobiology*, vol. 33, no. 3, pp. 313–318, April 2013, doi: 10.1007/s10571-013-9910-2.
- [148] M. A. Rahman, A. Gras Navarro, J. Brekke, A. Engelsen, C. Bindesbøll, S. Sarowar, M. Bahador, E. Bifulco, D. Goplen, A. Waha, S. A. Lie, B. T. Gjertsen, F. Selheim, P. Ø. Enger, A. Simonsen, and M. Chekenya, "Bortezomib administered prior to temozolomide depletes MGMT, chemosensitizes glioblastoma with unmethylated MGMT promoter and prolongs animal survival," *British Journal of Cancer*, vol. 121, no. 7, pp. 545–555, 2019, doi: 10.1038/s41416-019-0551-1.
- [149] X. Zhang, W. Li, C. Wang, X. Leng, S. Lian, J. Feng, J. Li, and H. Wang, "Inhibition of autophagy enhances apoptosis induced by proteasome inhibitor bortezomib in human glioblastoma U87 and U251 cells," *Molecular and Cellular Biochemistry*, vol. 385, no. 1, pp. 265–275, 2014, doi: 10.1007/s11010-013-1835-z.

Appendix

A1. Calibration Curves

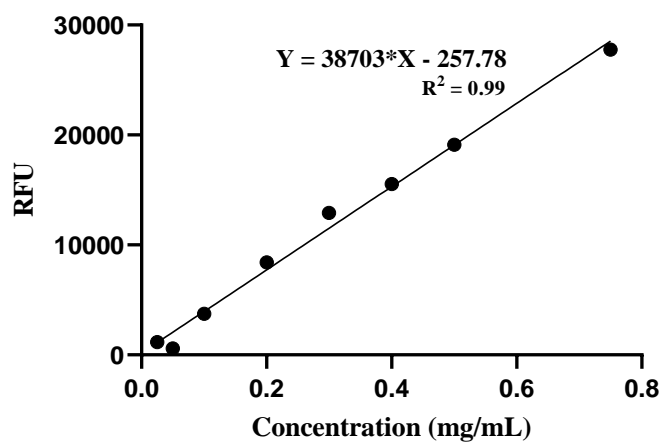


Figure A1.1 - Fluorescence (RFU) calibration curve of TMZ in PVA 2% to determine the EE of TMZ.

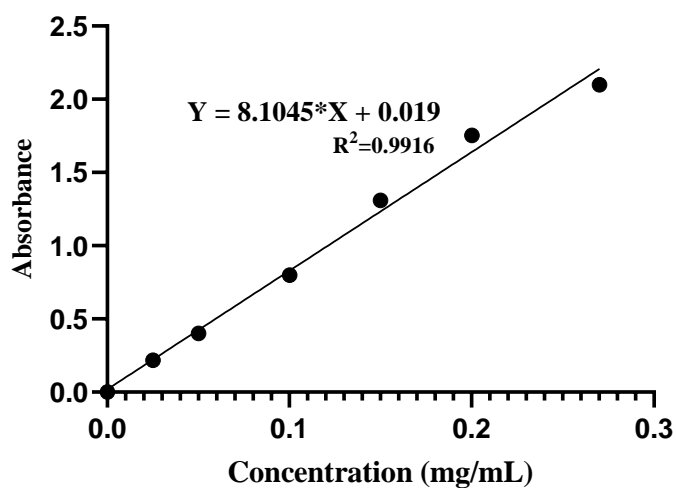


Figure A1.2 – Absorbance calibration curve of BTZ in PVA 2% to determine the EE of BTZ.

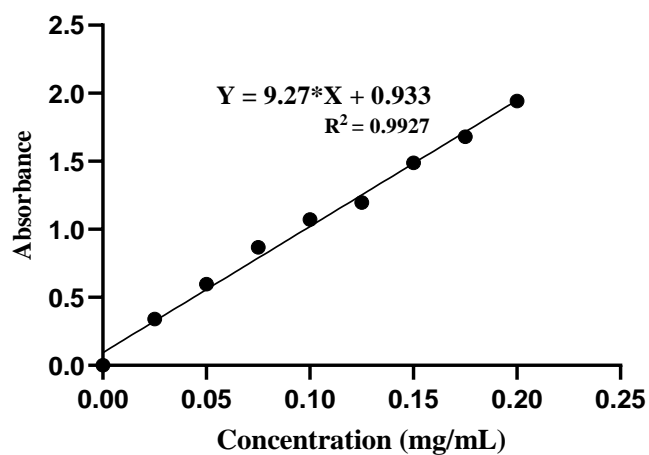


Figure A1.3 - Absorbance calibration curve of Tf using the BCA kit for Tf quantification.

A2. Experimental Design

Table A2.1 - ANOVA analysis for the response variable Size (Y_1) applying a quartic model.

Size (Y_1)						
Source	Sum of Squares	df	Mean Square	F-value	p-value	
Model	5.569×10^5	24	23205.54	1430.38	0.0007	significant
X ₁ -PLGA Mass	109.52	1	109.52	6.75	0.1217	
X ₂ -%PVA	2.851×10^5	1	2.851×10^5	17572.71	< 0.0001	
X ₃ -Sonication Cycles	182.41	1	182.41	11.24	0.0786	
X ₄ -Ratio O/W	144.50	1	144.50	8.91	0.0963	
X ₁ X ₂	1044.91	1	1044.91	64.41	0.0152	
X ₁ X ₃	944.03	1	944.03	58.19	0.0168	
X ₁ X ₄	1315.88	1	1315.88	81.11	0.0121	
X ₂ X ₃	411.08	1	411.08	25.34	0.0373	
X ₂ X ₄	439.95	1	439.95	27.12	0.0350	
X ₃ X ₄	405.02	1	405.02	24.97	0.0378	
X ₁ ²	61.06	1	61.06	3.76	0.1919	
X ₂ ²	1.683×10^5	1	1.683×10^5	10373.04	< 0.0001	
X ₃ ²	163.80	1	163.80	10.10	0.0864	
X ₄ ²	7.11	1	7.11	0.4380	0.5762	
Pure Error	32.45	2	16.22			
Cor Total	5.570×10^5	26				

Table A2.2 - ANOVA analysis for the response variable PDI (Y_2) applying a linear model.

PDI (Y_2)						
Source	Sum of Squares	df	Mean Square	F-value	p-value	
Model	0.0488	4	0.0122	2.90	0.0454	significant
X ₁ -PLGA Mass	0.0223	1	0.0223	5.30	0.0312	
X ₂ -%PVA	0.0062	1	0.0062	1.46	0.2395	
X ₃ -Sonication Cycles	0.0069	1	0.0069	1.64	0.2142	
X ₄ -Ratio O/W	0.0135	1	0.0135	3.21	0.0870	
Residual	0.0926	22	0.0042			

Lack of Fit	0.0915	20	0.0046	8.60	0.1092	not significant
Pure Error	0.0011	2	0.0005			
Cor Total	0.1414	26				

Table A2.3 - ANOVA analysis for the response variable Zeta Potential (Y_3) applying a quadratic model.

Zeta Potential (Y_3)						
Source	Sum of Squares	df	Mean Square	F-value	p-value	
Model	86.85	14	6.20	1.87	0.1424	not significant
X_1 -PLGA Mass	1.32	1	1.32	0.3966	0.5407	
X_2 -%PVA	12.16	1	12.16	3.66	0.0799	
X_3 -Sonication Cycles	12.81	1	12.81	3.86	0.0732	
X_4 -Ratio O/W	0.0008	1	0.0008	0.0002	0.9878	
X_1X_2	0.3906	1	0.3906	0.1176	0.7376	
X_1X_3	1.89	1	1.89	0.5690	0.4652	
X_1X_4	10.08	1	10.08	3.03	0.1071	
X_2X_3	4.73	1	4.73	1.42	0.2558	
X_2X_4	7.98	1	7.98	2.40	0.1471	
X_3X_4	0.8556	1	0.8556	0.2575	0.6210	
X_1^2	7.47	1	7.47	2.25	0.1596	
X_2^2	0.1080	1	0.1080	0.0325	0.8599	
X_3^2	14.23	1	14.23	4.28	0.0607	
X_4^2	12.83	1	12.83	3.86	0.0730	
Residual	39.87	12	3.32			
Lack of Fit	31.38	10	3.14	0.7396	0.6978	not significant
Pure Error	8.49	2	4.24			
Cor Total	126.72	26				

Table A2.4 - ANOVA analysis for the response variable EE TMZ (Y₄) applying a quadratic model.

EE TMZ (Y₄)						
Source	Sum of Squares	df	Mean Square	F-value	p-value	
Model	5348.59	14	382.04	0.5667	0.8453	not significant
X ₁ -PLGA Mass	1350.05	1	1350.05	2.00	0.1825	
X ₂ -%PVA	364.66	1	364.66	0.5409	0.4762	
X ₃ -Sonication Cycles	1043.29	1	1043.29	1.55	0.2372	
X ₄ -Ratio O/W	144.59	1	144.59	0.2145	0.6516	
X ₁ X ₂	20.25	1	20.25	0.0300	0.8653	
X ₁ X ₃	14.21	1	14.21	0.0211	0.8870	
X ₁ X ₄	897.90	1	897.90	1.33	0.2709	
X ₂ X ₃	31.19	1	31.19	0.0463	0.8333	
X ₂ X ₄	429.73	1	429.73	0.6375	0.4401	
X ₃ X ₄	0.0900	1	0.0900	0.0001	0.9910	
X ₁ ²	737.83	1	737.83	1.09	0.3161	
X ₂ ²	138.87	1	138.87	0.2060	0.6580	
X ₃ ²	143.07	1	143.07	0.2122	0.6533	
X ₄ ²	32.85	1	32.85	0.0487	0.8290	
Residual	8089.67	12	674.14			
Lack of Fit	7306.73	10	730.67	1.87	0.3989	not significant
Pure Error	782.94	2	391.47			
Cor Total	13438.26	26				

Table A2.5 - ANOVA analysis for the response variable EE BTZ (Y₅) applying a quadratic model.

EE BTZ (Y₅)						
Source	Sum of Squares	df	Mean Square	F-value	p-value	
Model	5371.72	14	383.69	1.07	0.4581	not significant
X ₁ -PLGA Mass	93.43	1	93.43	0.2606	0.6190	
X ₂ -%PVA	2360.39	1	2360.39	6.58	0.0247	

X ₃ -Sonication Cycles	172.33	1	172.33	0.4807	0.5013	
X ₄ -Ratio O/W	476.20	1	476.20	1.33	0.2715	
X ₁ X ₂	627.88	1	627.88	1.75	0.2104	
X ₁ X ₃	0.5366	1	0.5366	0.0015	0.9698	
X ₁ X ₄	187.21	1	187.21	0.5222	0.4837	
X ₂ X ₃	91.92	1	91.92	0.2564	0.6218	
X ₂ X ₄	97.17	1	97.17	0.2711	0.6121	
X ₃ X ₄	6.64	1	6.64	0.0185	0.8940	
X ₁ ²	60.01	1	60.01	0.1674	0.6896	
X ₂ ²	296.08	1	296.08	0.8259	0.3814	
X ₃ ²	11.69	1	11.69	0.0326	0.8597	
X ₄ ²	890.24	1	890.24	2.48	0.1410	
Residual	4301.94	12	358.49			
Lack of Fit	3762.40	10	376.24	1.39	0.4883	not significant
Pure Error	539.54	2	269.77			
Cor Total	9673.66	26				

A2.1 NPs Size

$$\begin{aligned}
 \text{Size} = & 151.07 + 4.78 (\text{PLGA mass}) - 244.10 (\% \text{PVA}) - 6.17 (\text{Sonication Cycles}) \\
 & + 5.50 (\text{O/W Ratio}) + 8.08 (\text{PLGA mass}) (\% \text{PVA}) \\
 & + 7.68 (\text{PLGA mass}) (\text{Sonication Cycles}) \\
 & + 9.07 (\text{PLGA mass}) (\text{O/W Ratio}) \\
 & + 5.07 (\% \text{PVA}) (\text{Sonication Cycles}) \\
 & - 5.24 (\% \text{PVA}) (\text{O/W Ratio}) \\
 & + 5.03 (\text{Sonication Cycles}) (\text{O/W Ratio})
 \end{aligned} \tag{1}$$

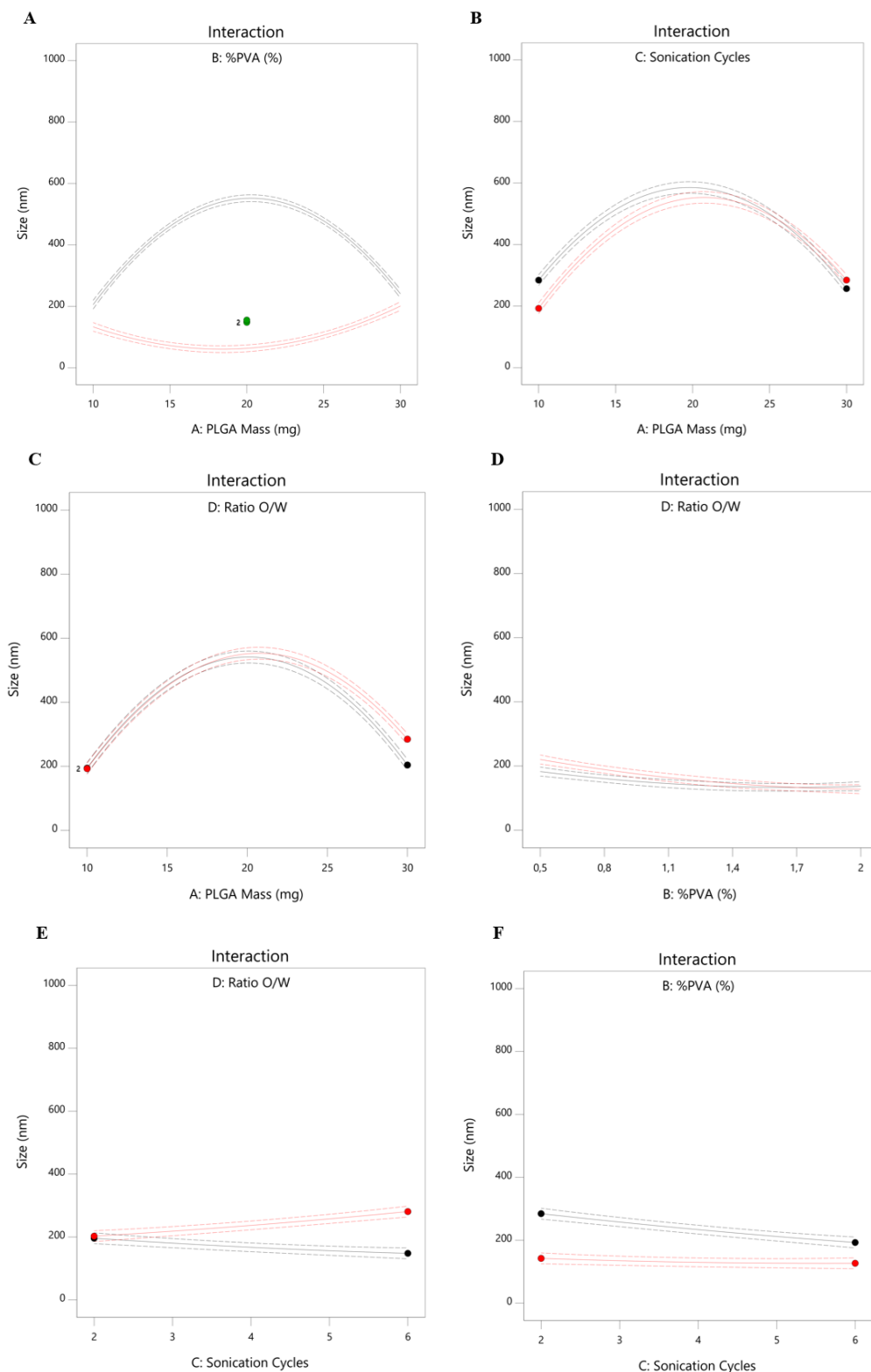


Figure A2.1 – Interaction plots regarding to Y_1 the NPs' size. (A) Interaction plot of X_1 and X_2 . The red line represents the O/W ratio (X_4) values (+1), and the black line represents the sonication cycles (X_3) values (-1). (B) Interaction plot of X_1 and X_3 . The red line represents the O/W ratio (X_4) values (+1), and the black line represents the %PVA (X_2) values (-1). (C) Interaction plot of X_1 and X_4 . The red line represents the sonication cycle (X_3) values (-1), and the black line represents the %PVA (X_2) values (-1). (D) Interaction plot of X_2 and X_4 . The red line represents the sonication cycle (X_3) values (+1), and the black line represents the PLGA mass (X_1) values (-1). (E) Interaction plot of X_3 and X_4 . The red line represents the %PVA (X_2) values (-1), and the black line represents the PLGA mass (X_1) values (+1).

A2.2 NPs PDI

$$\begin{aligned} \text{PDI} = & 0.0944 + 0.0327 (\text{PLGA mass}) - 0.0172 (\% \text{PVA}) \\ & - 0.0182 (\text{Sonication Cycles}) + 0.0255 (\text{O/W Ratio}) \end{aligned} \quad (2)$$

A3. FTIR Analysis

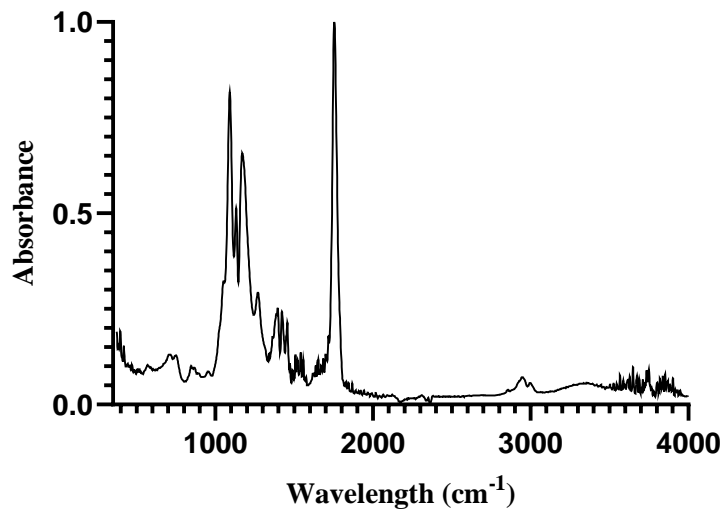


Figure A3.1 – FTIR absorbance spectrum of TMZ+BTZ loaded PLGA NPs solution recorded from 350-4000 cm⁻¹.

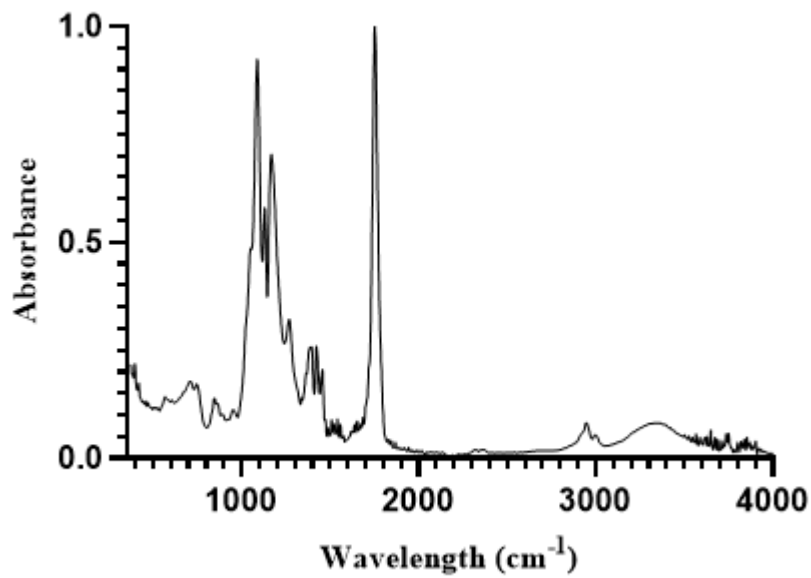


Figure A3.2 – FTIR absorbance spectrum of Tf-unloaded PLGA NPs solution recorded from 350-4000 cm⁻¹.